UNIVERSITY OF GAZİANTEP
GRADUATE SCHOOL OF
NATURAL AND APPLIED SCIENCES

FINITE ELEMENT ANALYSIS OF TEMPERATURE DISTRIBUTION IN PRECAST CONCRET GIRDERS SUBJECTED TO THERMAL LOADS

M. Sc. THESIS
IN
CIVIL ENGINEERING

BY
IHSSAN ADIL AL-HATMEY
NOVEMBER 2014

Finite Element Analysis of Temperature Distribution in Precast Concrete Girders Subjected to Thermal Loads

M.Sc. Thesis

In

Civil Engineering

University of Gaziantep

Supervisor

Assist. Prof. Dr. Nildem TAYŞİ

By

Ihssan Adil AL-HATMEY

November 2014

T.C.

UNIVERSITY OF GAZİANTEP

GRADUATE SCHOOL OF NATURAL & APPLIED SCIENCES

CIVIL ENGINEERING DEPARTMENT

Name of the thesis: Finite Element Analysis of Temperature Distribution in Precast
Concrete Girders Subjected to Thermal Loads

Name of the student: Ihssan Adil AL-HATMEY

Exam date: November 21, 2014

Approval of the Graduate School of Natural and Applied Sciences.

Prof. Dr. Metin BEDİR

Director

I certify that this thesis satisfies all the requirements as thesis for the degree of
Master of Science.

Prof. Dr. Mustafa GÜNAL

Head of Department

This is to certify that we have read this thesis and that in our opinion it is fully
adequate, in scope and quality, as a thesis for the degree of Master of Science.

Assist. Prof. Dr. Nildem TAYŞİ

Supervisor

Examininig Committee Members: Signatures

Prof. Dr. Mustafa ÖZAKÇA

Assist. Prof. Dr. Nildem TAYŞİ

Assist. Prof. Dr. Ömer Yavuz BOZKURT

Declaration

I hereby declare that all information in this document has been obtained and presented in accordance with academic rules and ethical conduct. I also declare that, as required by these rules and conduct, I have fully cited and referenced all   material and results that are not original to this work.

Ihssan AL-HATMEY

ABSTRACT

FINITE ELEMENT ANALYSIS OF TEMPERATURE DISTRIBUTION IN
PRECAST CONCRET GIRDERS SUBJECTED TO THERMAL LOADS

AL-HATMEY, Ihssan Adil

M.Sc. in Civil Engineering

Supervisor: Assist. Prof. Dr. Nildem TAYŞİ

November 2014, 100 pages

In general, the present bridge design codes introduce special provisions to control the possible effects of thermal loads that results from solar radiation and variation in air temperature. In this research, a thermal finite element analysis was conducted to study the temperature distributions and temperature gradients in precast concrete bridge girders under the effect of the daily variations of solar radiation, air temperature and wind speed. The proposed finite element model was verified with experimental results from literature, in which good agreement was found between the finite element results and the experimental records. The finite element model was then used to study the time dependent temperature variations and vertical temperature gradients for extreme thermal loads in Gaziantep, Turkey, in which weather stations was installed and climate records for more than 30 years were utilized. Comparisons were made between the predicted maximum vertical temperature gradient for the case of Gaziantep extremes and four available gradient models. The comparisons showed that with minor modifications, the current AASHTO temperature gradient model can be used to simulate Gaziantep extreme conditions.

Keywords: finite element analysis, precast concrete girder, solar radiation, temperature gradient, thermal loads.

ÖZET

SICAKLIK YÜKLEMELERINE MARUZ KALAN PREFABRIK BETON KİRİŞLERIN SONLU ELEMANLAR İLE SICAKLIK DAĞILIMLARININ ANALİZİ

AL-HATMEY, Ihssan Adil

İnşaat Mühendisliği Yüksek Lisans

Danışman: Yrd. Doç. Dr. Nildem TAYŞİ

Kasım 2014, 100 Sayfa

Genel olarak mevcut olan köprü tasarım standartları, güneş ışınları ve hava sıcaklıklarındaki farklılıklardan dolayı oluşabilecek muhtemel sıcaklık etkilerini kontrol etmek için özel öneriler sunmaktadırlar. Bu çalışmada, güneş ışınları, hava sıcaklığı ve rüzgar hızının günlük değişimlerinden dolayı öndökümlü betonarme köprü kesitlerindeki sıcaklık dağılımları ve sıcaklık farklılıklarını incelemek için, sonlu elemanlar ısıl analizleri yapılmıştır. Önerilen sonlu elemanlar modeli literatürdeki deneysel sonuçlarla doğrulanmıştır ve sonlu elemanlar sonuçları ile deneysel sonuçlar arasında iyi bir uyum gözlemlenmiştir. Daha sonra doğrulanan bu sonlu elemanlar modeli Gaziantep, Türkiye'deki 30 yıllık meteorolojiden alınan verilerdeki aşırı sıcaklık yüklerini zamana bağlı sıcaklık dağılımlarını ve değişimlerini hesaplamak için kullanılmıştır. Gaziantep'teki tahmin edilen maksimum düşey sıcaklık değişimleri ve mevcut olan dört değişim modeli sonuçları arasında karşılaştırmalar yapılmıştır. Karşılaştırmalar göstermektedir ki, ufak iyileştirmeler ile mevcut AASHTO sıcaklık değişim modeli, Gaziantep'teki aşırı durumları yansıtmak için kullanılabilir.

Anahtar Kelimeler: sonlu elemanlar analizi, öndökümlü betonarme köprü, güneş ışınımları, sıcaklık değişimleri, ısıl yüklemeler.

ACKNOWLEDGMENT

TABLE OF CONTENTS

LIST OF FIGURES

xiv

LIST OF TABLES

LIST OF SYMBOLS

a	Surface absorptivity of the girder surfaces
C	Specific heat capacity in $Jk/g°\mathrm{C}$
ρ	Density in kg/m^3
h_c	Convection heat transfer coefficient
I_s	Extraterrestrial solar radiation
k_x	Thermal conductivities in x direction
k_y	Thermal conductivities in y direction
k_z	Thermal conductivities in z direction
Q	Amount of heat generated within the body W/m^3
q_c	Heat convection
q_g	Heat absorbed from solar radiation
q_r	Heat radiation to the surrounding atmosphere
q_s	Heat irradiation from the sun
T	Temperature at any point (x, y, z) at any time, t
T_a	Ambient air temperature
T_s	Concrete surface temperature
T_{top}	Temperature on the top surface of the deck slab
T_1	Temperature that develops at the top of the bridge deck
T_2	Temperature that develops at location 0.1 meters below the top of the bridge deck
T_3	Temperature that develops in the bottom of the superstructure
v	Wind speed
ϵ	Surface emissivity

σ Stefan-Boltzman radiation constant $5.67 \times 10^{-8} W/m^2 K^4$

θz Solar zenith angle between the line overhead and the line to the sun

Ψs Angle of rotation along the bridge length

CHAPTER 1

INTRODUCTION

1.1 General

Precast Prestressed Concrete (PC) girders are increasingly utilized in construction of concrete bridges all around the world. Many of the research were conducted using various materials and different structural analyzes and construction techniques to increase the span of the PC girders. Most of these studies focused on the structural stiffness, material development, the whole bridge structural and the integrity of the girders. Also the many design codes presented various types and recommended special design specification and construction limitations. Considers (AASHTO) among of these codes. Special provisions have been recommended for the thermal considerations to control influence of temperature differentials arises from variations of climate including solar radiation and air temperature. However, further studies there is a need to understand the behavior of PC bridge girders under time-dependent thermal loads, which can caused deformations and stresses that affect the depend on time durability and the structural safety of the bridge girders.

Due to climatological variations in the ambient environment, bridges continuously gain and lose heat. The heat transfers take place during three principal mechanisms: convection of heat between the ambient air and the surface, radiation from the sun, and re-radiation of the surface to or from the ambient environment. The solar radiation intensity reaching the surface of a bridge and the surrounding air temperature are functions of the time of day and also the time of the year. The interaction between the climatological environment and the surface of the structure results in temperature variation between the elements of the structure. These temperature variations, in turns, produce strains and deformations in the structure. The intensity of solar radiation reaches of the bridge superstructure primarily through direct radiation, diffused radiation from the sky and reflected from the surrounding objects.

The coming radiation reaching the surface may penetrate the surface or may be reflected back, be absorbed and transform to heat. The magnitude of absorbed energy depends on the color and nature of the receiving surface. A rough and dark surface has a higher absorptivity than does a smooth and light surface. Some of this absorbed energy is lost to the air by re-radiation and convection. Convective heat transfer is a function of the temperature difference between the ambient air and the surface as well as wind speed as shown Figure 1.1.
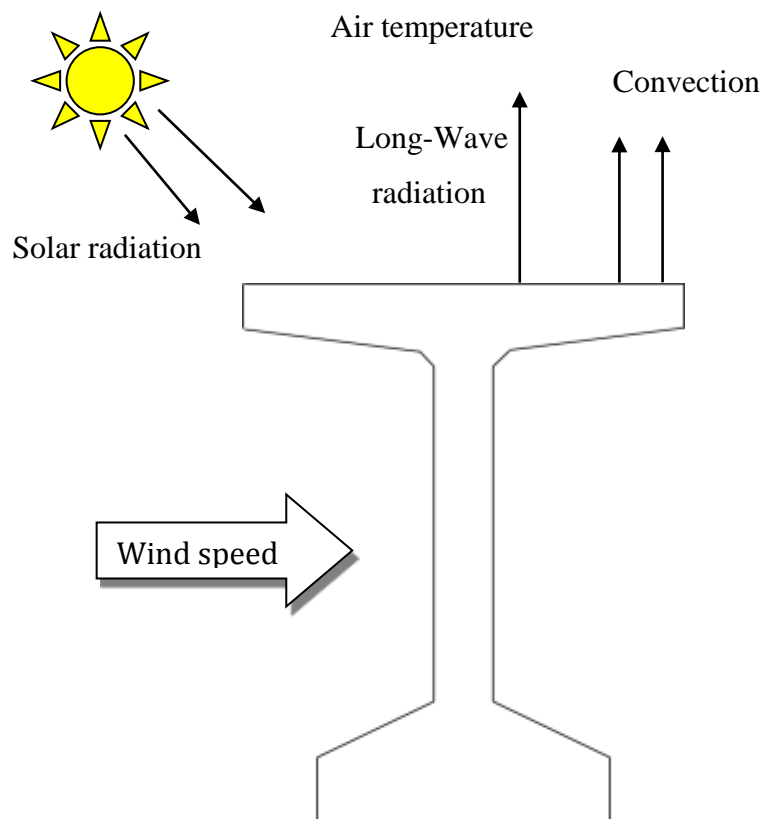
Figure 1.1 Cooling and heating of concrete girder

In this research, Two Dimensional (2D) and Three Dimensinal (3D) Finite Element (FE) analysis will be carried out to understand the temperature gradients and temperature distribution occurs within the various parts of the PC girders under time-dependent thermal loads. In this research, FE method will be using two various commercial FE packages to research the thermal behavior of (AASHTO) PC girders also under time-dependent thermal loads. The results of this study may contribute to a best understanding of the vertical temperature distribution in the girder and hence vertical temperature gradients which are very important for design considerations to

control the thermal deformations of the bridge girders. Also, lateral temperature gradients and temperature distribution in the bridge girder will be studied, which also may lead to thermal cracks. Tow FE packages will be used to simulate the time dependent heat transfer problem in the PC girder. The first is the well known FE package ANSYS [1], while the second is the multi-physics FE program COMSOL [2]. Results of the both programs will be verified and compared with experimental results from literature.

1.2 Objectives and Layout of the Thesis

The goals of this research are to investigate differences in the temperature distributions of PC bridge girders under different environmental conditions and to evaluate the behavior of the bridge girders. This study determines extremes in seasonal climate conditions pertaining to the highest vertical and lateral temperature differentials and suggested vertical and lateral thermal gradients for the design of the PC bridge girders. Also study the influences of seasonal variations and various bridge orientations on the lateral and vertical temperature differentials. Another important mission in this search is work on the FE program to carry out the heat transfer model and the structural model of the problem. Two FE packages were tried to simulate the heat transfer problem.

Chapter two shows the literature review that summarizes the researches that dealt with the thermal environmental effects of concrete bridge girders. Chapter three presents basic equations of the heat transfer also describes experimental and FE results of the compared study. In chapter four and five, results from ANSYS and COMSOL programs respectively, are presented and discussed in details during the first of June 1st and on November 15th.Chapter six determines extremes for seasons of the year environmental conditions associated to the maximum vertical and lateral temperature distributions and temperature gradient in Gaziantep. Finally, Chapter seven summarizes the results of the current study for the thermal responses and behavior of prestressed concrete bridges.

CHAPTER 2

LITERATURE REVIEW

2.1 General

The interest in researching the conduct of bridge structures under climate thermal loading was increased significantly in latest years. Expected stress distributions and temperature within a bridge structure for design considerations was concentration of many investigators.

Early realization in this field attempted to relate temperature average within the structure to the ambient weather data. Expecting of the temperature field from the actual climate conditions has been a later step. Variation approaches were used to expect this temperature field. For structures of the simple geometry, traditional methods of analysis have been utilized. However, for structure with compound geometry, numerical techniques depended on finite difference or FE was adopted.

In the following, a brief study of the heat transfer mechanism that take place between the atmosphere and the structure is introduced along with a review of the experimental and theoretical study previously done. Also the types of thermally caused stresses in structure are discussed.

2.2 Environmental Thermal Influences in Concrete Bridges

Narouka et al. [3] conducted tested on a composite steel bridge produced in the determination of a nonlinear distribution of temperature during the depth of the bridge section. The maximum calculated temperature differential was found to be -9 °C.

Barber [4] introduced a formula capable of guess the maximum temperature on the surface pavement of the bridge. Also this formula incorporated the wind speed, pavement temperature properties, air temperature, solar radiation and the surface temperature.

Leonhardt et al. [5] reported that nonlinear thermal gradients case the cracks and the lateral movements in the PC Box Girder (BG) in Germany for Jagst Bridge, after that, was interested in the temperature differences under climate conditions.

Early studies with thermal effects on bridge superstructure beyond 1960 basically used on One-dimension heat flow, Zuk [6] found a new method to compute stresses and temperature deflection from linear thermal gradients. Later, Zuk [7] calculated the maximum temperature on the surface of a steel and composite bridges using an equation that suggested by Barber [4].

Priestley [8] analyzed the influence of different available proposed temperature differentials and compared the results with obtainable measured data. One of these proposed gradients is the one suggested by Maher [9]. Maher proposed a linear temperature gradient during the top slab of the superstructure. This assumption was depended on variation measurements taken from several bridges in Britain. Another proposed thermal gradient research by Priestley is the one suggested by the Ministry of Works of New Zealand [10] that the temperature vary with several depth as second, fourth and sixth degree parabolas.

Priestley [11] conducted several parametric studies on PC girder deck slab bridges and BG to study the influence of climate thermal loads on bridges; he proposed a nonlinear fifth order temperature gradient, which varies from a maximum at the top surface to zero at 1.2 m blow the top surface. The proposed fifth order gradient model is illustrated in Figure 2.1
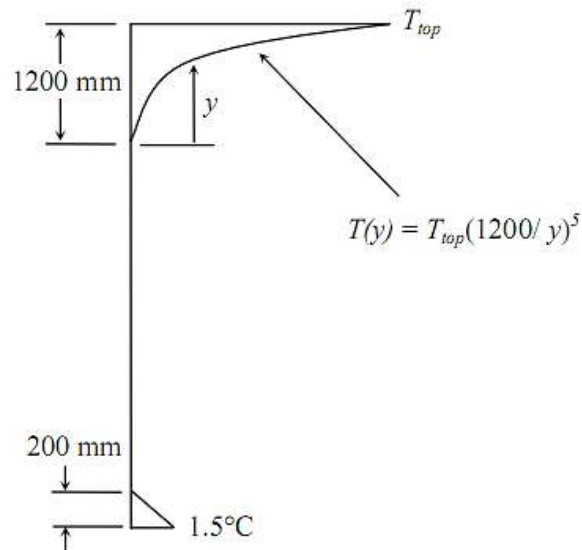
Figure 2.1 Vertical thermal gradient suggested by Priestley [11]

Emerson [12] used finite difference method in one dimensional (1D) to compute temperature distribution in steel, composite and concrete bridges based on ambient air temperature, wind speed, solar radiation. The author started the numerical computations at the early morning hours between 4:00 am and 8:00 am during which, the temperature of the bridge is nearly uniform. For concrete bridges, the maximum thermal gradients take place around 4:00 pm for the thick slab and the box section, while it take place around 3:00 pm for the thin slab in the summer reversed the thermal gradients generally take place around 6:00 am for thick slab and the box section while it take place around 5:00 am for the thin slab in the winter.

Lanigan [13] developed a 2D FE program to find temperature distribution during bridge-type structures. The results got from the program exhibited good agreement with the measurements done on laboratory models. Reynolds and Emanuel [14] reported their research of the different parameters that effect the estimation of temperature gradient between the inner and outer surfaces of the bridge structure. Also they reported the results of different measurements and theoretical studies carried out on the temperature response of bridges.

Will et al. [15, 16] developed FE-programs for thermal stress analysis and the heat transfer of bridge structures. The 2D FE was used to predict thermal distributions inside the concrete bridges. The thermal stresses and movements were then estimated using a thermal stress program based on the predicted temperatures from the 2D

temperature analysis. The author found that the calculated movements have good agreement with field coupled movements.

Radolli and Green [17] used 1D finite difference method to expected temperature distribution in "I" girders and concrete slab bridges. Predicted observed measurements and temperature differential were in good agreement. They suggested simplified formulas to predict thermal gradients for use in design.

Emanuel and Hulsey [18] used FE method introduced minimum and maximum deck temperatures as well as vertical temperature variations concrete composite and steel bridges exposed climate variation. The predicted maximum temperature for hot day and the predicted minimum temperature for cold day were 66 $^{\circ}$C and 23 $^{\circ}$C respectively. While the vertical temperature variation, the predicted maximum temperature for the top and the predicted the minimum temperature for the bottom were 22 $^{\circ}$C and 17 $^{\circ}$C respectively.

Dilger et al. [19, 20] took into account for the location, the orientation and the geometry of the bridge when compute bridge temperatures using a method of 1D finite difference. The expected temperatures showed good correspond with the accounted data at the bridge on Muskwa River in British Columbia. Thermal stresses also were calculated using extreme of the expected temperatures. This research showed that the highest temperature variations took place during the following conditions:

- High density of solar radiation
- Large daily difference in surrounding temperature
- No shade or small of the box flange overhang
- Big size of the steel box
- Dark surface of the steel box
- Non-presence of wind

Kenney and Soliman [21] whose studies were depended on past several experimental and theoretical results suggested a simple thermal gradients and vertical thermal gradient in concrete composite and steel bridges for the winter and summer seasons. The temperature distribution which recommended for Southern Ontario and the

Middle Atlantic States, Canada was uniform during the depth of the steel girder and linear during the depth of the concrete deck.

Clark [22] studied the frequency occurrence of temperature differentials in a BG bridge throughout a period of 50 years. He explained that the critical temperature distribution was related to the maximum and minimum values of the surrounding air temperature.

Emerson [23, 24] carried out extended experimental studies on composite, steel and concrete bridges of various dimensions and shapes located in Wales and England. Amongst other bridges, also she carried out extensive research on BG cross sections. The levels of the maximum thermal gradients measured for each bridge, tabulated in Table 2.1, denote the effect of thickness of the surfacing. She conducted a set of analyzes to investigate the effect of thickness of surfacing on maximum thermal gradients in 6 different cross section depths, ranging between 1.5 m-0.2 m, when subjected to an extreme weather condition in the British. Various surfaces like as waterproofing membrane, asphalt cover, etc, of different thicknesses were tried and the maximum thermal gradient was ascertained.

Emerson [25, 26] noted that when the measured temperature for the bridge reached each time lows and highs, in the winter and summer respectively, the thermal gradients in the bridge were not different from those measured in the previous years. Her conclusion of this research that large negative and positive thermal gradients could happen within a daily cycle and this could occur at least 5 or 6 times a year.

Table 2.1 Temperature variations of bridges in British

Bridge Structure	Type	Depth (m)	Surfacing Thickness (mm)	Temperature Difference (^{0}C)
Adur	CBGB	1.1	64	17.0
Coldra	I-Beam	1.14	102	13.0
Mancunian	CBGB	1.3	90	14.0
Hammersmith	CBGB	2.0-2.7	92	15.0
Medway	I-Beam	2.4-2.7	57	16.0
Marlow Bishom	CBGB	1.52-4.15	150	17.0

CBGB= Concrete Box Girder Bridge

Moorty and Roeder [27] used FE method for evaluating the temperature response of concrete composite and steel bridges exposed to weather conditions. The steel girder has been modeled using 3D beam elements and the concrete deck has been modeled by utilizing plate elements. The thermal movements and temperature distribution obtained from these analytical models were then compared with the results of the measurements for the verification of the suggested method. In addition, this research discussed the effects of support conditions and variation bridge geometry on thermal responses and temperature distributions in the composite bridges.

Imbsen et al. [28] investigated the influence of different thermal gradients on a variety of effective bridge section. Their study summarizes of the variation available temperature differentials in current bridge design codes, and they recommended four variation temperature distributions for variation zones United States.

For the analysis of temperature influences in a concrete BG, Elbadry and Ghali [29] performed a parametric research for the influences of the girder geometry, bridge orientation, surface conditions and weather conditions on thermal stresses and bridge temperatures using a 2D FE analysis. Based on the research, the combination of climate and surface conditions necessary to introduce the temperature field linked to the stresses and largest curvature in the concrete BG were as the follows:

- Daily range of surrounding temperature is large

- Deck is all covered by asphalt

- One side of the BG is safeguarded from solar radiation throughout the hot season.

Later, Elbadry and Ghali [30, 31] discussed concrete cracks and tensile stresses induced nonlinear temperature gradient in a concrete bridge and introduced a minimum quantity of reinforcements so that to control the width of thermal cracks. Mirambell et al. [32] introduced an analytical model depends on a 2D finite difference method in calculate stress distributions and temperature in concrete BG bridges. In that research, they focused on the importance of transverse temperature variation between the air enclosed and the external air in the concrete box which induce tensile stresses at the inside or outside of the web and the slab of the BG.

Moreover to numerical and theoretical evaluation of the thermal conduct in concrete bridges, experimental researches were conducted by several researchers. Dilger et al. [33] also monitored the behavior of a steel composite and continuous concrete BG for a concrete deck during the period of construction and during the first three years of the operation. There were cracks reported by the field measurements in the concrete deck and also nonlinear strain distributions across the width and the depth of the steel boxes which were rates to temperature increases in the concrete deck, as well as the rapid heating of steel boxes exposed to direct of solar radiation. For the section of a double box concrete bridge, Churchward and Sokai [34] presented measurements of temperatures during period of construction, their study provided experimental expressions for average temperatures and vertical temperature profiles as a function of maximum thermal gradient depend on temperature and surrounding temperature.

Roberts-Wollman et al. [35] calculated concrete temperature data in San Antonio city, Texas over a section of a segmental BG bridge, the maximum negative and positive vertical temperature differentials measured in the study were then compared to those recommended in the AASHTO Segmental Specifications in 1999 [36], and AASHTO LRFD Bridge Design Specifications in 1994 [37]. For the positive temperature differential, the AASHTO LRFD Bridge Design Specifications (1994) exhibited large vertical gradients for the surface without a topping. The vertical gradient was measured when topped with asphalt was nigh to those of the AASHTO LRFD Bridge Design Specifications (1994). The AASHTO Segmental Specifications

(1999) showed larger vertical gradients for both conditions. Furthermore, the negative vertical temperature differentials were larger for both surface conditions when they were compared to the AASHTO Specifications in (1994, 1999). In addition, this research evaluated the relationships between the surround climatic conditions and measured girder temperatures to predict positive thermal gradients.

Relative to thermal gradients, AASHTO in 2000 [38] as shown Table 2.2, divides the USA into four zones of solar radiation, with zone four receiving the least and zone one the most solar radiation. Zone one encompasses most of the Western USA, giving the Saco bridges the thermal gradient shown in Figure 2.2. Negative thermal gradients are obtained by multiplying the positive temperatures by (-0.3). The lower amount negative thermal gradient reflects the different cooling and heating events for the bridge decks. The positive thermal gradients take place when throughout the summer the soffit is warmer less than the top of the deck; the negative thermal gradient develops on winter nights when the soffit temperature is cooler less than the deck. The event of summer develops a much larger thermal gradient than the event of winter.

T_1, T_2 and T_3 indicate temperature at the top of the bridge deck, temperature at location 0.1 m below the top of the bridge deck and temperature at the bottom of the superstructure respectively.

Table 2.2 Temperature gradients AASHTO [38]

Zone	$T_1(^0C)$	$T_2(^0C)$
1	30	7.8
2	25	6.7
3	23	6
4	21	5
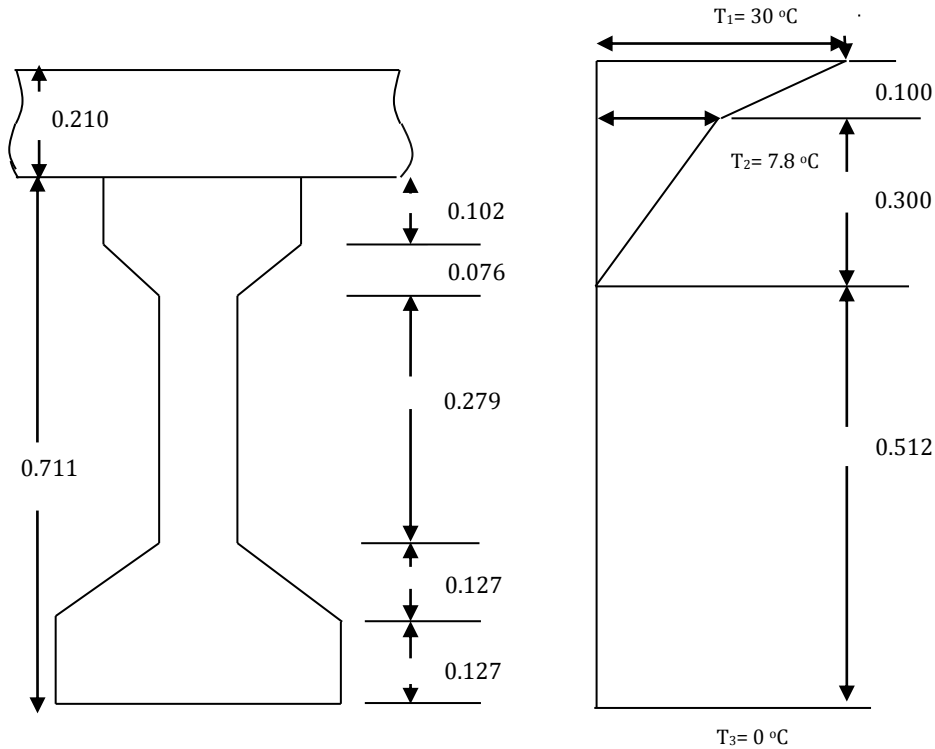
All dimensions are in meters

Figure 2.2 Saco Bridge temperature distributions (for positive temperature gradient)

Saetta et al. [39] introduced a numerical procedure depended on the FE method for expecting stress levels and temperature variations in a concrete BG bridge and a concrete dam. Assuming stress fields and uncoupled temperature, this study first measured the temperature field by a concrete structures consisted from internal heat generation and climate boundary conditions. The acquired temperature field was including transferred thermal loads in the stress-strain analysis that depended on the linear elastic conduct of material. For the validation and effectiveness of the suggested numerical method, the results obtained in that research were compared with the empirical results that reported in the literature.

Suchinda and Will [40, 41] developed a new method for predicting the temperature conduct of fiber reinforced polymeric demonstrated and V-shaped bridge decks the need to consider temperature response caused climate conditions in the design. In the research, a 2D heat transfer FE analysis using calculated climate boundary conditions has been performed to determine temperature distributions in the superstructure deck. The gained temperature distributions have been transferred to a temperature stress analysis using movements, shell elements and deck temperatures were predicted. Furthermore, parametric research to demonstrate the effect of the heat emissivity and solar absorptivity of the fiber reinforced polymeric plate on temperature responses was conducted.

Gilland and Dilger [42] measured temperature differences, ambient air temperature, wind speed and solar radiation during the period of construction of the Confederation Bridge, a PC BG situated in Atlantic, Canada. Temperature data appeared that prior to the removal of the formwork, concrete temperatures sounded to gradually increase because the heat of hydration. After the formwork has been removed, the concrete members experimented sudden temperature differentials because their exposure to surrounding climate conditions.

Roeder [43] was collected a significant quantity of data for both the Utah and California Bridges and was compared to the minimum and maximum design recommendation maps stipulated in the AASHTO LRFD Specifications in 2010 [44]. Showed this map that bridges often be designed for less movements than desired by the AASHTO Specifications in 1996 [45]. The minimum and maximum average temperatures of the Utah and California Bridges were expected with 17 % and 27 %, respectively.

Li et al. [46] analyzed the temperature response of the Confederation Bridge depended on experimental data for three sections approximately 4.5 m, 8.7 m and 13 m deep. They used the Extreme Value Analysis (EVA) to obtain 100 year return thermal loads. The EVA results were compared with the Canadian code (CAN/CSA-S60-00) [47] and with the Priestley model [11]. They found that the Canadian code gives a fairly good estimate for average temperatures but underestimate the positive linear differential temperatures by about 20 %, the 4.5 m deep bridge section showed Priestley model in the hot season was good agreement, but the other two deeper

sections shown lower temperature in the slabs and higher temperature in the web. The Priestley model based on, this study suggested a modified third-order vertical temperature differential for extremely deep prestressed girder sections.

Lee, [48] carried out analytical and experiment study on precast PC bridge girder to investigate the thermal influences on girder. An experimental research on PC girder segment in Georgia evaluated and identified variations in lateral and vertical temperature differentials in the girder with change in the climate conditions. The author found the largest vertical temperature differentials was in the summer, the intensity of the solar radiation was the highest on the top surface of the girder. With an increase in intensity of solar radiation on the vertical surface, the largest lateral temperature differentials were in the winter and late falls. He determines the magnitudes of the temperature differentials with variation in meteorological conditions and using the FE package ABAQUS [49] based on 2D FE heat transfer analysis model. Also introduced a simple method depended on 1D beam theory to compute thermal deformation reductive by lateral and vertical thermal gradients. The vertical deformation has been computed using a vertical temperature differential along the web heights of a PC concrete girder; the transverse thermal deformation has been computed using three transverse temperature differentials in the middle width of the top flange, across the web and along the bottom flange, respectively.

Wang and Fang [50] studied the temperature difference of concrete BG bridges. In that research, they used the commercial FE-program ANSYS based on 2D FE analysis and depend on measurement filed on a PC BG bridge in China. They reported that their FE model temperatures in conjunction with the recorded ones within a maximum error of 3.

Zhang et al. [51] utilized the ANSYS APDL parametric in the design language to development a secondary visual module for the analyzing of temperature field in PC BG. Comparative research with field measurements of a changeable section PC BG bridge exhibited that the used FE simulation can objectively express the actual boundary conditions with higher accuracy and can meets the requirements of practical analysis and design in engineering.

Carboni and Lacarbonara [52], used the FE multi-physics package COMSOL [2] investigate in the thermo-elastic-dynamic conduct of concrete BG bridge. A 3D model was simulated to assess the temperature field because solar radiation and climate exposure and its influences on the normal frequency of the bridge. They observed in summer negative differences of the natural frequencies because the heating of the structure, which reach a maximum around 3:00 pm. While, in winter, positive differences were observed because the cooling of the structure in the early hours of the day even 9:00 am, beyond which the difference start to decrease up to about 3:00 pm.

2.3 Proposed and Design Thermal Gradient

Based on Maher experimental studies in the Australia and United Kingdom, Maher [9] suggested a linear temperature variation for concrete BG sections. He proposed variations only during the flange section i.e. the deck slab of the bridge, since he thought that they have been the most significant. The distribution is shown in Figure 2.3.
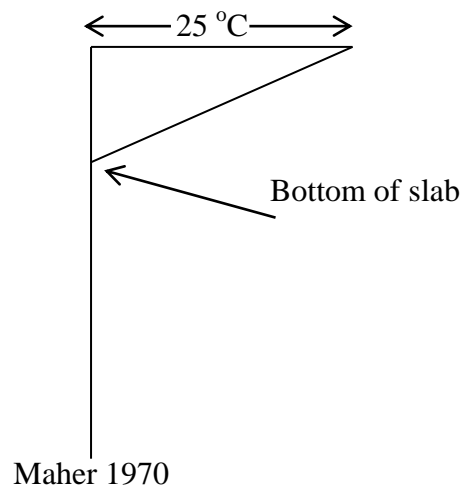
Figure 2.3 Temperature distribution proposed by Maher [9]

Since initially suggested by Priestley in 1972 [8] to the New Zealand Code of Practice New Zealand Ministry of Works Department (NZMWD) and largely as a result of the found thermally caused by damage to the Newmarket Viaduct, the difference was modification from a simple increase in the deck slab to a nonlinear sixth order curve, design thermal gradient for sections greater than 1220 mm deep

and decreasing to a zero at a depth of 1390 mm regardless, of the section. In addition a parametric study and research of seven typical New Zealand bridge sections exhibited that the critical case could be adequately expected by a fifth-order curve distribution, Priestley [11]. The revised thermal gradient consists of fifth-order curve expending from the upper surface to a maximum depth of 1200 mm which is suiting for slabs, T-beams, web members and cantilevers of BG sections. Also, a linear temperature distribution is applied to the bottom 200 mm of all sections. For concrete above closed air cells, a linear increase in temperature is determined for representation the insulating influence of the air cell as illustrated in Figure 2.4. Priestley proposed that this revised temperature gradient would lead to a significant reduction in the soffit tension stress level. This difference has now been accepted by the (NZMWD) for all main concrete bridges designed.

$$t_y = 30(y/1370)^6 \,^0C$$

$$t_y = T(y/1200)^5 \,^0C$$

$$t_{y`} = 5-0.05\, h \,^0C$$

$$T = 32-0.2\, h \,^0C$$

h = black top Thickness (mm)

NZMWD 1970   NZMWD 1973   NZMWD 1977
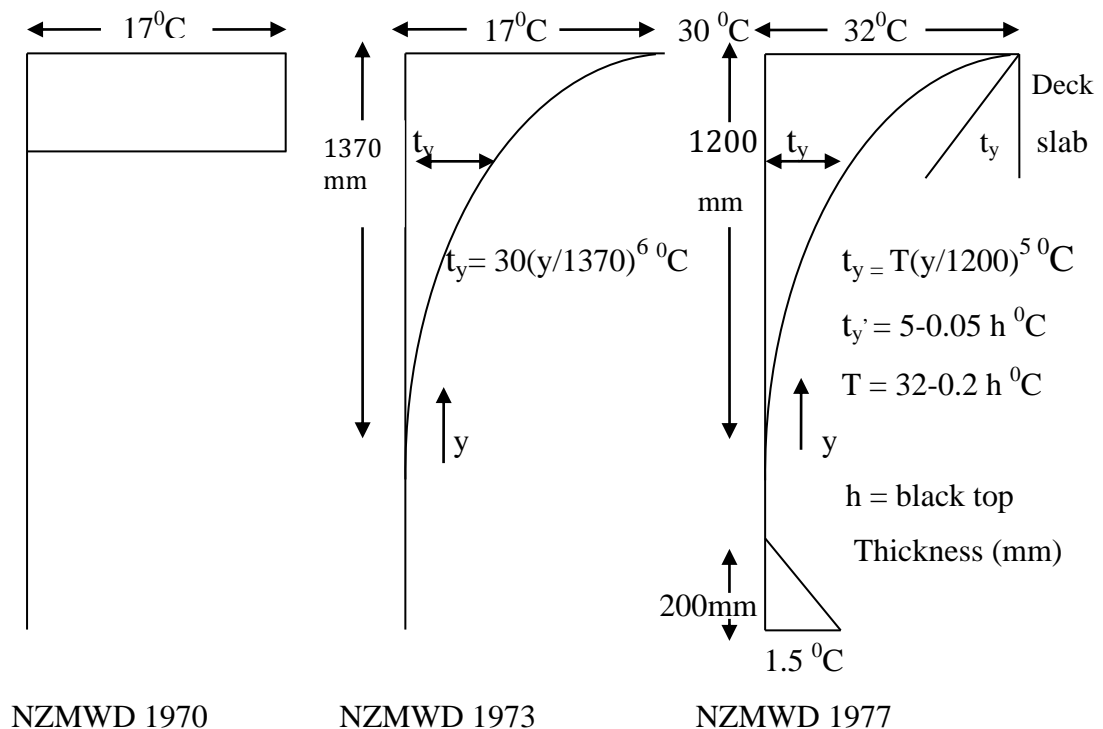
Figure 2.4 Temperature gradients proposed by the NZMWD [10, 53, 54]

In the United Kingdom prior to 1973, the concrete bridges were designed for a maximum temperature variation of 8.3 ^oC, linear during the section. Emerson [23], indicated that this was inadequate a nonlinear temperature difference depend on twelve years of location measurements on seven bridges with different depths, in Wales and England was adopted. The effect of the surfacing layer was included by use of a modified in the calculations. In 1978 various straight line format depend on

further study by Emerson [25] was suggested in the design loading document BS5400. Allowances have been made for the influence of surfacing. These temperature distributions are depend on the extreme weather conditions throughout the twelve year period and could be extensive in the future. As shown in Figure 2.5 the various thermal gradients in the British standards code.

8.3 ^{0}C   13.5 ^{0}C   13.5 ^{0}C

500mm

d_1

d_2

D

d1=0.3m<150mm

d2=0.3m>100mm

<250mm

d3=0.3<100mm

+blacktop thickness

D/3

2.5 ^{0}C   2.5 ^{0}C

BS153 1972   Emerson 1977   BS5400 1978
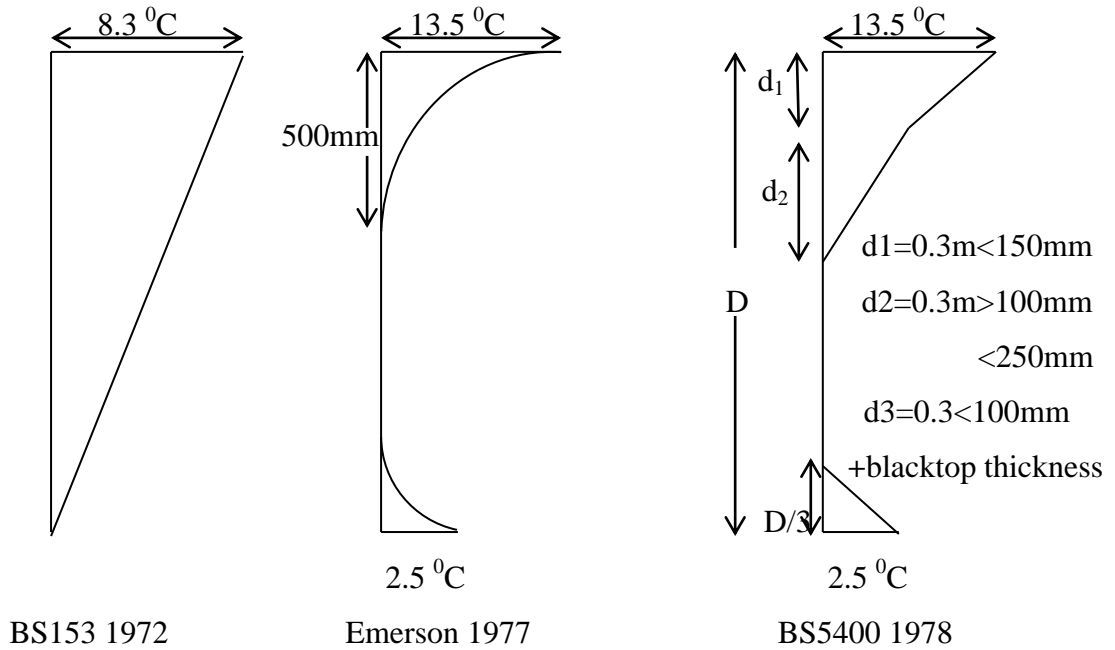
Figure 2.5 Thermal gradient adopted by the United Kingdom code and by Emerson [25]

17

CHAPTER 3

HEAT TRANSFER IN BRIDGE GIRDERS

3.1 General

In general, the analysis of heat transfer in bridges is a 3D problem. In a bridge with constant cross-sectional dimensions along the span length, the temperature can be considered constant over the bridge length but varies along the depth and across thickness of the sections.

Temperature distribution in a structure depends on time and upon the cross sectional geometry, the geographical location and orientation of the longitudinal axis of the bridge, which defined by the latitude, longitude and azimuth angle, in addition it depends on the properties of the materials, namely solar radiation absorption coefficient, surface emissivity, material density, specific heat, thermal conductivity and the surface convection coefficient. It also a function of the time of the day and the season, climate conditions including daily variations of air temperature, wind speed, and clearness of the sky. Moreover, during the early days of concrete, the heat of cement hydration is an additional internal thermal load.

3.2 Basic Equations of Heat Transfer

The conduction of heat through the girder volume is governed by the Fourier heat transfer differential equation, The general differential equation of heat flow in three dimensions is [55]:

$$\frac{\partial}{\partial x}\left(k_x \frac{\partial T}{\partial x}\right) + \frac{\partial}{\partial y}\left(k_y \frac{\partial T}{\partial y}\right) + \frac{\partial}{\partial z}\left(k_z \frac{\partial T}{\partial z}\right) + Q = \rho c \frac{\partial T}{\partial t} \qquad (3.1)$$

Where: k_x, k_y, k_z are thermal conductivities in x, y and z direction. The unit of k is $W/m°\mathrm{C}$. Typical values for concrete, steel and asphalt.

T is the temperature at any point (x, y, z) at any time, t

Q is the amount of heat generated within the body (e.g. by hydration of cement) per unit time per unit volume, W/m^3

ρ is the density in kg/m^3

C is the specific heat capacity in $J/kg°C$

The thermal loads applied on the boundaries of the concrete girder can be represented by

$$k\frac{\partial T}{\partial n}l + q_c + q_s + q_g + q_r = 0 \tag{3.2}$$

In which, q_c is the convection heat change between the bridge surfaces and ambient air

$$q_c = h_c(T_s - T_a) \tag{3.3}$$

Where h_c is the convection coefficient in $W/m^2°C$, T_s is the surface temperature of the girder, and T_a is the temperature of the surrounding air. In this research the formula shown in Eqn. (3.4) (Lee, 2010) was used, in which v represents the wind speed.

$$h_c = \begin{cases} 5.6 + 4.0v & (v \le 5\,m/s) \\ 7.2v^{0.78} & (v > 5\,m/s) \end{cases} \tag{3.4}$$

q_g is heat absorbed from solar radiation, where,

$$q_s = aI_s \tag{3.5}$$

Where a is the surface absorptivity of the girder surfaces, while I_s is the solar radiation flux on a horizontal surface.

q_r is the radiation reflected from the ground and the surroundings (albedo)

$$q_r = \epsilon\sigma(T_s^4 - T_a^4) \tag{3.6}$$

q_r is the heat emitted from the surfaces of the bridge by log-wave radiation, ϵ is the surface emissivity, and σ is a constant equals $5.67 \times 10^{-8}\,W/m^2K^4$ (Stefan-Boltzmann constant).

3.3 The Comparative Study

Heat transfer problems that include solar radiation, other irradiation sources, surface radiosity, and convection cooling in addition to conduction have many detailed boundary conditions. To well define all these boundary conditions and thermal loads, many detailed inputs are required. Some of these inputs are time-dependent like ambient air temperature and wind speed. Others are time-independent, such as bridge layout and geographical information like latitude, longitude and time zone. Also, the materials thermal properties like thermal conductivity; specific heat, emissivity and absorptivity should be well defined. Geometry of cross-section plays an important

role in the problem and need to be accurately defined. All these parameters make it somewhat difficult to find some suitable study in the literature for comparison purpose compared with the conventional structural problems with static or dynamic loads. However, an experimental study on a segment of a precast concrete girder with the required details was found and is used in this study for verification purposes.

3.3.1 Definition of the case study

Due to the availability of almost all of the required input data, an experimental and numerical study carried out at Georgia Institute of Technology in Atlanta/USA by Lee [48] was chosen for comparison purposes. In this study a five-foot length of the standard AASHTO BT-63 prestressed concrete girder was used in the experimental part as shown in Figure 3.1. On the other hand, the FE program ABAQUS [49] was used to simulate the problem and carry further structural and parametric studies
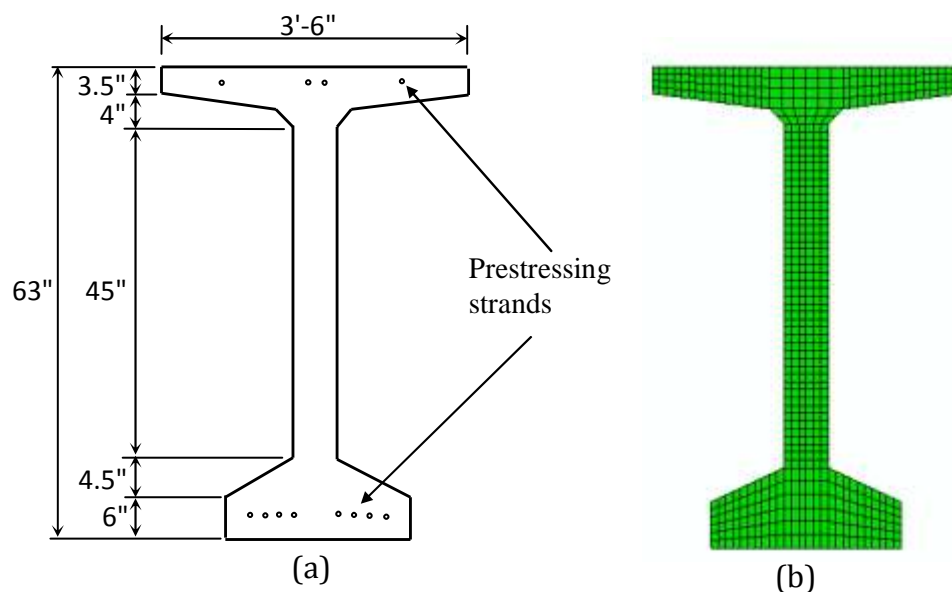
Figure 3.1 Cross-sectional details and FE mesh of the test specimen [48]
(a) experimental model and (b) FE mesh

A total number of 28 interior and surface thermocouples were installed at the mid span of the specimen as shown in Figure 3.2. Two pyrometers were used to measure the intensity of solar radiation on the vertical and horizontal surfaces of the girder. To measure wind speed, anemometer was installed above the surface of the top flange.

The latitude of the test location is $33^o46'N$, while longitude is $84^o23'W$ and time zone is -5. The longitudinal axis of the girder lies on the East-West direction while vertical web surfaces face the north and south direction. Because of the difficulty of measuring thermal properties of concrete, the author chose some recommended values from the literature and used it in the FE model. The used thermal conductivity, specific heat, and concrete density were $1.5\ W/m\ K$, $1000\ J/kg\ K$, and $2400\ kg/m^3$ respectively. The emissivity and absorptivity coefficients were assumed to be 0.85 and 0.5 respectively.
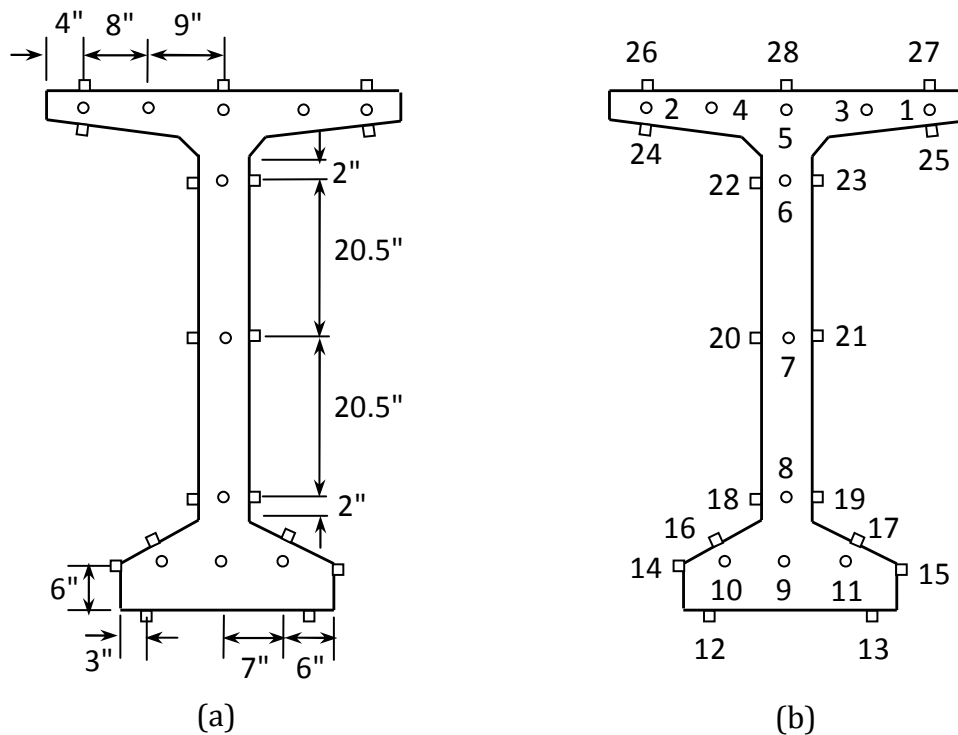
Figure 3.2 Thermocouple (a) locations and (b) numbers [48]

The author chose three days to present his experimental results; these are, June 1st, October 1st, and November 15th. While in the presenting of the numerical study, only the June 1st and the November 15th were chosen. Figures 3.3 and 3.4 below show the measured hourly air temperatures and wind speed respectively, while Figure 3.5 shows the measured solar radiation intensities.
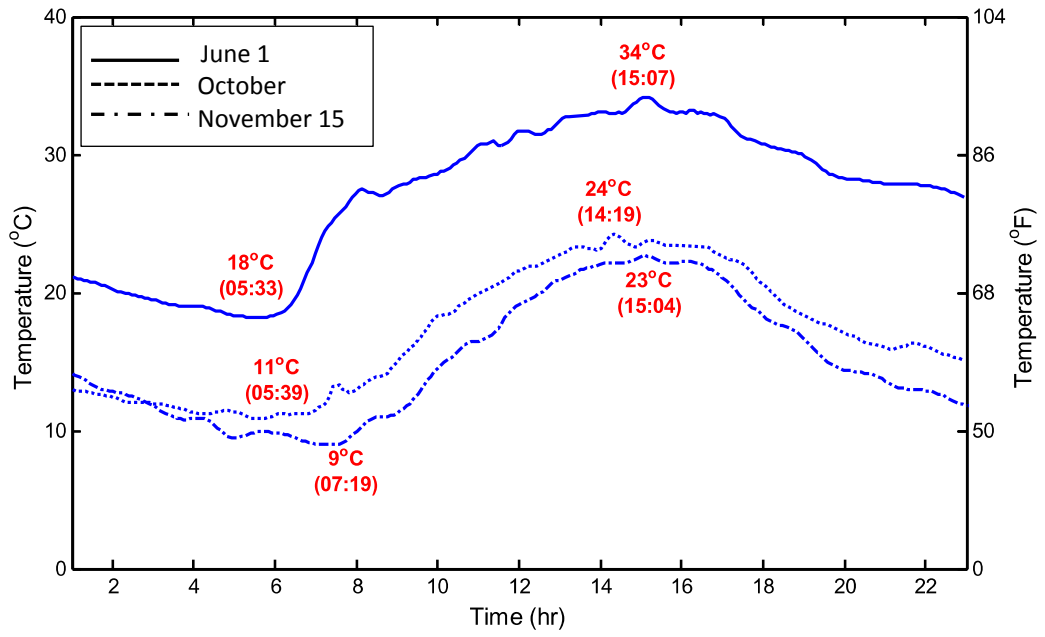
Figure 3.3 Hourly air temperatures for the chosen days [48]
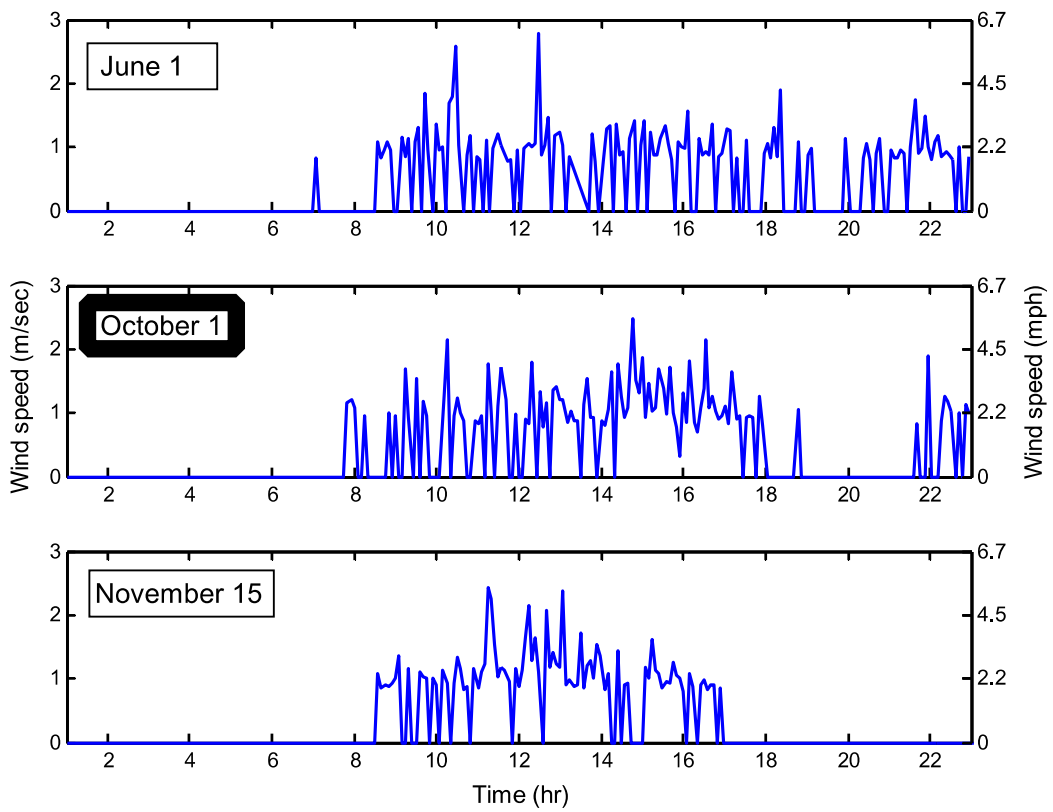
Figure 3.4 Recorded wind speed for the chosen days [48]
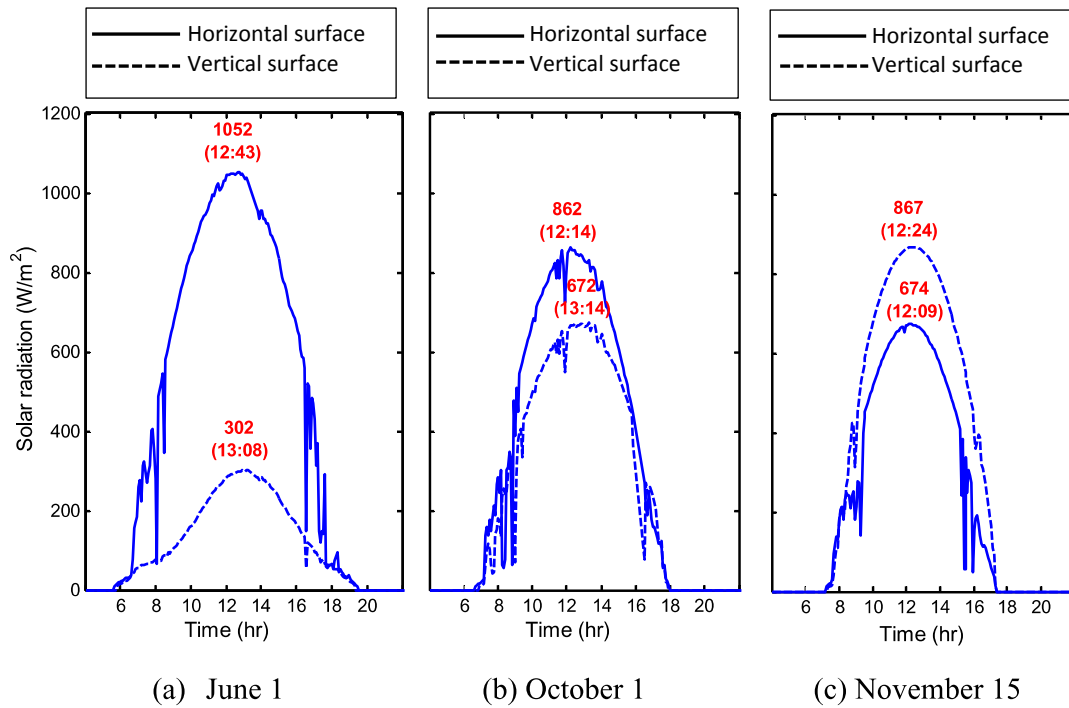
Figure 3.5 Measured solar radiation on vertical and horizontal surfaces [48].

To calculate the convection coefficient h_c based on wind speed v, was used a formula proposed by Saetta et al. [39] which is as follows:

$$h_c = 5.6 + 4.0v$$

(4-1)

The initial temperatures were considered to be 29.7 ℃ for June 1st and 19.3 ℃ for November 15th.

3.3.2 Experimental and FE results of the case study

In this section some initial results of the experimental and numerical parts from reference [48] are presented. These results include temperature distribution for the whole chosen days for specific thermocouples and sectional temperature distributions for specific times.

Figures 3.6 through 3.8 show the measured and predicted temperatures variations at different thermocouples locations on June 1st. While Figures 3.9 through 3.11 show the temperatures variations at different thermocouples locations on November 15th.

23
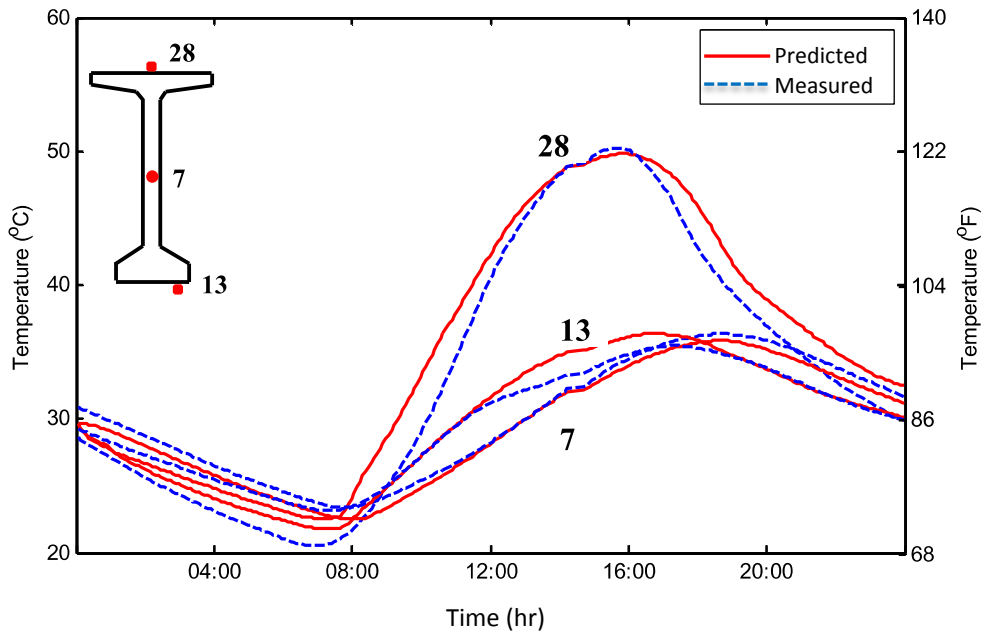
Figure 3.6 Temperature variations at thermocouples 7, 13, 28 on June 1st [48]
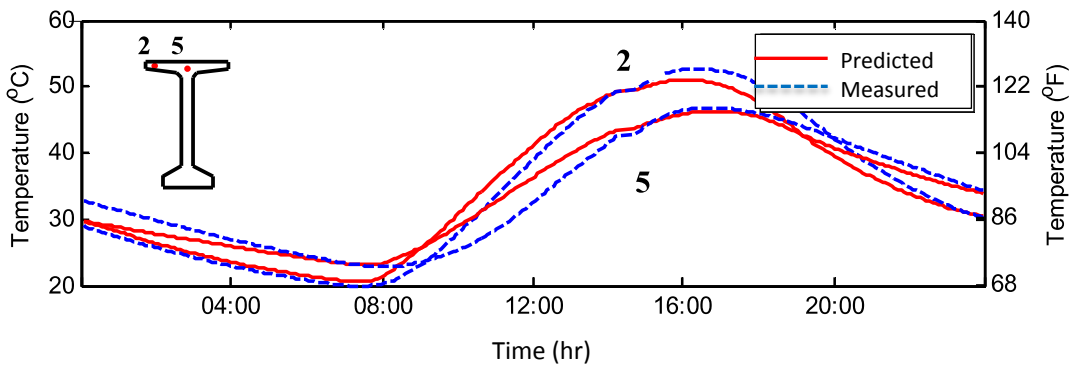
Figure 3.7 Temperature variations at thermocouples 2 and 5on June 1st [48]
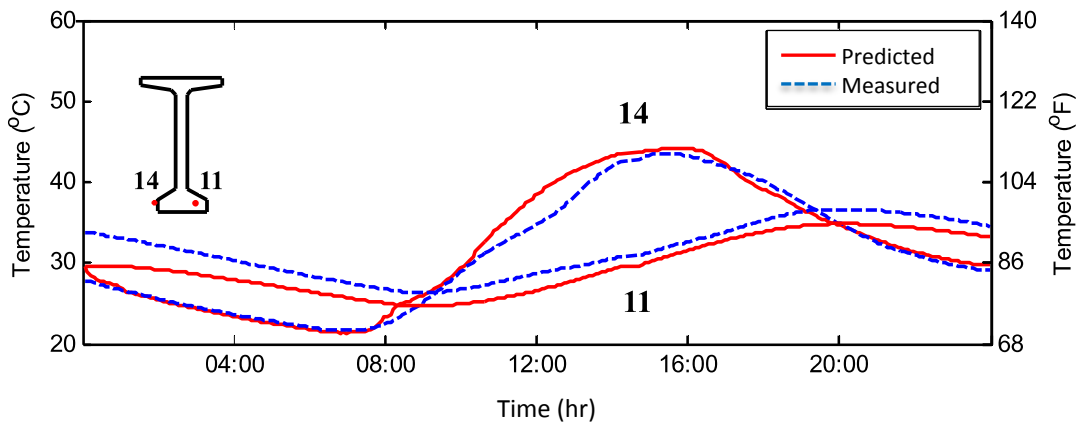
Figure 3.8 Temperature variations at thermocouples 11 and 14 on June 1st [48]

24
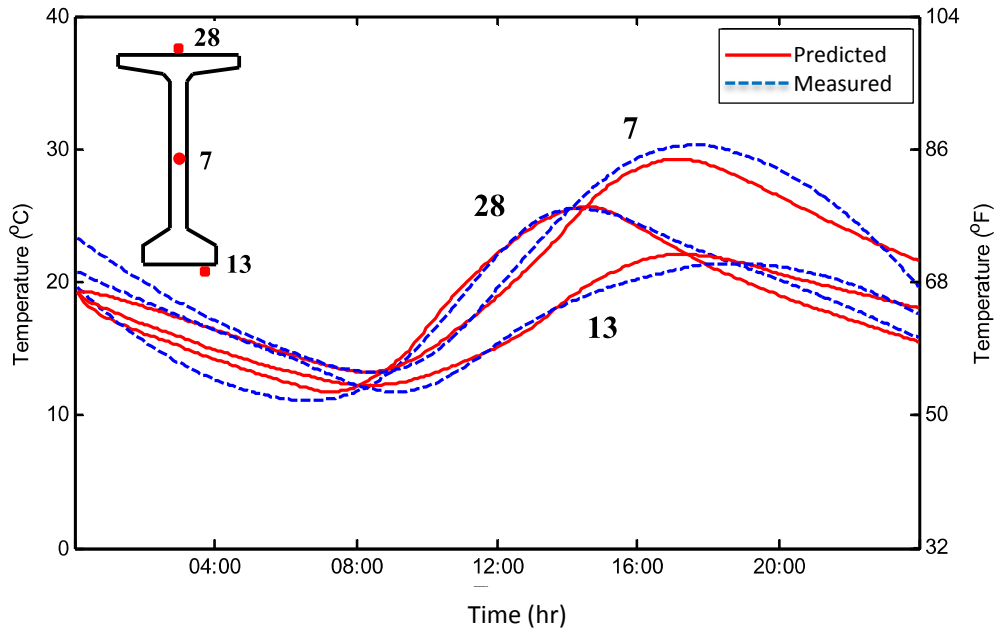
Figure 3.9 Temperature variations at thermocouples 7, 13, 28 on November 15th [48]
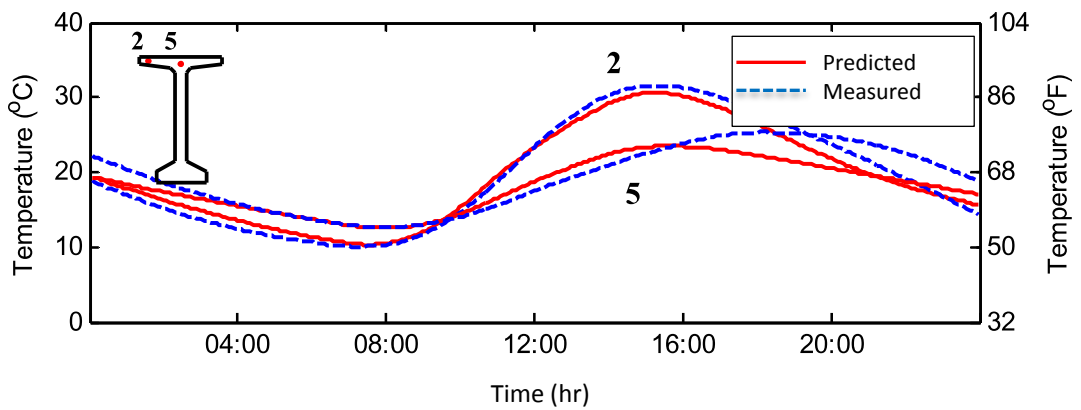
Figure 3.10 Temperature variations at thermocouples 2 and 5 on November 15th [48]
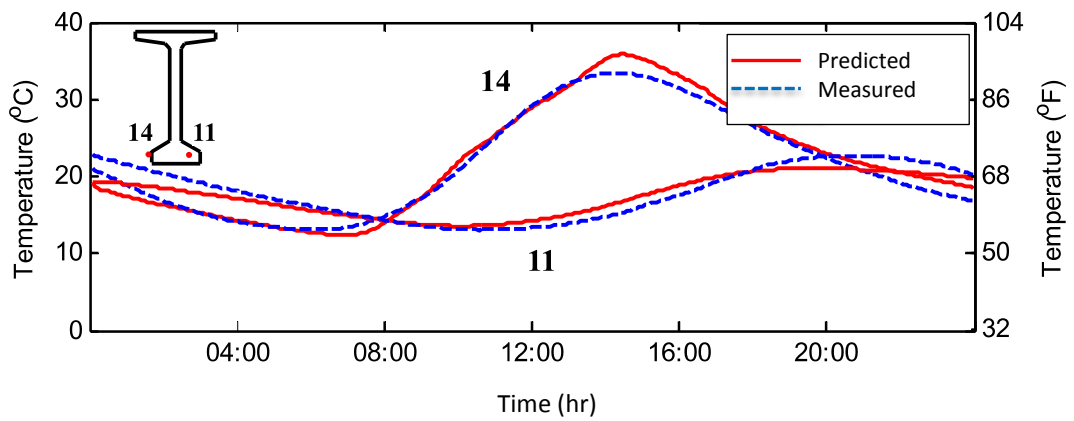
Figure 3.11 Temperature variations at thermocouples 11 and 14 on November 15th [48]

Figure 3.12 shows selected temperature contours on the whole cross section on June 1st, while Figure 3.13 shows the temperature contours on November 15th.

(a) 6:28 a.m.   (b) 1:42 p.m.
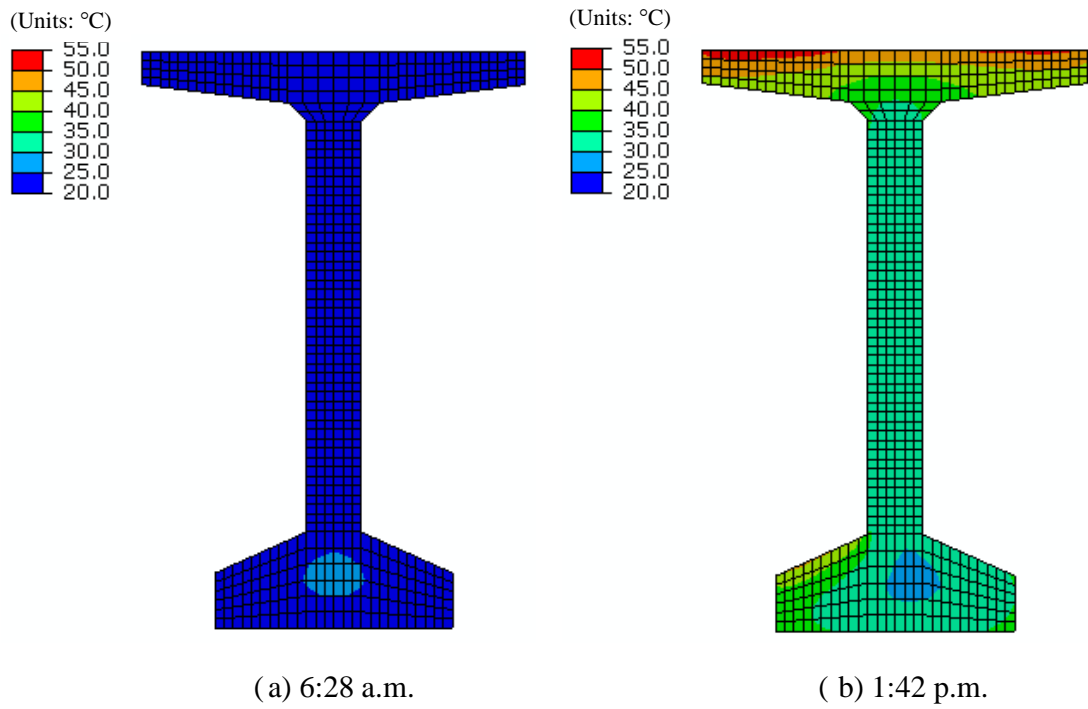
Figure 3.12 Temperature contour plots on June 1st [48]

(a) 7:35 a.m.   (b) 1:35 p.m.
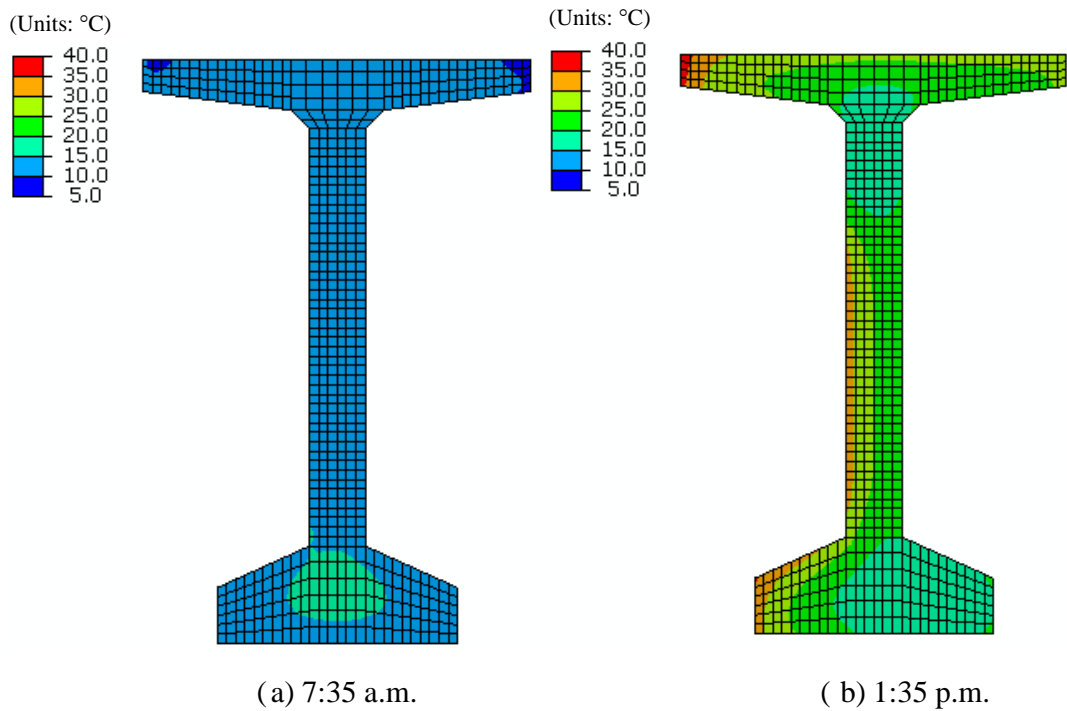
Figure 3.13 Temperature contour plots on November 15th [48]

26

CHAPTER 4

MODELING WITH ANSYS

4.1 General

Since the temperature has been considered to be constant along the span of straight girders because of the constant boundary conditions, the heat transfer problem can be simulated using a 2D model. Therefore, using ANSYS a 2D model was considered. Considering the 2D and 3D problems, thermal radiation in ANSYS can be modeled using three techniques. The first two methods are the AUX12 radiation matrix method and the Grandiosity solver method, both are used for more generalized radiation problems were surface-to-surface radiation (two or more surfaces) is considered. The third method is an easier method that is used to simulate radiation between a surface and a point. The third method is the one recommended by ANSYS to simulate the surface-to-ambient radiation of a surface, where the node can be considered as the ambient that receives temperature from the hot surfaces. The third method requires the use of the surface effect elements SURF151 and SURF152 for 2D and 3D models respectively. These surface elements work as a skin above the used thermal plane or solid elements to apply all types of boundary conditions without having any physical properties (thickness) that may affect the solution.

4.2 Element Types and Load Procedure

2D PLANE77 element was used to model the thermal conductivity and SURF151 surface effect element was used to apply the solar radiation, convection, and surface-to-ambient radiation boundary conditions. The used load application technique depends on the measured solar radiation data and do not calculate solar position and the resulted radiation intensity because this needs further programming and writing a special subroutine. The author measured the intensity of solar radiation on the top face of the top flange and on one of the vertical sides of the web as shown in Figure 3.5. Therefore and because of the lag of information about the solar radiation

intensity on the second vertical face of the web, the solar radiation was considered to symmetric and equal at both sides.

The method of the overall heat transfer coefficient was used to apply both convection loads q_c and solar radiation load q_s as convection load only with an integrated ambient air temperature as follows:

$$q = q_c + q_r - q_c \qquad (4.1)$$

Where q_r represent the surface-to-ambient radiation of the surfaces which can be calculated using the extra node with the surface effect element or rounded using suggested empirical formulas. The top equation can be re-written as shown below to exclude q_r from the calculation of the integrated air temperature.

$$q = q_o + q_r \qquad (4.2)$$
$$q_o = q_c - q_s = h_c(T_s - T_a) - a.I \qquad (4.3)$$
Thus:
$$q_o = h_c[T_s - T_a - a.I/h_c] \qquad (4.4)$$
Or:
$$q_o = h_c(T_s - T_{as}) \qquad (4.5)$$
Where
$$T_{as} = T_a + a.I/h \qquad (4.6)$$

The integrated air temperature T_{as} was calculated for each time step and q_o was applied as a convection tabular load.

Actually, even that the axis of the beam lies on the east-west direction, in fact the solar radiation is not the same on the northern and southern faces. The distribution and amount of difference depends on the season of the year and the time of the day.

4.3 Results of the ANSYS Model

Figures 4.1 and 4.2 show the temperature contours of the girder section on the first of June. Figure 4.1 describes the temperature variation across the section at the early morning at 6:28 am. It is shown that temperatures ranges between about 20.6℃ and about 25.5℃, similar results can be observed in Figure 3.12, where temperature ranges from about 20.6 ℃ to about 27.1 ℃. Another notice is that the maximum

temperature located at the center of the bottom flange and the minimum temperature concentrates at the outer parts of the top flange as can be obviously shown from Figure 4.1 and 3.12. Note that the color grading used in the ANSYS model is more accurate than the one used by the author, since nine colors are used to describe a 5 ℃ temperature difference, while the author used only one color for each 5 ℃.

As shown in Figure 4.1, the temperature distribution describes the end time of cooling process and start time of solar heating. Figure 4.2, on the other hand, describes a time step where solar heating reaching its ultimate stage. The external surfaces and especially the top horizontal surface suffer direct solar radiation heating, which raises the temperature of these surfaces compared to the interior cores. On the other hand, the core of the bottom flange where the concrete mass is maximum shows the minimum range of temperature. This is due to the weak thermal conductivity of concrete compared to its specific heat.

As mentioned in the previous chapter, the used thermal conductivity is 1.5 $W/m.K$ while the specific heat is 1000 $J/kg.K$, compared with metals like carbon steel where the thermal conductivity is about 50 $W/m.K$, and specific heat is about 500 $J/kg.K$. The temperature contour plot, shown in Figure 4.2 shows a good agreement with the compared one shown in Figure 3.12.

The temperature ranges from 30.2 ℃ to 52 ℃ with maximum at the top surface of the top flange and minimum at the core of the bottom flange. The resulted temperature distribution is very close to the measured temperature distribution, where the measured temperatures range from 30.6 ℃ to 50.9 ℃, while the range of the ABAQUS predicted temperatures was from 29.7 ℃ to 49.3 ℃.

Thus, the difference between the ANSYS predicted temperatures and measured temperatures is acceptable enough compared with the difference of the ABAQUS predicted temperatures shown in Figure 3.12 and measured temperatures. One important difference between the ANSYS model and the compared ABAQUS model is that temperature loads were assumed to be symmetric on both the southern and the northern sides of the web, while in fact it is not symmetric as shown in Figure 3.12. Actually, the northern side worms more than the southern side in summer during the first hours of the morning and the last hours before the sunset. This is due to the

complicated movement of the sun, which will be discussed later in the chapter 5.
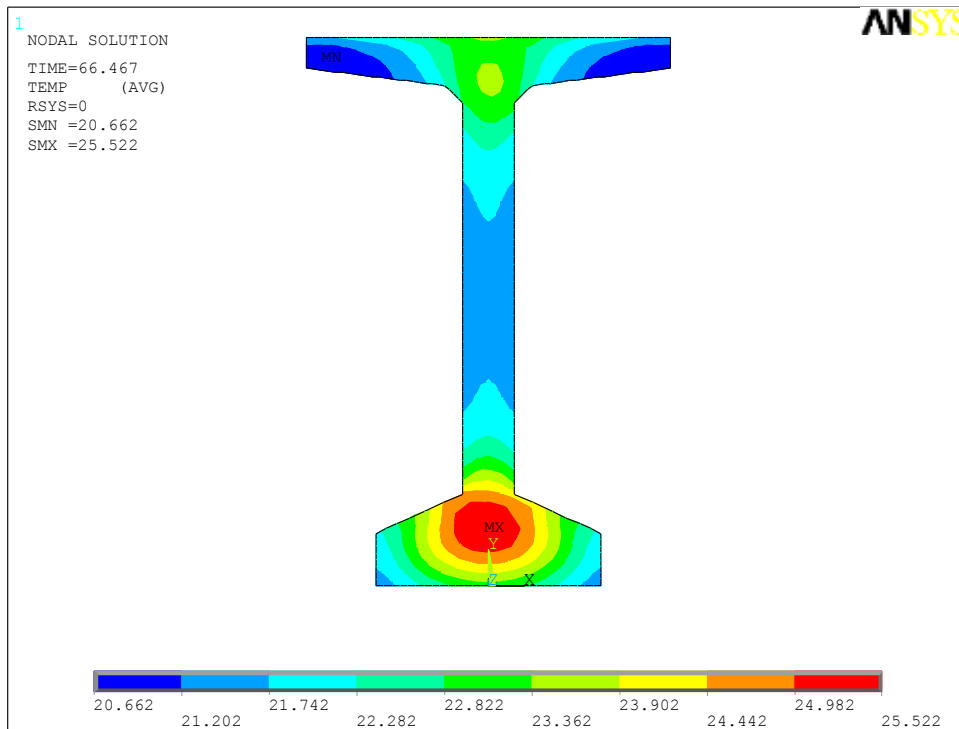
Figure 4.1 Temperature contour plots on June 1st at 6:28 am
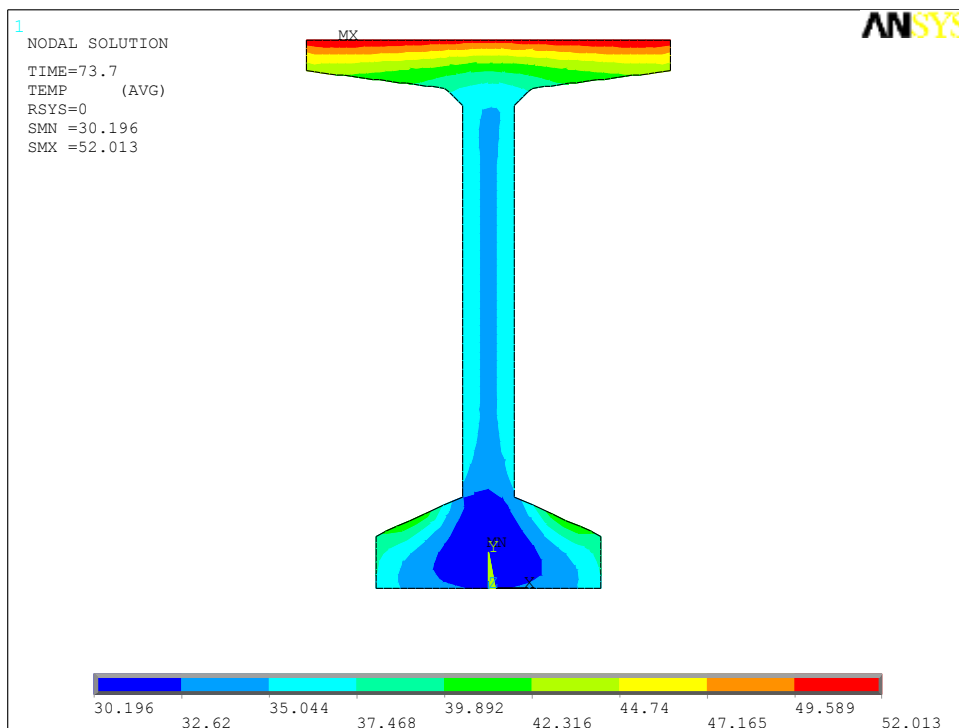
Figure 4.2 Temperature contour plots on June 1st at 1:42 pm

Figures 4.3 to 4.6 show the temperature variation at specific thermocouple locations during the full 24 hours of the first of June. A simple comparison of these temperature variations with the corresponding variations of the comparative model shown in Figures 3.6 through 3.8 reveals that the ANSYS model temperature results agree fairly with the measured temperatures and the compared ABAQUS temperature results. Figure 4.3 shows the temperature variation at the location of thermocouples 7, 13 and 28. When it is compared with Figure 3.6, it is noticeable that the behavior is almost the same for the three thermocouples. Also, the maximum and minimum temperature values fairly agree with those of the compared ABAQUS model results and the measured temperatures. Similar behavior agreements can be noticed for thermocouples 2 and 5 by the comparison between Figures 4.4 and 3.7. Even the inflection points and the curves intersections seem to be at the same time-temperature positions. Comparison between Figure 4.5 and 3.8 at thermocouples 11 and 14, obviously show that both the ANSYS 2D model and the ABAQUS 2D model temperature results follow the same behavior of the field measured temperatures. Figure 4.6 summarizes the temperature variations at thermocouples 2, 5, 7, 11, 13, 14 and 28 on June 1st.
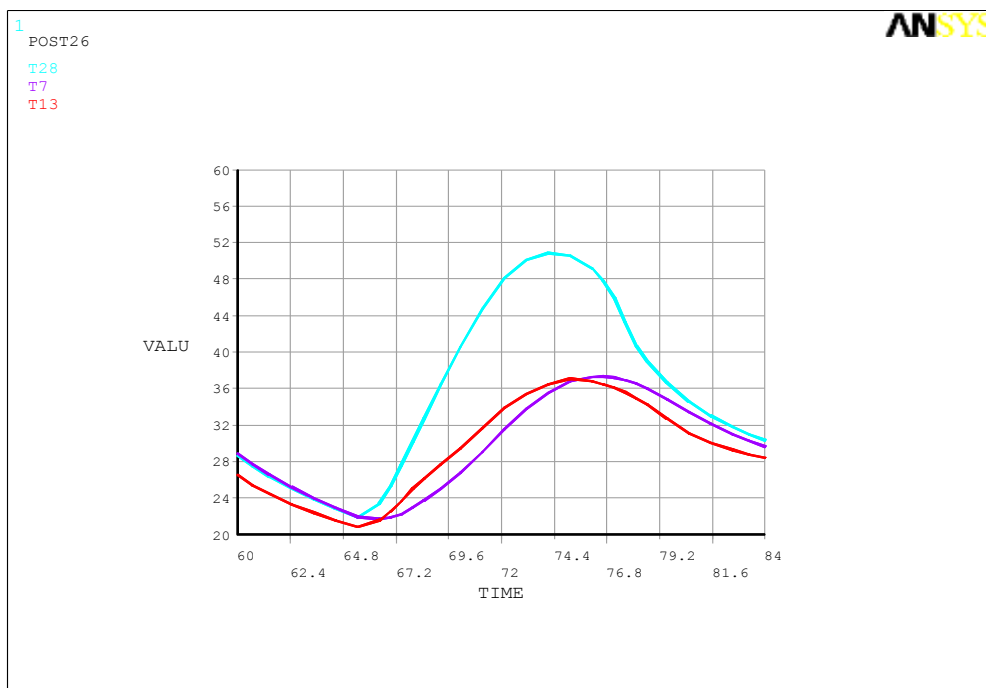
Figure 4.3 Temperature variations at thermocouples 7, 13, 28 on June 1st
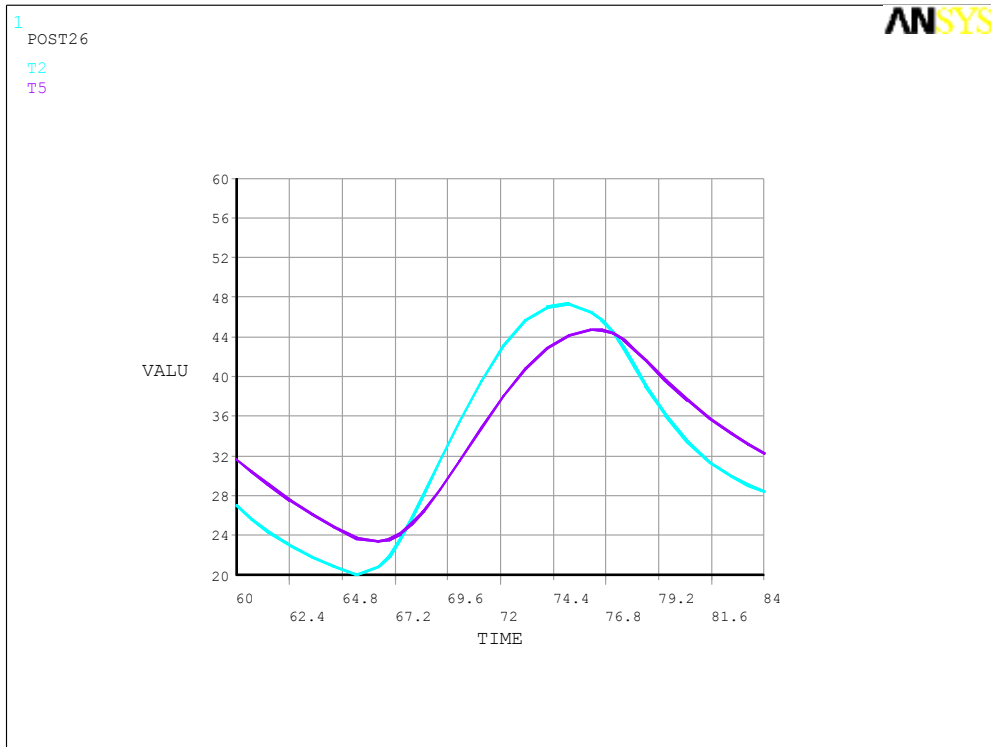
Figure 4.4 Temperature variations at thermocouples 2 and 5 on June 1st
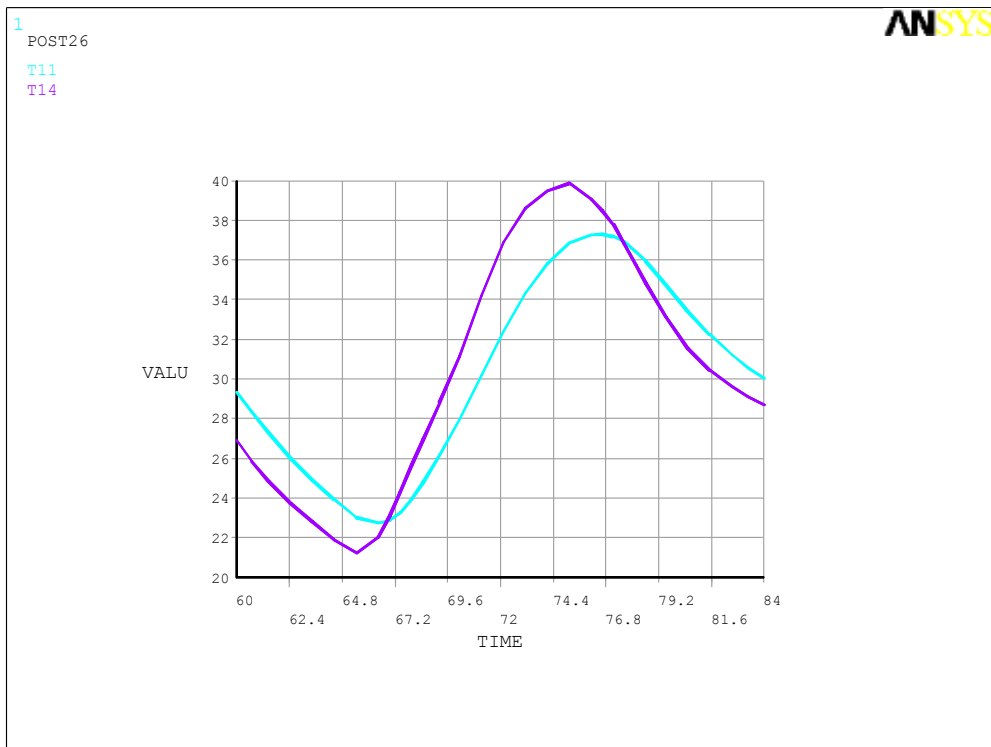
Figure 4.5 Temperature variations at thermocouples 11 and 14 on June 1st
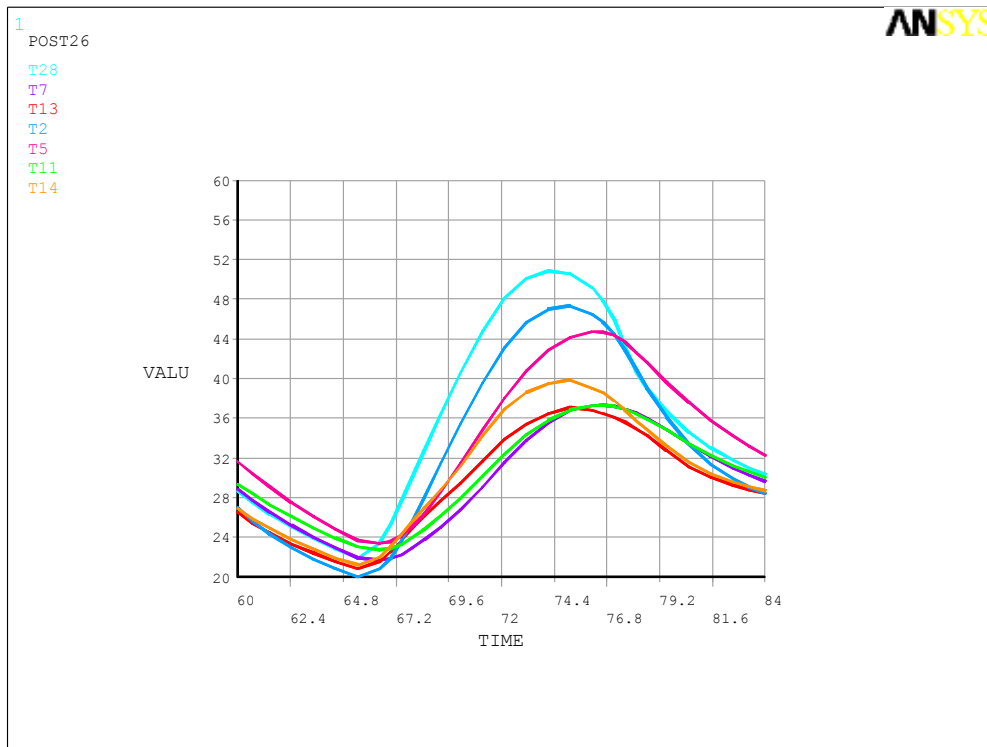
Figure 4.6 Temperature variations at thermocouples 2, 5, 7, 11, 13, 14 and 28 on June 1st

The minor differences between ANSYS results with the compared field measurements and ABAQUS numerical study results can be attributed to the simplified load application technique and the assumptions that were used in the modeling of this girder using ANSYS.

CHAPTER 5

MODELING WITH COMSOL MULTIPHYSICS

5.1 General

One of the features that COMSOL 4.3a is the division of the different physical problems into physics or modules; each contains various sub-branches depending the type of the problem. The heat transfer module includes several branches, among which is the radiation heat transfer branch, which in turn contains four main sub-branches, among which is the heat transfer with surface-to-surface radiation. COMSOL 4.3a was used to model the same AASHTO BT-63 prestressed concrete girder segment described in Chapter 4. The heat transfer with surface-to-surface radiation node in COMSOL 4.3a has a built-in solar model. Using this solar model, the sun position, sun movement, and the resulted solar radiation fluxes can be automatically accurately calculated and applied on the modeled girder. The solar radiation applied as an external radiation source and is applicable for three-dimensional problems only. Therefore, the AASHTO BT-63 PC girder segment was modeled using a 1m span length.
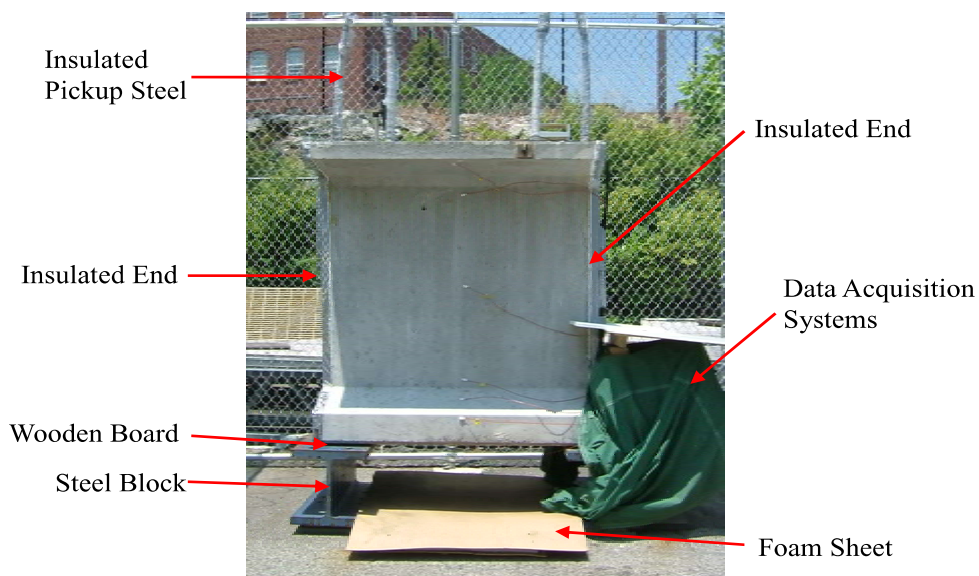
Figure 5.1 The experimental girder segment [48]

To eliminate the impact of the modeling criteria on the results, the end cross-sectional faces of the girder were considered as thermally insulated. The modeling criterion simulates the real experimental segment, where the segment has a limited span and extruded polystyrene sheets thermally insulated the end cross-sectional faces as shown in Figure 5.1.

5.2 Seasonal and Daily Sun Movement

Before presenting the model results, an important solar factor should be discussed which is the change of the daily sun movement. The position of the sun plays an important role on the received incident intensity and distribution of solar radiation on the surfaces of the bridges. This position for a specific point on the earth surface globally differs yearly from season to season and daily from hour to hour. Figure 5.2 illustrates the difference of the daily sun movement between the different seasons.
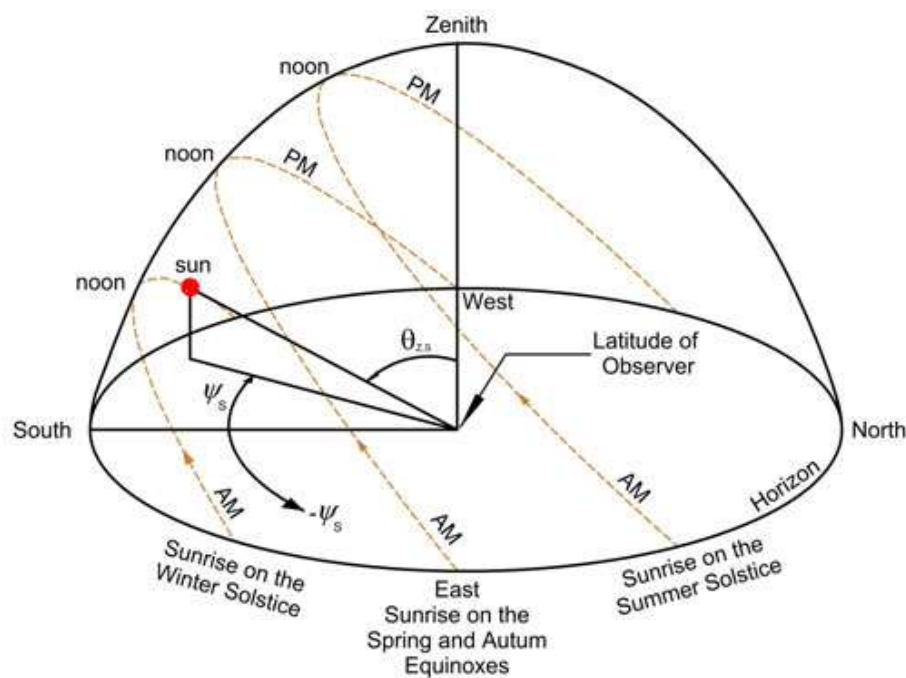
Figure 5.2 Daily sun positions of the four seasons

As shown in Figure 5.2, in spring and autumn the sun rises from east and sets at west making some angle the zenith (vertical to sky) towards the south. Thus for the case of the girder under study where the longitudinal axis lies on the E-W direction, the solar radiation should be almost symmetrical on the southern and northern web faces during the early morning hours and the hours before sunset. While during the mid-

day hours, the northern faces should be partially shaded and hence receive lower amount of solar radiation than the southern faces.

Sun movement during summer is more interesting. As shown in Figure 5.2, the sun rises from the Northern-East and moving towards the Southern-west trying to reach the zenith higher in the sky than in spring or autumn. Before noon the sun crosses the zenith-EW plane resting at the higher point in the sky at the day noon making an angle with the zenith toward the south. Beyond noon, this movement is reversed until the sunset at the N-W direction. Figure 5.3shows this movement on June 21st.
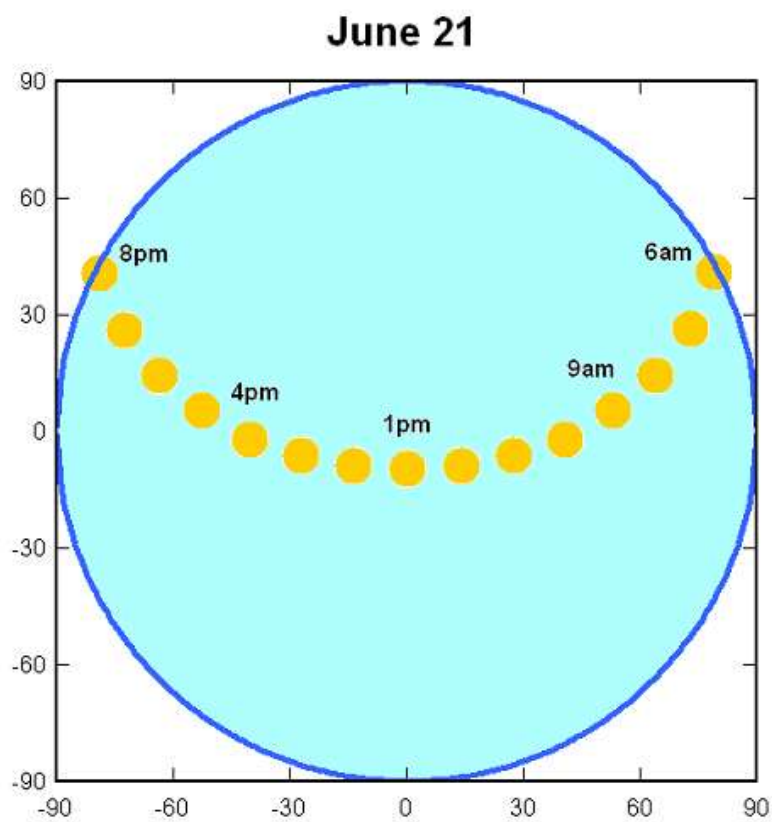
Figure 5.3 Hourly sun positions on June 21st

To validate the solar model used by COMSOL 4.3a, the solar radiation and shading effect were studied at different hours on June 1st and November 15th. Figure 5.4 shows the cross-sectional temperature contour at sunrise at 5.28 am on June 1st. It is shown in the figure that temperature is almost symmetric, which an expected result after the night is cooling hours. However, it is actually not so. There is a slight difference, which can obviously noticed by comparing the 3D temperature contour plots of the northern and southern faces of the girder segment as shown in Figure 5.5.
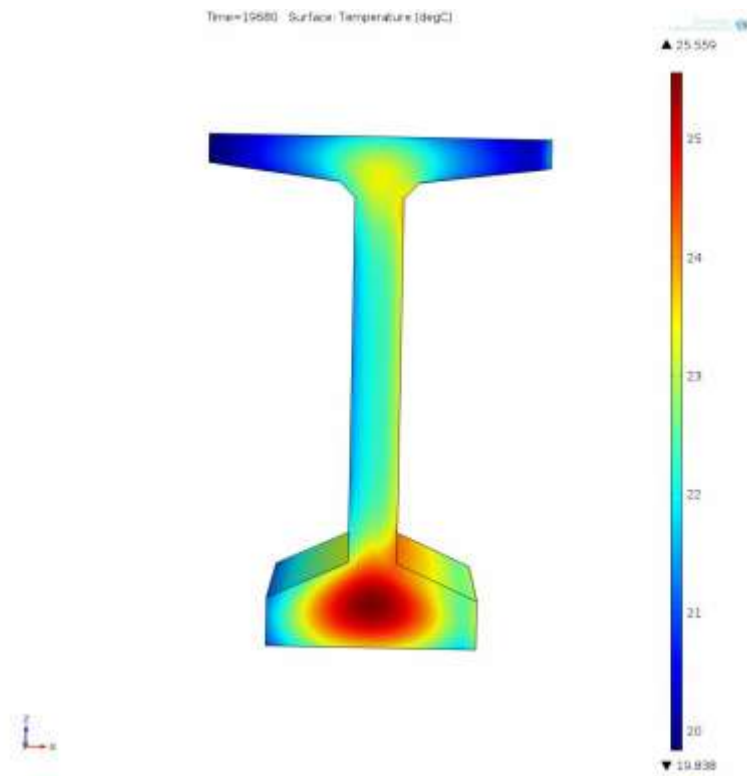
Figure 5.4 Cross-sectional temperature contour at sunrise at 5:28 am on June 1st

5:28 AM Southern Face   *5:28 AM Northern Face*
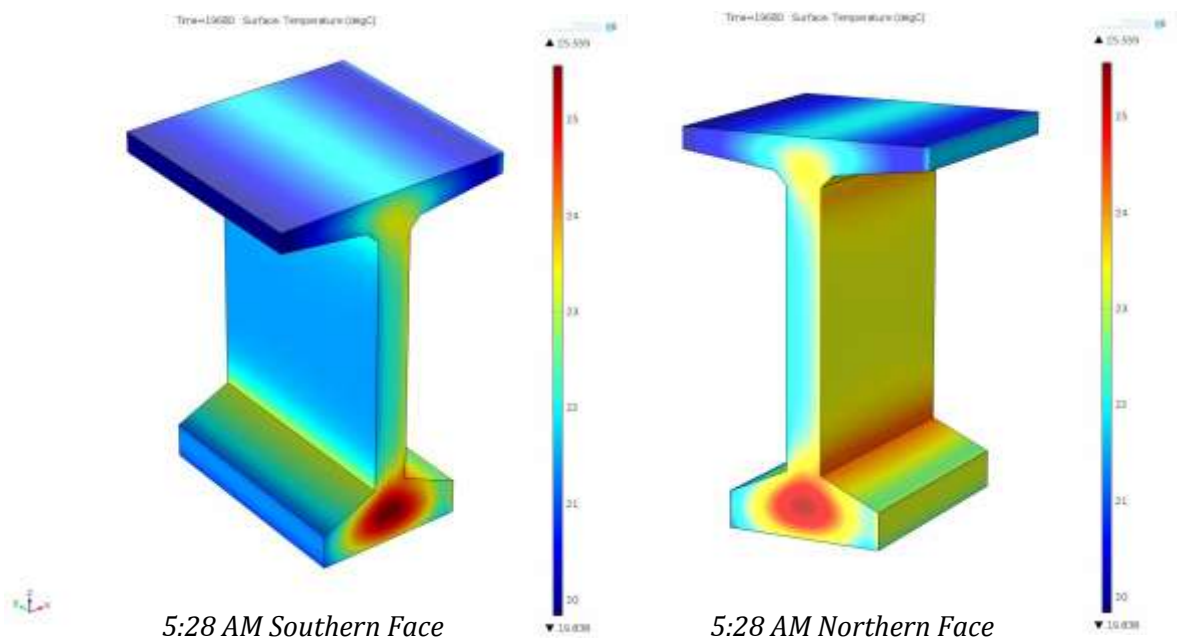
Figure 5.5 Temperature contours at sunrise at 5:28 am on June 1st

As shown in Figure 5.5 solar radiation attacks the northern faces while the southern faces are completely shaded. This means that sun rises from the northern-east

direction. Figures 5.6 and 5.7 show the temperature contours at the sunset time at 7.43 pm on June 1st.
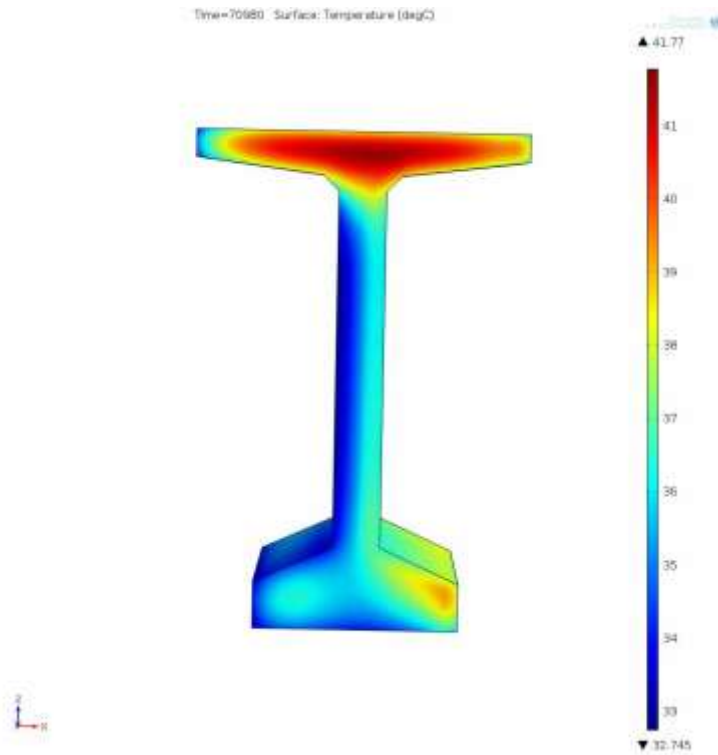
Figure 5.6 Cross-sectional temperature contour at sunset at 7:43 pm on June 1st

7:43 pm Southern Face   *7:43 PM Northern Face*
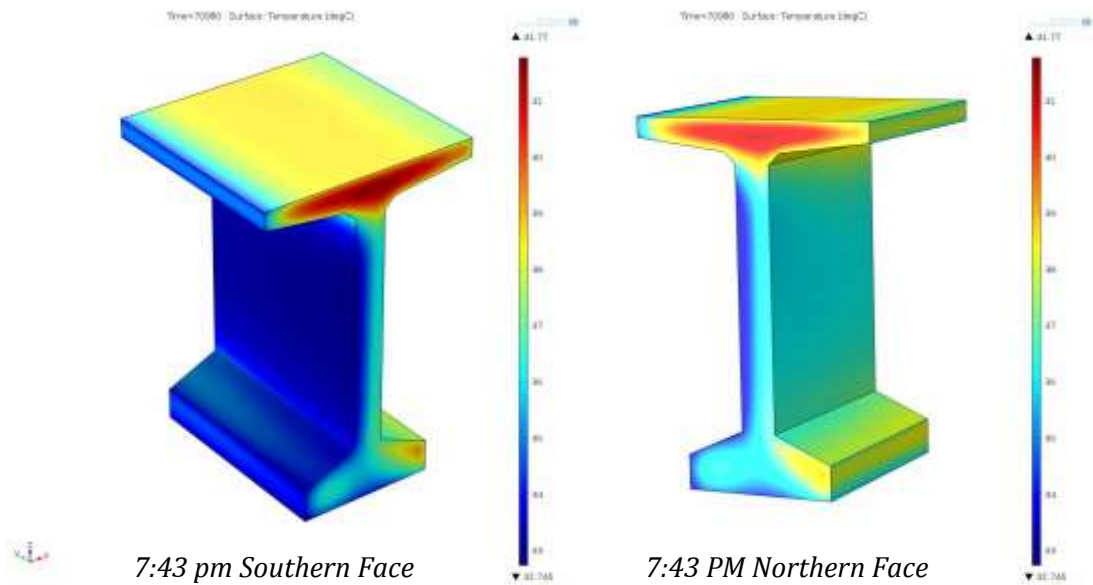
Figure 5.7 Temperature contours at sunset at 7:43 pm on June 1st

The same point can be noticed by the observation of Figures 5.6 and 5.7, where the

northern faces are exposed to solar radiation while the southern faces are shaded and being cooled. This again confirms that in the solar model, the sunsets at some angle to the north rather that the exact west. This comparison still needs the temperature contours at some time near the mid-day. The time of maximum temperature distribution, which is more than two hours after the solar noon on June 1st, is used here. At 2:45 pm the section was noticed to be suffered the maximum daily temperatures, which will be discussed later in this chapter. At this time it is expected that sun has moved from its noon position, which slightly crosses the zenith-EW plane to the south direction towards the sunset position at the northern west. Hence, trying to cross the zenith-EW plane back, which means that solar radiation, is almost symmetrical on both northern and southern faces of the girder as shown in Figure 5.8.
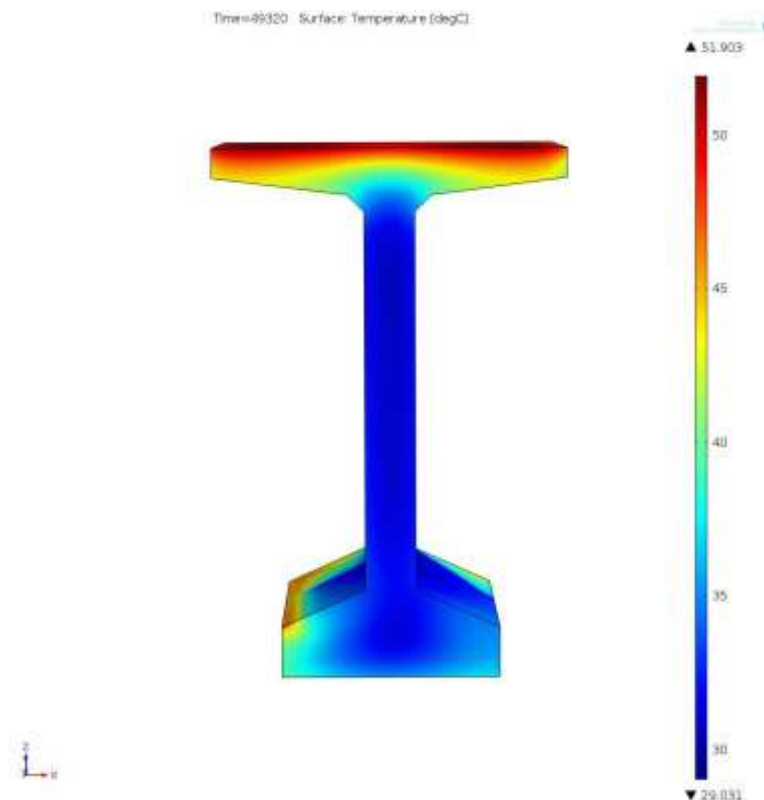
Figure 5.8 Cross-sectional temperature contour at 2:45 pm on June 1st

It is shown in Figure 5.8 and well clarified in Figure 5.9 that the northern faces of the girder segment is slightly further shaded than the southern faces. This mean that at this time the sun hasn't reached the zenith-EW plane yet, and hence the sunrays still slightly tilted to the south direction. Thus, it can be concluded that the solar model of

39

COMSOL 4.3a simulates the actual solar movements.

2:45PM Southern Face   *2:45PM Northern Face*
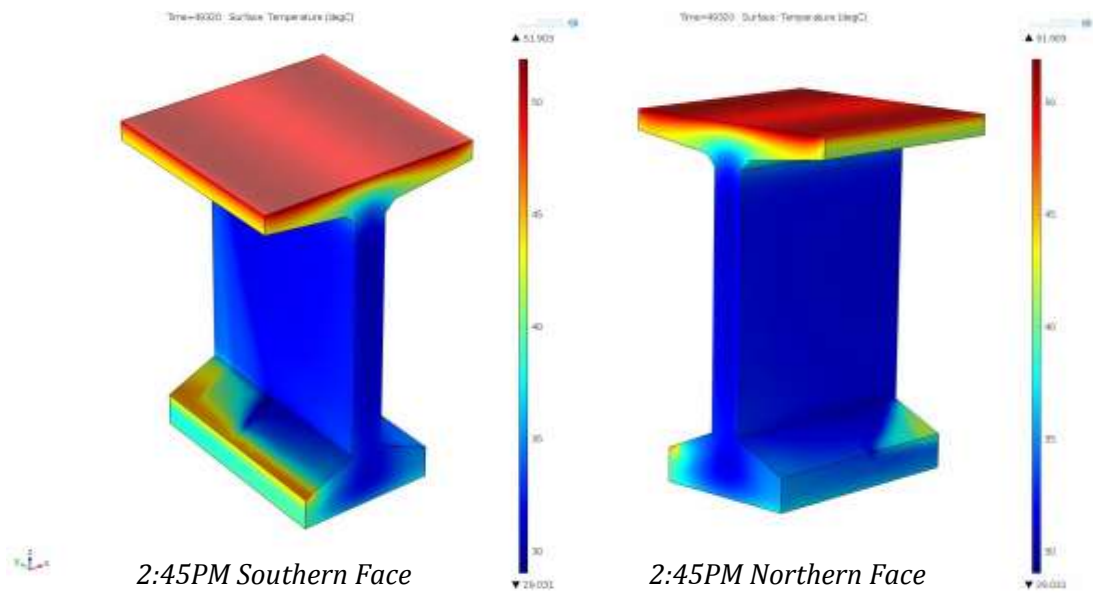
Figure 5.9 Temperature contours at sunset at 2:45 pm on June 1st
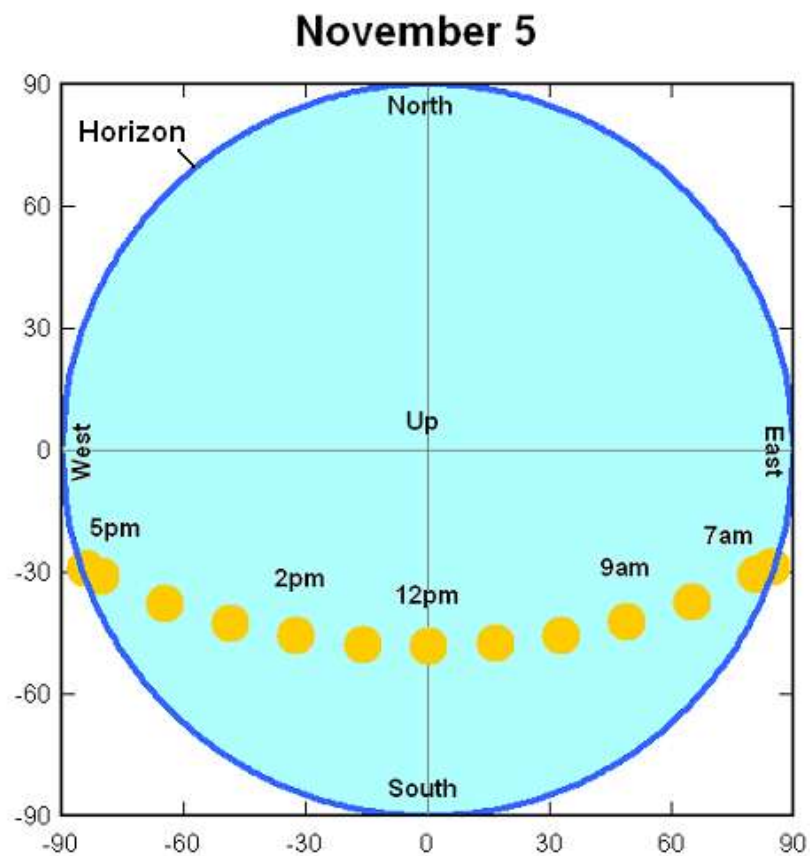
Figure 5.10 Hourly sun positions on November 5th

Another verification of the COMSOL 4.3a solar model can be shown using the same girder segment on November 15th. As shown in Figure 5.2, during November the sun rises from the southern east and sets at the southern west. Between sunset and sunrise, the sun moves to the south of the zenith-EW plane with lower altitude than in summer. This movement is well illustrated in Figure 5.10, which shows the hourly position of sun on November 5th.

This movement is accurately modeled by COMSOL 4.3a solar model as can be obviously noticed in Figures 5.11 through 5.14. The cross-sectional temperature contour at the sunrise time at 7:35 am may give some information about the sun position at that time. However, the 3D temperature contours shown in Figure 5.11 can obviously show that sun rises from the southern east part. As shown, the southern side is fully radiated, while the northern side is still shaded. The Figure 5.11 also reflects that sun is at the lowest daily altitude, since there is no noticeable shading effect on any of the vertical southern faces of the girder and no noticeable radiation effect on the top surface of the girder.

7:35 AM Southern Face   *7:35 AM Northern Face*
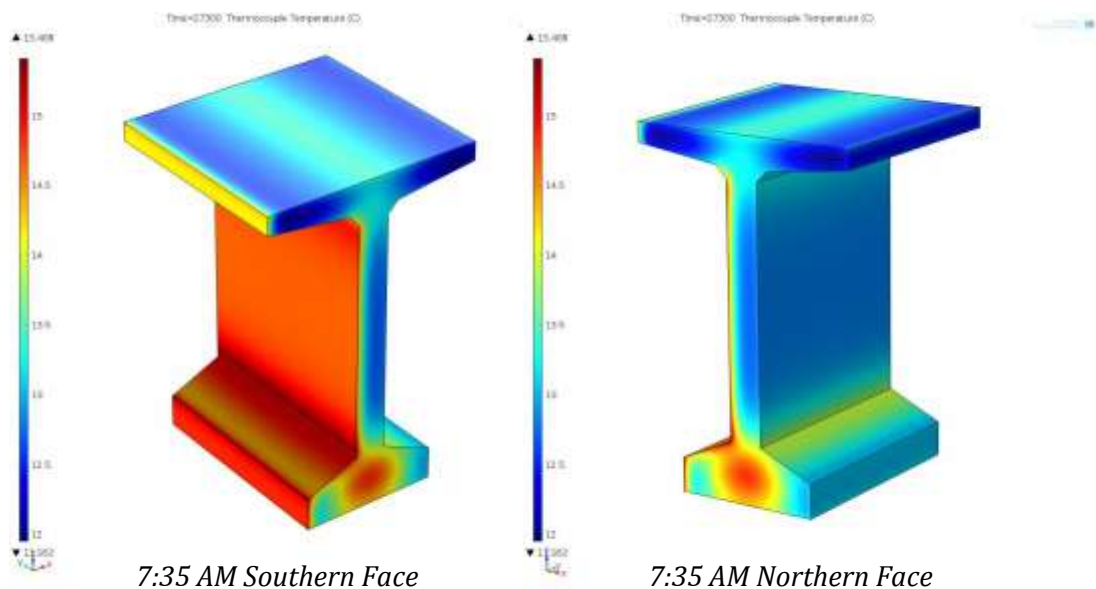
Figure 5.11 Temperature contours at sunrise at 7:35 am on November 15th

Figure 5.12 is a 2D temperature contour which represent the temperature variation on the cross-section of the girder. However, the solar position at the sunset time at 5:34 pm on November 15th is clearly clirified in this figure. The inclination of the sun

41

towards the south at sunset time is clear in Figure 5.12, and it is more obviously shown in Figure 5.13 where 3D temperature contours are illustrated. As shown in Figure 5.13, one important difference between sunset and sunrise times is the temperatures distribution of the top surface of the girder.

In Figure 5.11 the end of the cooling process can be noticed, where the central line of the surface still wormer than the outer areas. This is because the outer areas or the overhanging portions of the girder cooled faster during the night due the larger cooling surface area-to-mass ratio. While, the central area have small cooling surface area compared to the larger beneath concrete mass. The opposite is obviously noticed at the sunset time after the day worming hours. As shown in Figure 5.13, the outer overhanging portions of the flange are wormer than the central area. This is again because of the higher surface area-to-mass ratio compared with the central area. These areas receive higher amounts of solar radiation and hence worm faster.
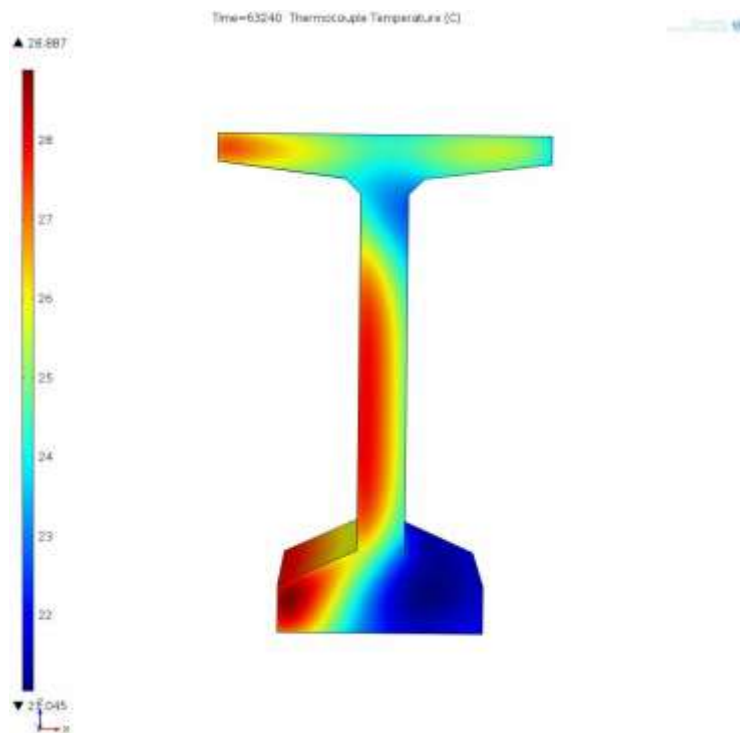
Figure 5.12 Cross-sectional temperature contour at sunset at 5:34 pm on November 15th

5:34 PM Southern Face　　　　*5:34 PM Northern Face*
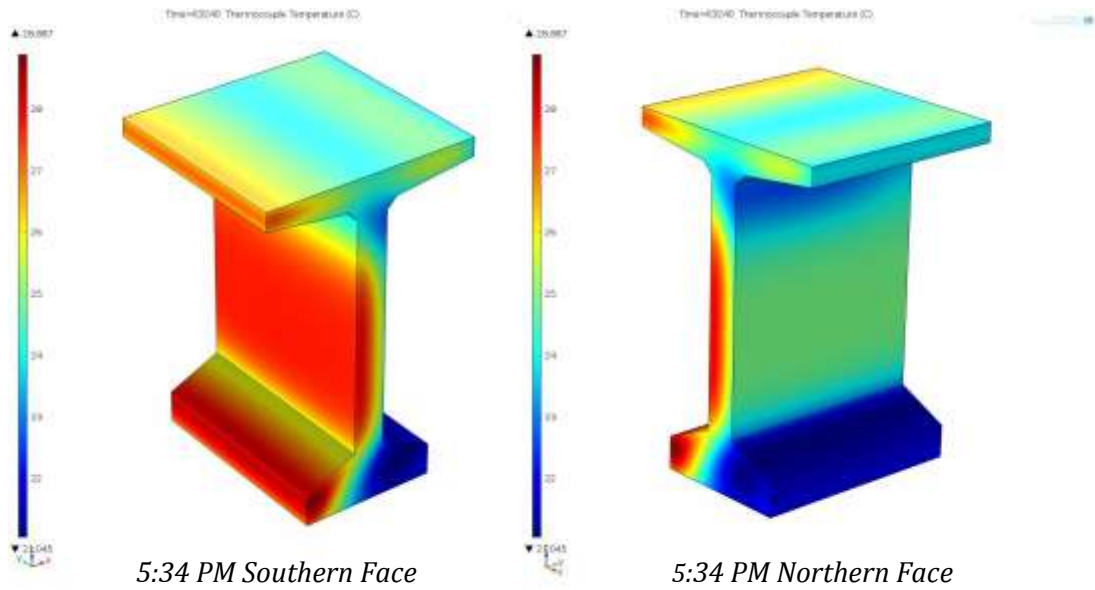
Figure 5.13 Temperature contours at sunset at 5:34 pm on November 15th

1:35 PM Southern Face　　　　*1:35 PM Northern Face*
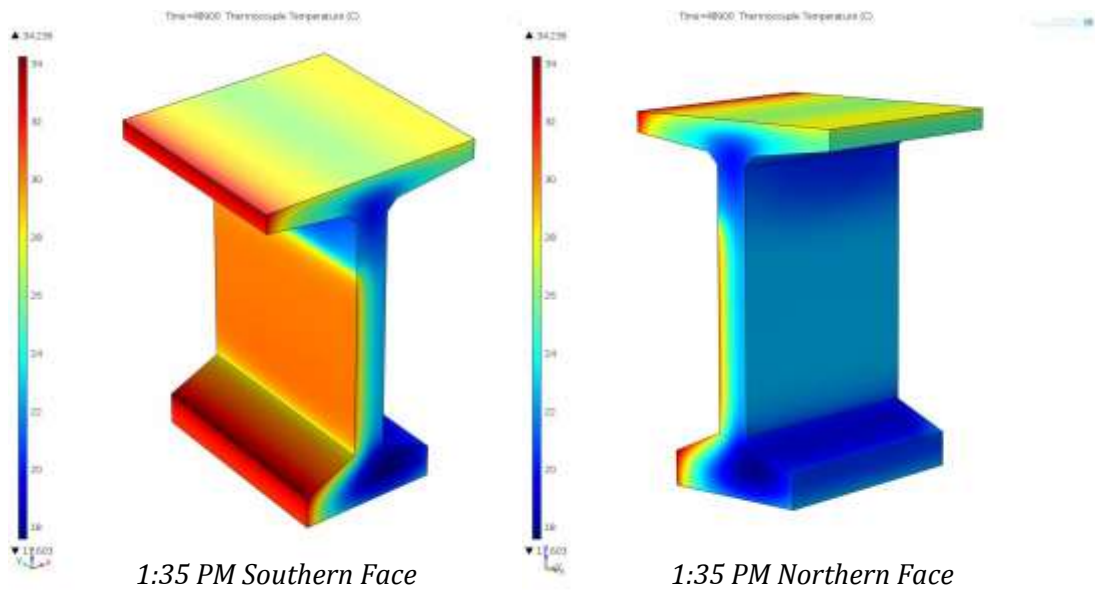
Figure 5.14 Temperature contours at 1:35 pm on November 15th

Figure 5.14 shows the 3D temperature contour plots after the midday of November 15th at 1:35 pm. It is shown that even at the midday period, the sun movement still to the south of the zenith-EW plane. It is clearly shown in the figure that the sun still radiates the southern faces of the girder but with higher altitude, where the top surface receives higher solar incidents and web vertical face is partially shaded by the overhanging portion of the top flange. On the other hand, the northern faces of

the girder are almost fully shaded due to the sun inclination angle. The previous figures together with those of June 1st show the high accuracy of the COMSOL solar model.

5.3 Element Type and Load Procedure

In COMSOL choosing element type is not required like in ANSYS, it is only required to define the type of the shape function whether Lagrange element or Hermitian element. Also, the order of the shape function should be defined whether linear, quadratic, cubic, quartic or quintic.

Since radiation is a nonlinear problem, then nonlinear element should be used. For heat transfer with radiation, the default element order is quadratic. In COMSOL, loads can be applied directly, using interpolation tables, or using various types of functions. The daily changes in temperature and wind speeds were introduced as a tabular data, COMSOL then transform these tabular data into an interpolated function. The user can control the type and order of this interpolation whether linear or higher order. Daily temperature was interpolated as a sin wave, while wind speed was introduced as stepped linear interpolation to simulate the daily temperature and wind speed defined in Figures 3.3 and 3.4 respectively.

The heat transfer with surface-to-surface radiation module was used to define the heat transfer process with many possible load types. Convection coefficient was introduced as a function of the hourly-interpolated wind speed. Surface-to-ambient radiation was activated, so that the grandiosity of all surfaces is calculated directly at each time sub-step based on the difference between the introduced ambient air temperature and the calculated surface temperature from the previous time sub-step. Surface-to-surface radiation between the girder surfaces is automatically activated in this module. It is the most complicated and time consumer item of the heat transfer model.

Solar radiation was defined using the COMSOL solar model as an external radiation source. Reflected radiation from ground was also calculated as an external time-dependent heat flux using a ground reflectivity of 0.2. Note that some of the introduced thermal loads like surface-to-surface radiation and ground reflectivity

were not introduced in the ABAQUS model of the author. The surface-to-surface radiation, which combined with surface-to-ambient radiation in open enclosures is the most complicated item in the heat transfer process and is generally neglected by most of the previous researchers due to this complicity.

5.4 Results of the COMSOL Model

In this section, temperature results of the current COMSOL model are discussed and compared with the measured and ABAQUS model predicted results discussed in chapter 4. These results include the temperature contours at specific times of the day and the daily temperature variation at specific thermocouple locations both at the first of June and the fifteenth of November.

5.4.1 Temperature contours

Figures 5.15 through 5.18 show the comparison temperature contours on June 1st, while Figures 5.19 and 5.20 show these temperature contours on November 15th.

5.4.1.1 Temperature contours on June 1st

In Figure 5.15 and 5.16, the effect of sun position in the summer mornings is clear, where northern faces are under direct low altitude solar radiation and southern faces are almost completely shaded.
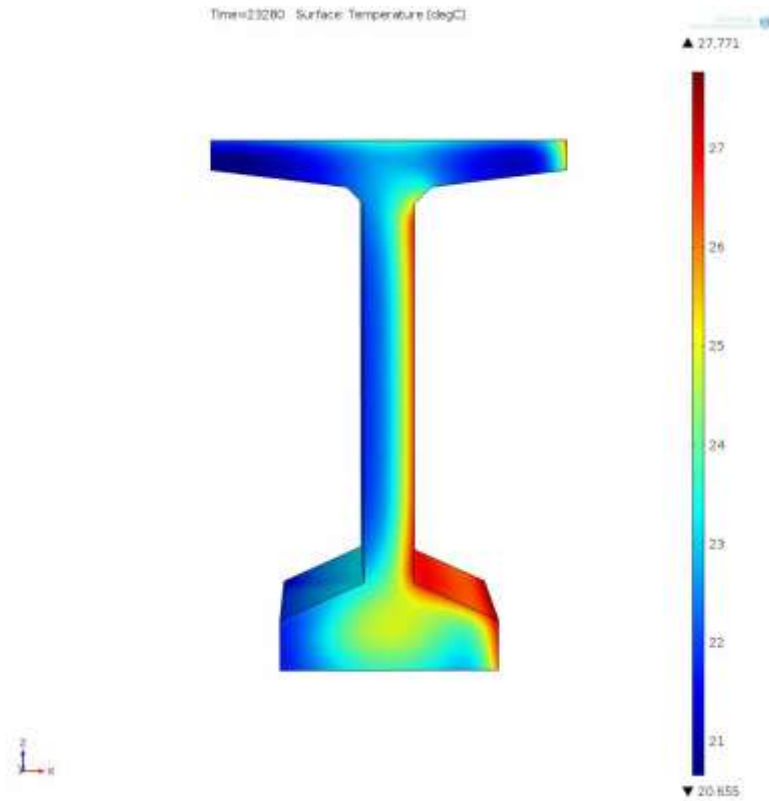
Figure 5.15 Cross-sectional temperature contour at 6:28 am on June 1st

6:28 AM Southern Face   *6:28 AM Northern Face*
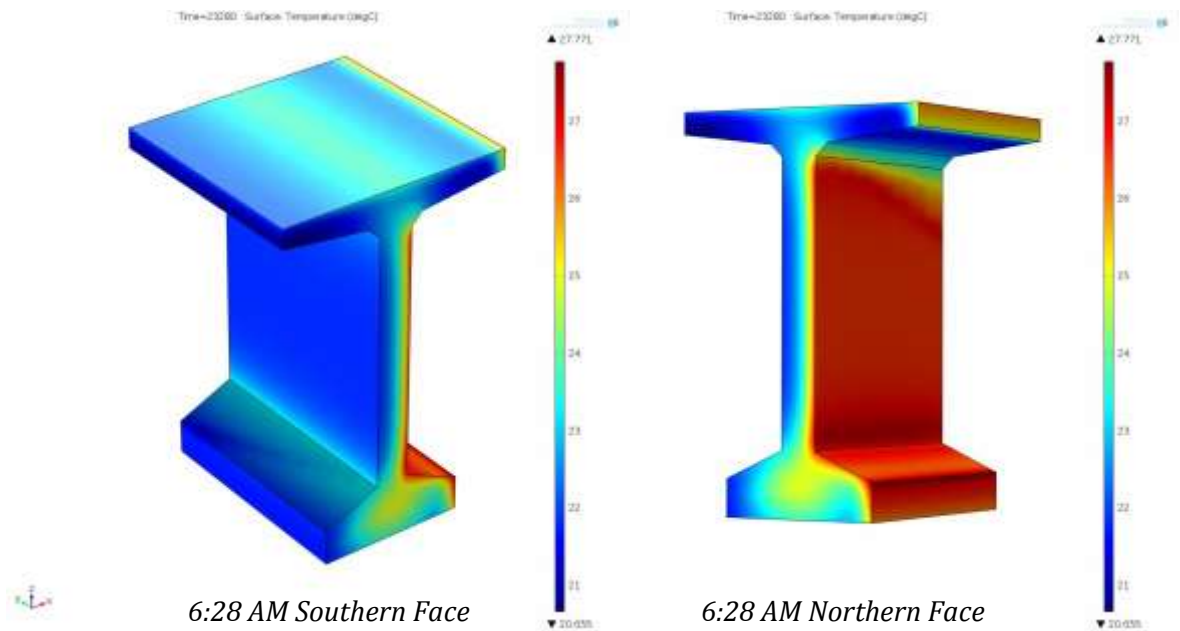
Figure 5.16 Temperature contours at 6:28 am on June 1st

As shown in Figure 5.15 and 5.16, the girder temperature ranges from 20.6 ℃ to 27.7 ℃ at the early morning at 6:28 am, which are almost the exact measured thermocouple temperatures, the measured thermocouple temperatures at 6:28 am are

in the range of 20.6 °C to 27.1°C. The temperature distribution is also the same with minor differences, where the maximum temperature located at the center of the bottom flange while the bottom faces of the far ends of the top flange seems to have the minimum temperatures.

One important difference between COMSOL temperature contour shown in Figure 5.15 and the compared ABAQUS temperature contour shown in Figure 3.12a is the effect of the sun position, where it is shown that temperature is almost symmetric in Figure 3.12a. This can be attributed again to the output format of these contours. Because the author used only one color for each 5°C difference, while in COMSOL output formatting, the full range of rainbow color grading was used. Using wider range of colors to present smaller temperature steps make it betters to accurately study the temperature distributions. However, this does not mean that the used solar model by the author is incorrect. By the comparison between Figure 3.12b for temperature contours at 1:42 pm and its corresponding COMSOL figures, Figure 5.17 and 5.18, it is shown in all these figures that sunrays are slightly inclined toward the southern faces as discussed in the previous section.
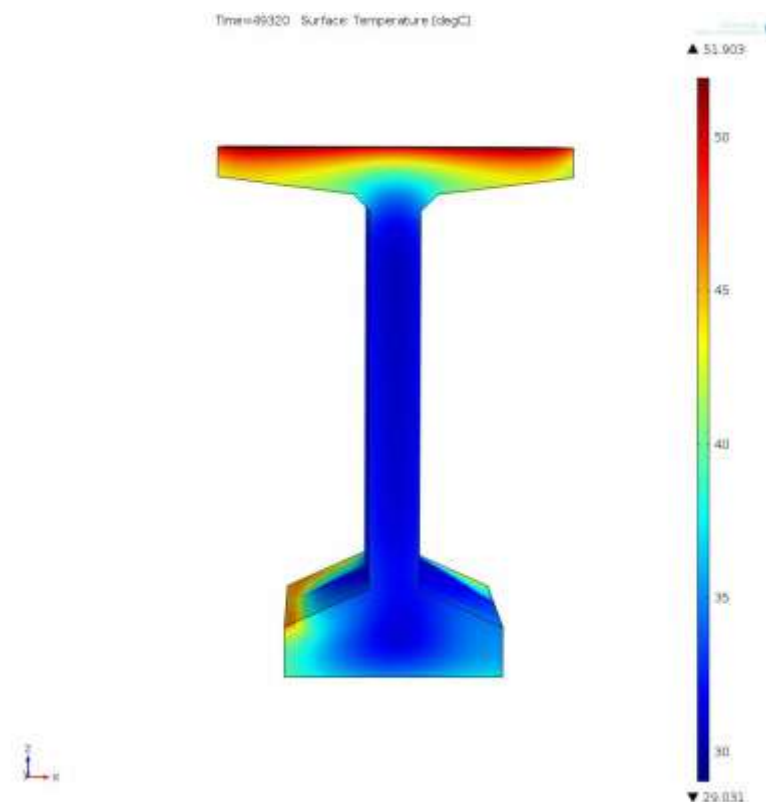
Figure 5.17 Cross-sectional temperature contour at 1:42 pm on June 1st

1:42 PM Southern Face   *1:42 PM Northern Face*
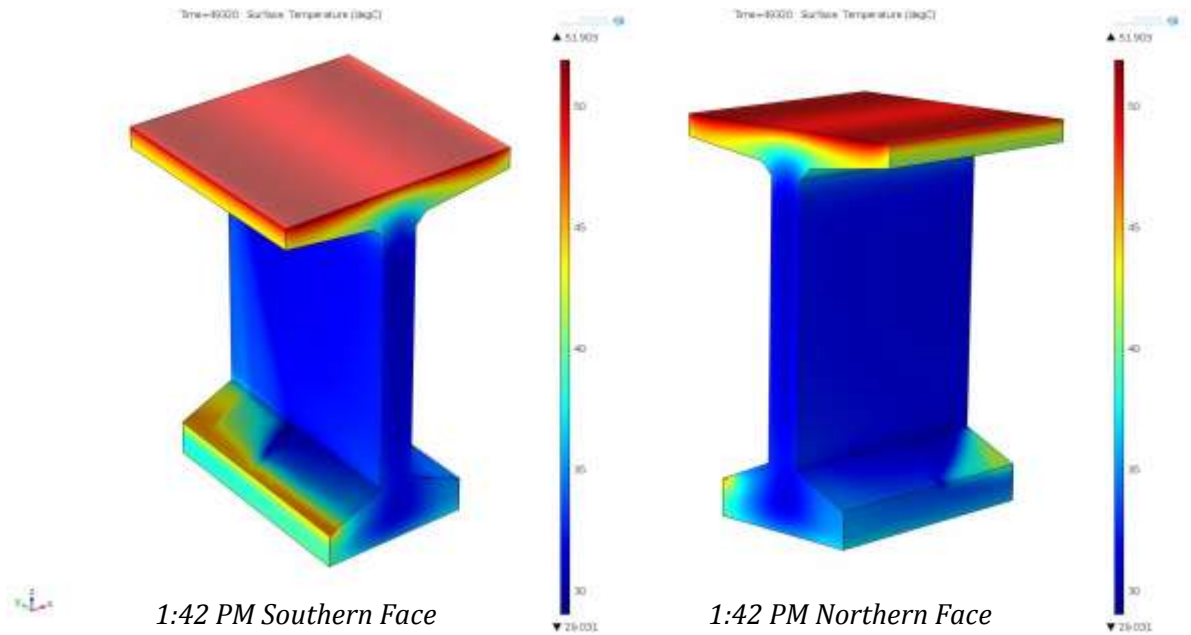
Figure 5.18 Temperature contours at 1:42 pm on June 1st

This can be noticed by the comparison of the two ends of the top faces of the bottom flange. This means that the solar modeling used by the author follows the correct solar movement. The thermocouple-measured temperatures were in the range of 30.6 ℃ to 50.9 ℃, while the range of the predicted temperatures by COMSOL model is 29 ℃ to 51.9 ℃, which reflects the accuracy of the COMSOL predicted temperatures where temperature difference does not exceed 1.6 ℃. On the other hand, the ABAQUS predicted temperatures were from 29.7 ℃ to 49.3 ℃ which is also close enough to the measured temperatures with a maximum temperature difference of 1.6℃.

The COMSOL model temperature distribution is quite similar to that of ABAQUS. As shown by the comparison between 5.17 and 3.12 b, the maximum temperatures concentrated on the top layers of the top flange composing some condensed slightly varied temperature layers with smaller depths at the central area and larger depths at the outer areas of the top flange, while the web temperature seems to be uniform near the minimum girder temperature, which concentrated at the central mass of the bottom flange.

5.4.1.2 Temperature Contours on November 15th

Comparing the temperature contours on November 15th, it can be said that the same notices and observations discussed in the comparison of June 1st both for morning and afternoon can be drawn here. Taking into account the output controls and the color grading-temperature ratio used in the current COMSOL model and the author ABAQUS model, it can be said that both models drawn almost the same temperature contours at 7:35 am and 1:35 pm. This can be obviously shown by the comparison of Figures 5.19 with Figure 3.13a.

The minimum and maximum thermocouple temperatures recorded by the author were about 9 ℃ and 14.2 ℃ respectively. While COMSOL model shown in Figure 5.19 shows that temperature ranges from about 11.9 ℃ to about 15.4 ℃ at 7:35 am. Thus a maximum temperature difference of about 2.9 ℃ is recorded between the measured and COMSOL predicted temperature at this time. While a maximum daily temperature difference of 5.4 ℃ was recorded between the measured and the compared ABAQUS predicted temperatures on November 15th. At 1:35 pm, the current COMSOL model and the compared ABAQUS model show exactly the same behavior and temperature contour plots.
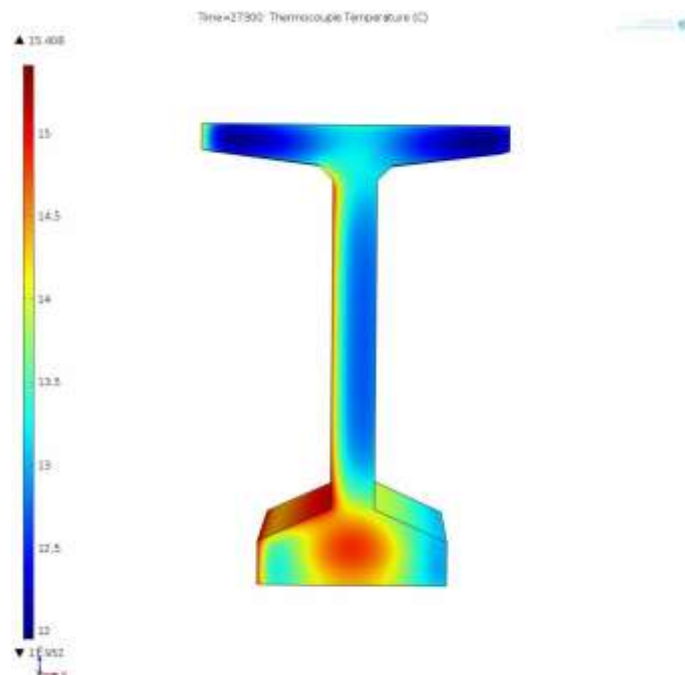
Figure 5.19 Cross-sectional temperature contour at 7:35 am on November 15th

Comparing the temperature contour at 1:35 pm shown in Figure 5.20 and Figure 3.13b, it can be obviously noticed that both are almost identical. In both figures, the maximum temperature concentrated on the southern vertical faces of the top flange, web and bottom flange in addition to the upward tilted surface of the bottom flange. The upper part of the southern face of the web is clearly shown to be shaded by the overhanging portions of the top flange and hence have lower temperatures than the lower points of the same surface that are directly exposed to sunrays. On the other hand, lower temperatures are graded towards the fully shaded northern surfaces of the web and the bottom flange. The top shaded mass of the web and the northern shaded mass of the bottom flange has the minimum temperature grading with absolute minimum temperature at the center of the northern part of the bottom flange.
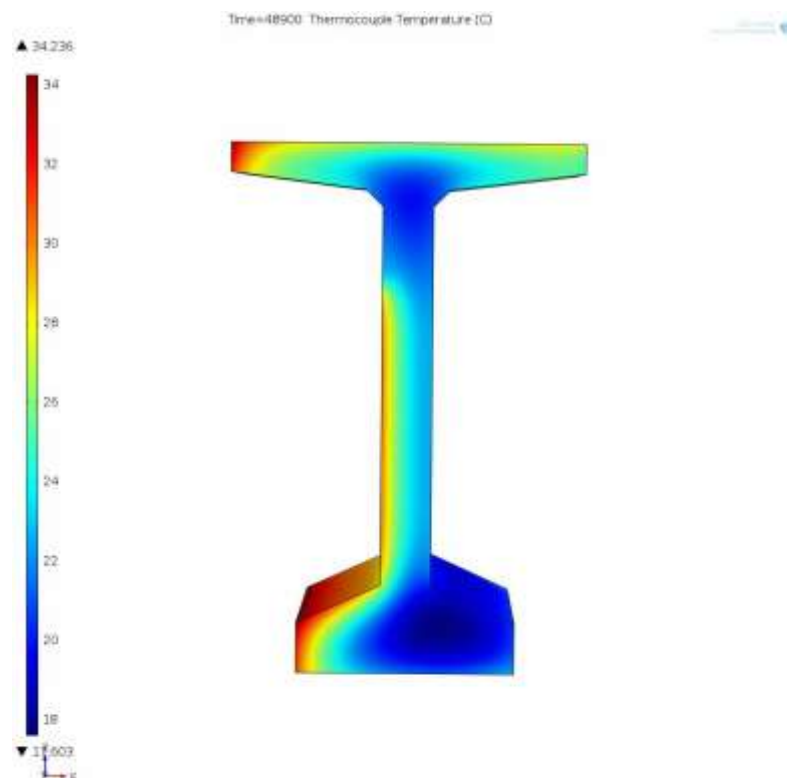
Figure 5.20 Cross-sectional temperature contour at 1:35 pm on November 15th

The minimum and maximum COMSOL predicted temperatures at 1:35 pm are 17.6 ℃ and 34.2 ℃ respectively as shown in Figure 5.19. While the measured thermocouple minimum and maximum temperatures are 14.9 ℃ and 35.3 ℃ respectively. Thus, the maximum temperature difference between the measured and

COMSOL predicted a temperature at this time is about 2.7 ℃. This difference is about half the maximum daily temperature difference recorded between the measured and ABAQUS predicted temperatures on November 15th, which is 5.4 ℃.

5.4.2 Temperature variations at thermocouple locations

In this section the daily temperature variations at specific thermocouple locations both on June 1st and November 15th are discussed. These variations are compared with those measured directly from the experimental girder segment and with the corresponding variations predicted by the compared ABAQUS model.

5.4.2.1 Temperature variations on June 1st

Figures 5.21 through 5.23 show the daily temperature variations at specific thermocouple locations during the full 24 hours of the first of June. The comparison of these temperature variations with the corresponding measured and ABAQUS predicted variations shown in Figures 3.6 through 3.8 reveals the good agreement of both the behavior and temperature values of these variations with the measured and the ABAQUS model variations. Figure 5.21 show the temperature variations at the location of thermocouples 7, 13 and 28. The comparison of this figure with Figure 3.6 shows that the behavior is almost the same for the three thermocouples. Also, the maximum and minimum temperature values fairly agree with those of the compared ABAQUS model results and the measured temperatures.
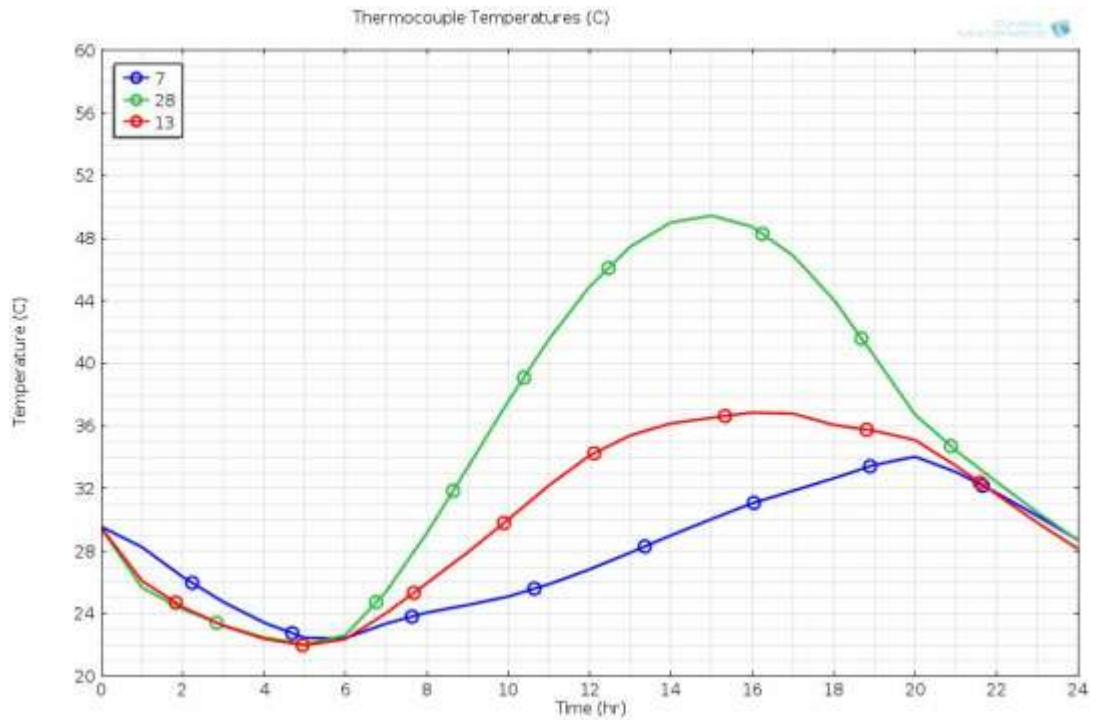
Figure 5.21 Temperature variations at thermocouples 7, 13, 28 on June 1st

The same fashion of agreement is recorded for thermocouples 2 and 5, as obviously shown in Figure 5.22 and 3.7. Comparison between Figure 5.23 and 3.8 at thermocouples 11 and 14, show that COMSOL has well simulated the temperature variation at these thermocouples. One important difference between the COMSOL predicted temperature variation and the compared measured variation at thermocouple is the curve sagging between 11:00 am and 3:00 pm. Similar sagging but with lower slopes can be noticed in Figure 3.8.

This drop of temperature can be attributed to the shading effect on the location of thermocouple 11 at the northern part of the bottom flange as well illustrated in Figure 5.18. This shading occurred due to the crossing of the sun from the north to the south of the zenith-EW plane at about 10:00 am, and back crossing of this plane to the northern side at about 4:00 pm as shown in Figure 5.3. A general notice, which may slightly affect the temperature values, is the initial condition applied in the COMSOL model. The effect of the initial temperature, which assumed to be uniform through the full girder mass at the initial time, can be reduced by starting the simulations three days before the target day. This procedure was followed in the current ANSYS model and the compared ABAQUS model. However, in the COMSOL model and because of the activation of surface-to-surface radiation, the run rime became too

52

long and hence shorter time period, which is only the target 24 hours, was considered.

Figure 5.22 Temperature variations at thermocouples 2 and 5 on June 1st
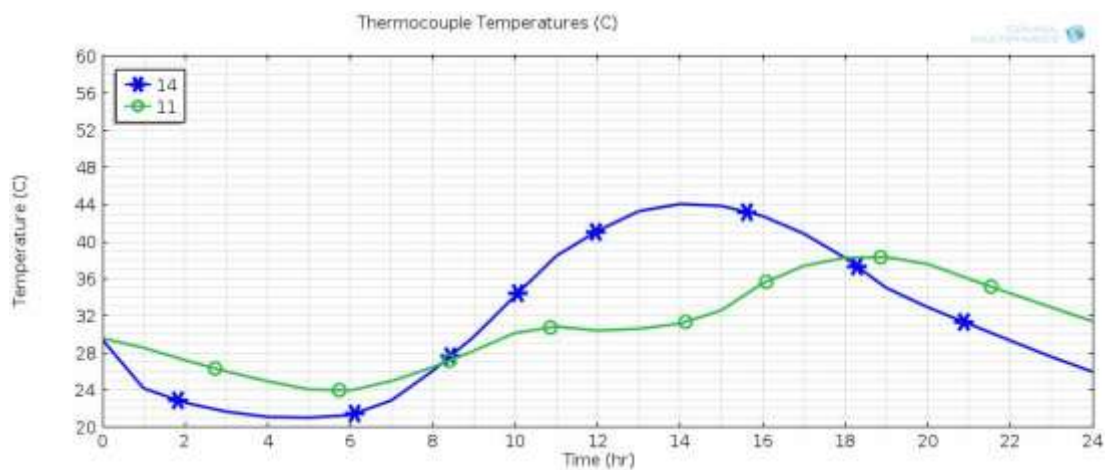
Figure 5.23 Temperature variations at thermocouples 11 and 14 on June 1st

5.4.2.2 Temperature variations on November 15th

Figures 5.24 through 5.26 illustrate the temperature variations during the 24 hours of the 15th of November at different thermocouple locations. The behavior of the temperature variation curves of the thermocouples 7, 13 and 28 follow the same measured behavior. A comparison between Figure 5.24 and 3.9 shows that the domains of concaving up and down, inflection points, curves intersection points and extreme maximum and minimum value are almost the same.
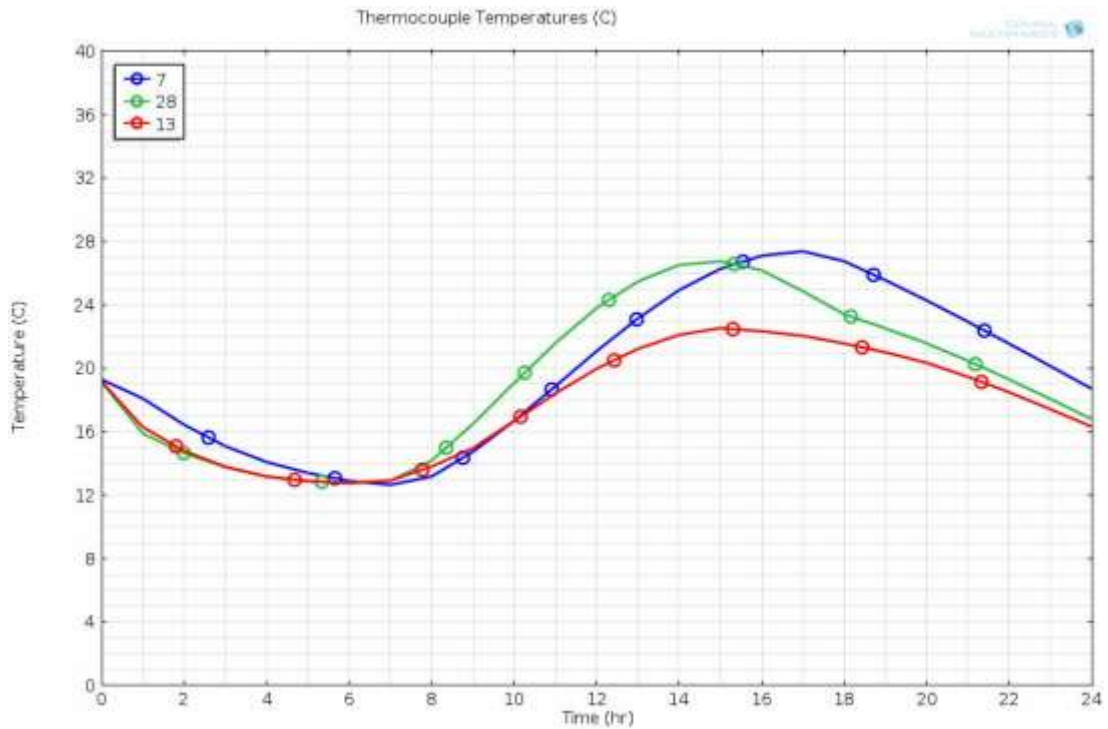
Figure 5.24 Temperature variations at thermocouples 7, 13, 28 on November 15th

Comparison of Figure 5.25 that describes the temperature variation at thermocouples 2 and 5 predicted using the COMSOL model with Figure 3.10, which describes the corresponding measured and ABAQUS predicted temperature variations, shows the high degree of agreement of the COMSOL results with those measured or ABAQUS predicted. Excluding the initial time, which discussed earlier in the previous section, all curves details are almost identical. Thermocouple 11 and 14 show similar fashion of behavior agreement as shown in Figures 5.26 and 3.11.
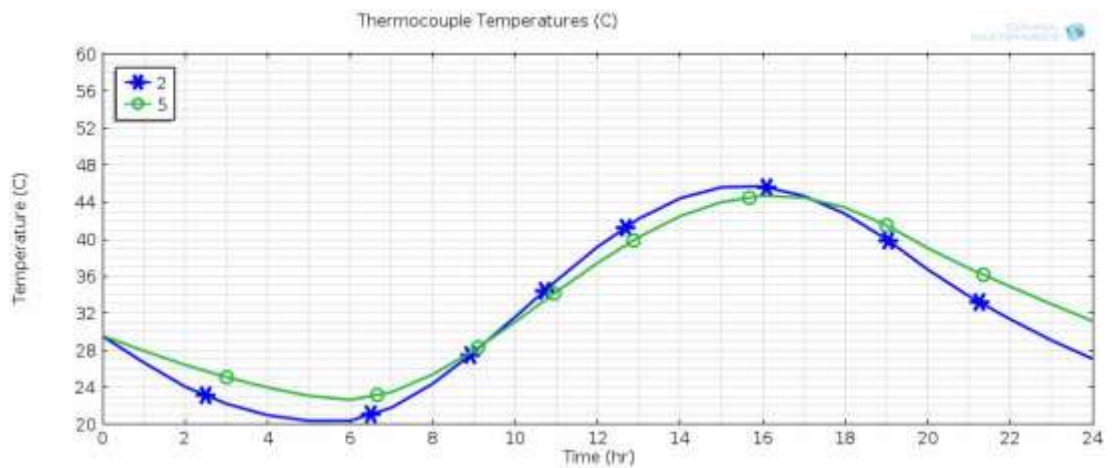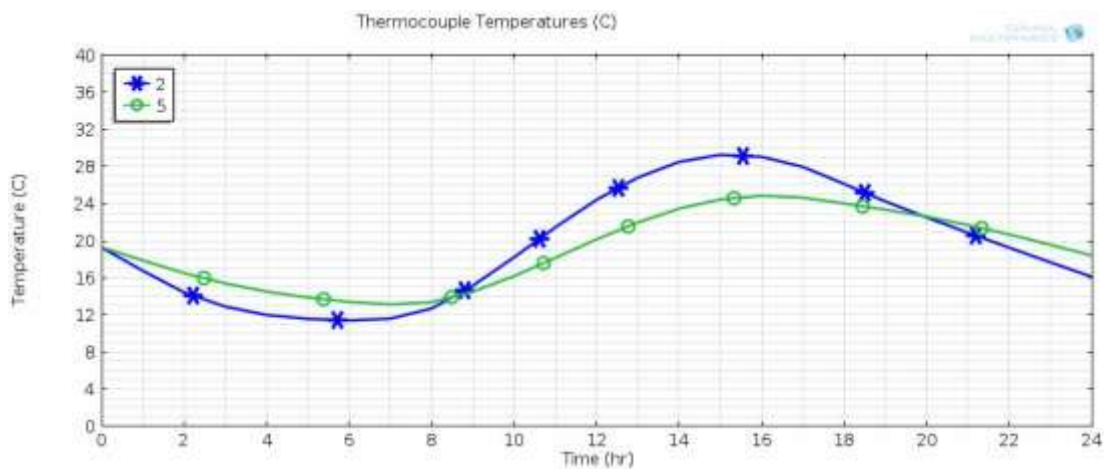

Figure 5.25 Temperature variations at thermocouples 2 and 5 on November 15th
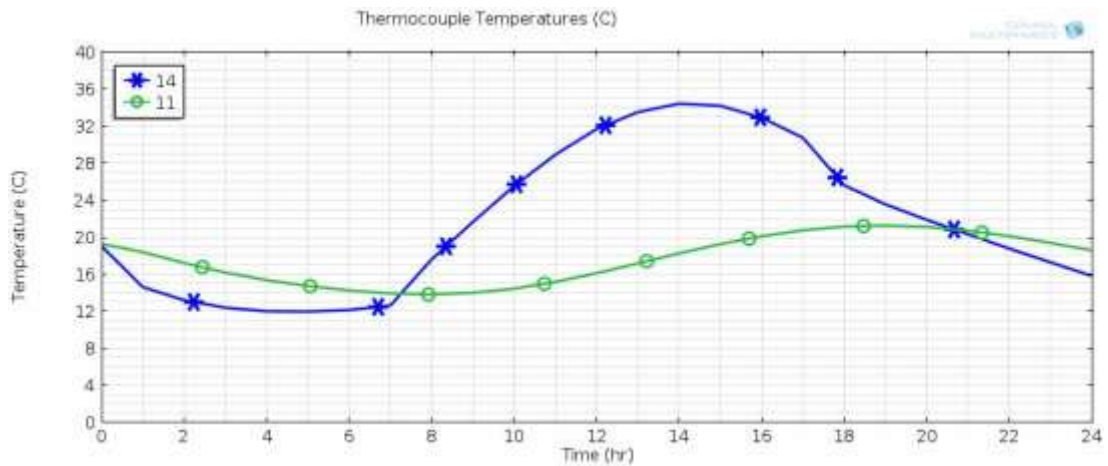
Figure 5.26 Temperature variations at thermocouples 11 and 14 on November 15th

5.5 Vertical Temperature Distributions on June 1st

This part compares vertical temperature differences expected by the heat transfer analysis and obtained from the experiments. The vertical temperature difference of the locations thermocouple at mid-span was installed along the web heights of the girder thermocouples 28, 5, 6, 7, 8, 9, 12 and 13 (A-A line). Depended on the maximum vertical temperature differences, the vertical temperature distributions were evaluated at the thermocouple sites. This study compares the measured and predicted maximum negative and positive vertical temperature distributions along the height of the girder. According to the vertical temperature difference in the girder during on June1[st], the lowest temperature was predicted along of the bottom flange (thermocouple 9) and the highest temperature on the top surface along of the top flange (thermocouple 28). The Average Absolute Error (AAE) and the Maximum Absolute Error (MAE) were used as verification tools. The AAE is the average of the absolute differences between the predicted and the experimental temperatures for a group of thermocouples at a specific time, while MAD is the maximum absolute difference within the group of thermocouples at that time.

In Figure 5.27, the AAE was 0.97^{o}C while the MAE was 2.3^{o}C at (thermocouple 28). This AAE and MAE occurred at 6:30 am. Figure 5.28 shows temperature contours at sunrise at 6:30 am on June 1st. In Figure 5.29, the AAE was 1.2^{o}C and 1.0^{o}C while the MAE was 3.0^{o}C and 2.4^{o}C at (thermocouple 6). This AAE and MAE occurred at 1:40 pm and 2:00 pm respectively. Figure 5.30 and 5.31 illustrated temperature

contours at 1:40 pm and 2:00 pm on June 1st. The predicted temperatures of the FE analysis have good agreement with the experimental temperatures for both the positive and the negative vertical temperature distributions.
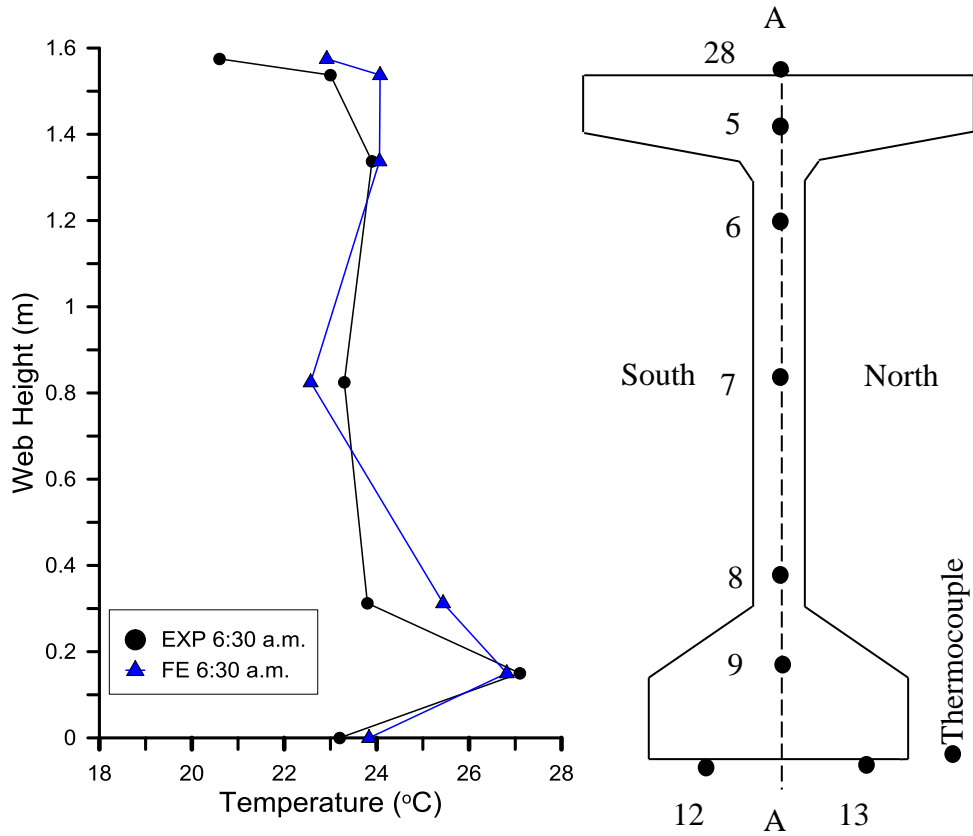
Figure 5.27 Measured and predicted maximum negative vertical temperature distributions along the depth of the girder on June1st
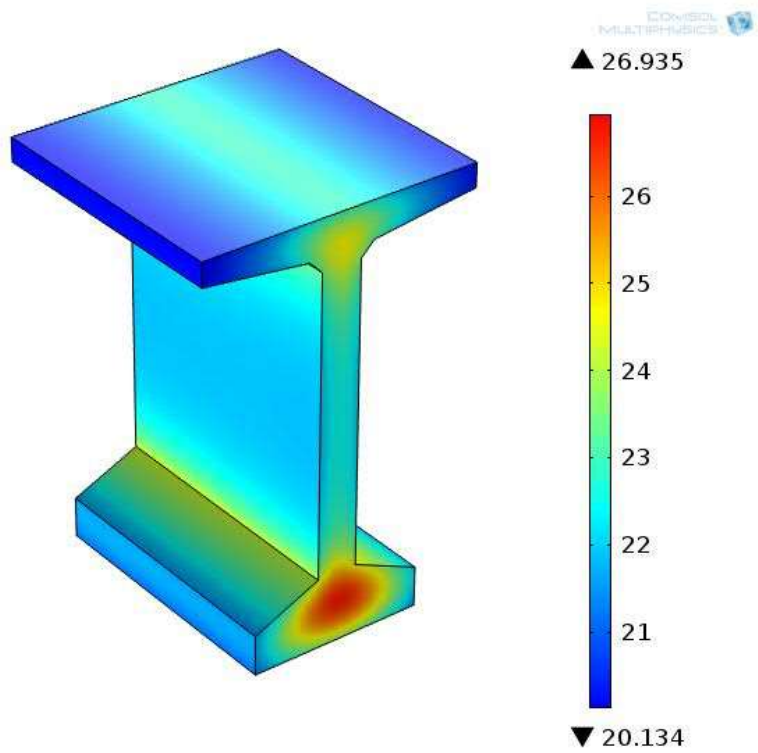
Figure 5.28 Temperature contours at sunrise at 6:30 am on June 1st
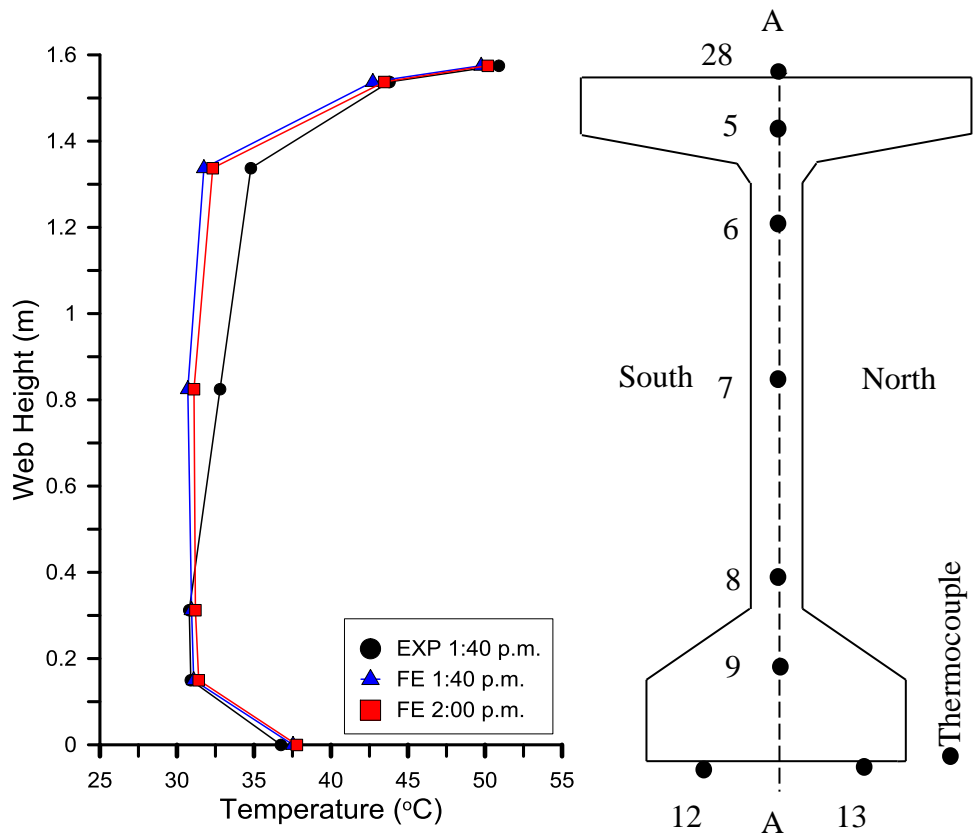
Figure 5.29 Measured and predicted maximum positive vertical temperature distributions along the depth of the girder on June1st
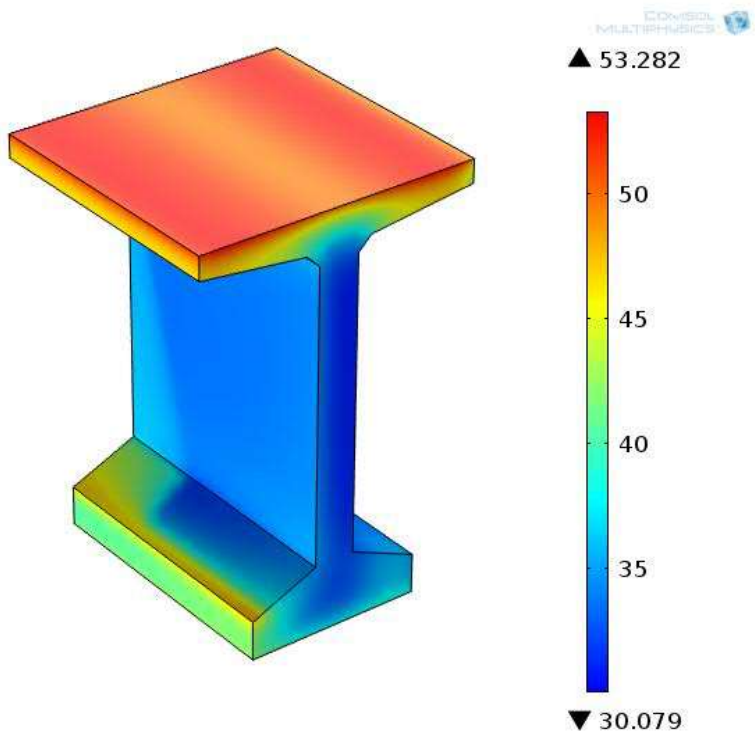
Figure 5.30 Temperature contours at 1:40 pm on June 1st
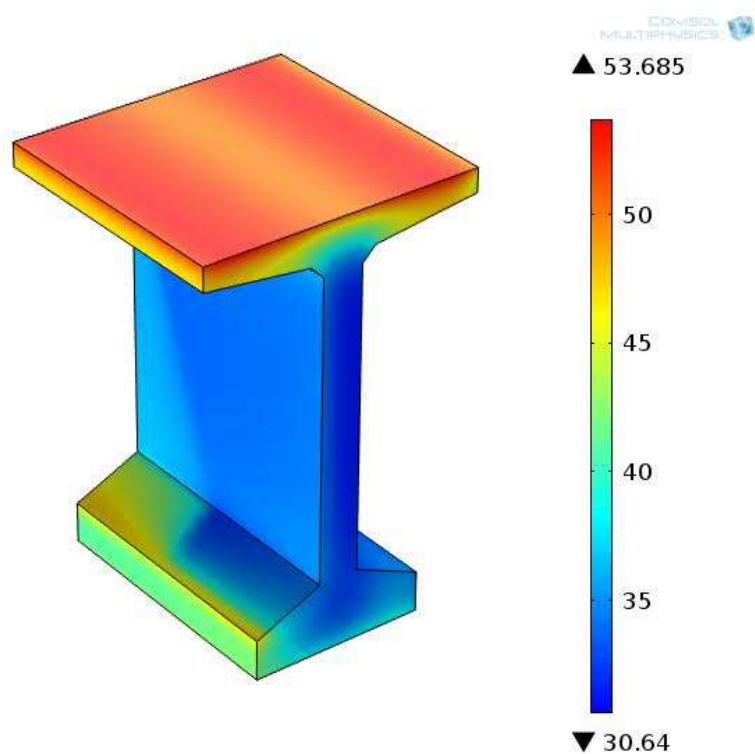
Figure 5.31 Temperature contours at 2:00 pm on June 1st

5.6 Lateral Temperature Distributions on June 1st

Also this section compares maximum lateral temperature differences exposed by the heat transfer analysis and obtained from the experiments. Due to expose the girder to direct intensity of solar radiation from the sun only one side of the girder and the top surface, lead to the largest transverse temperature distribution, the lateral temperature differences were studied along the top flange width thermocouples 2, 4, 5, 3 and 1 (B-B line), along the bottom flange width thermocouples 14, 10, 9, 11 and 15 (D-D line) and across the web thickness thermocouples 20, 7, and 21 (C-C line). Based on the maximum lateral temperature differences, the lateral temperature distributions were evaluated at the thermocouple sites. Figure 5.32 and 5.33 compares the measured and predicted maximum negative and positive lateral temperature distributions along the width of the top flange of the girder. Also the (AAE) and the (MAE) were used as verification tools.

As shown in Figure 5.32 includes temperature difference, defined from the AAE was 1.1^{o}C and 1.0^{o}C while the MAE was 1.75^{o}C and 1.70^{o}C at (thermocouple 4). This AAE and MAE occurred at 6:30 am and 6:40 am respectively. Also Figure 5.34 shows temperature contours at sunrise at 6:40 am on June 1st.

In Figure 5.33, the AAE was 0.40^{o}C while the MAE was 0.80^{o}C at (thermocouple 4). This AAE and MAE occurred at 1:10 pm. Figure 5.35 shows temperature contours at 1:10 pm on June 1st. The highest temperature predicted took place on the south-side of the top flange and the lowest temperature took place in the middle of the top flange. The predicted temperatures of the FE analysis have good agreement with the experimental temperatures for both the positive and the negative lateral temperature distributions

Figure 5.32 Measured and predicted maximum negative lateral temperature distributions along width of the top flange of the girder on June1[st]

Figure 5.33 Measured and predicted maximum positive lateral temperature distributions along width of the top flange of the girder on June1[st]

Figure 5.34 Temperature contours at sunrise at 6:40 am on June 1st
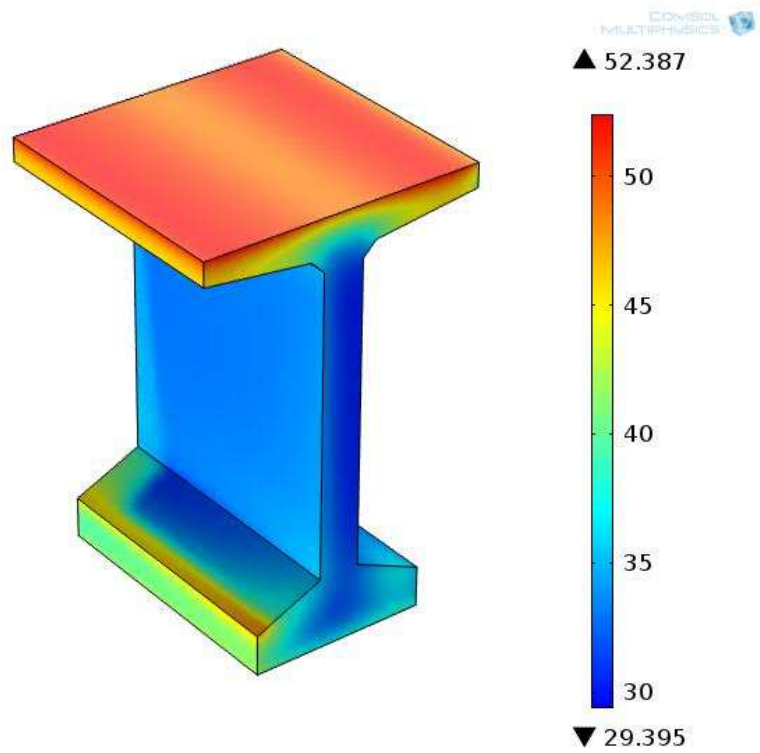
Figure 5.35 Temperature contours at 1:10 pm on June 1st

Figure 5.36 and 5.37 compares the measured and predicted maximum negative and positive lateral temperature distributions along the width of the bottom flange of the girder on June 1st. As shown in Figure 5.36, the AAE was 0.29^oC while the MAE was 0.42^oC at (thermocouple 10). This AAE and MAE occurred at 6:30 am.

In Figure 5.37, the AAE was 0.87^oC while the MAE was 1.74^oC at (thermocouple 14). This AAE and MAE occurred at 1:40 pm. The highest temperature predicted occurred on the south-side on the vertical surface of the bottom flange. The predicted temperatures of the FE analysis have good agreement with the experimental temperatures for both the positive and the negative lateral temperature distributions of the bottom flange.
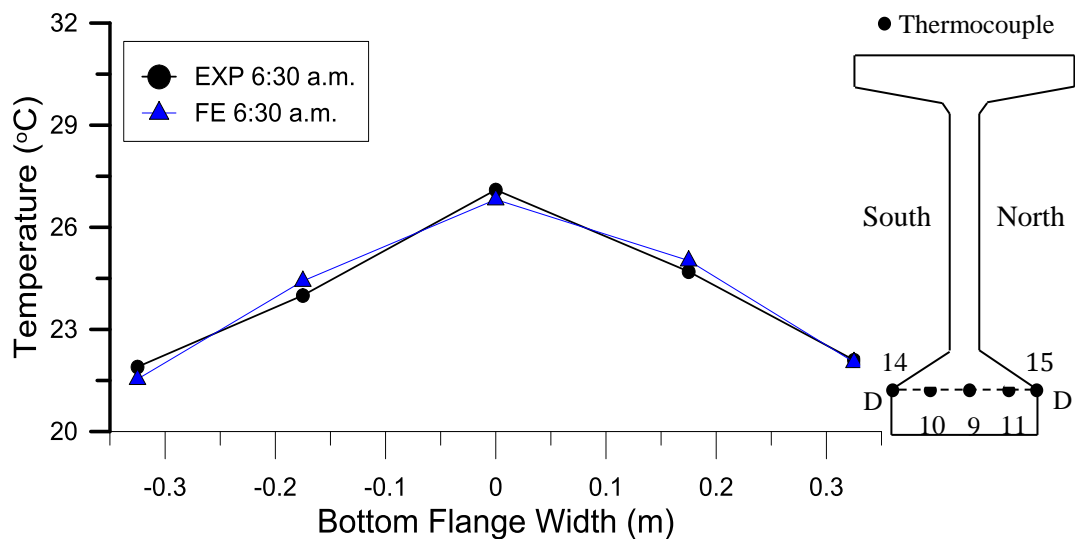
Figure 5.36 Measured and predicted maximum negative lateral temperature distributions along width of the bottom flange of the girder on June1st
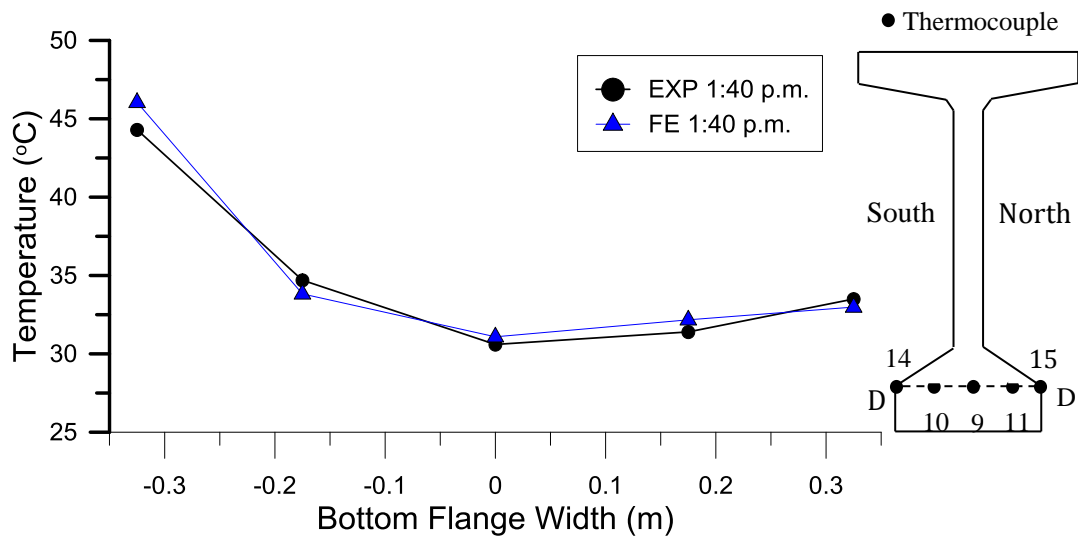
Figure 5.37 Measured and predicted maximum positive lateral temperature distributions along width of the bottom flange of the girder on June1[st]

Also Figure 5.38 and 5.39 compares the measured and predicted maximum negative and positive lateral temperature distributions at across web of the girder on June 1st. As shown in Figure 5.38 includes temperature difference, defined by the AAE was 0.57^{o}C while the MAE was 0.72^{o}C at (thermocouple 7). This AAE and MAE occurred at 6:30 am.

In Figure 5.39, the AAE was 1.5^{o}C and 0.83^{o}C while the MAE was 2.6^{o}C and 1.4^{o}C at (thermocouple 21). This AAE and MAE occurred at 12:00 pm and 1:00 pm respectively. The highest temperature predicted occurred on the south-facing of vertical surface due to highest solar radiation on that surface. As shown Figure 5.40 and 5.41, temperature contours at 12:00 pm and 1:00 pm on June 1st. The predicted temperatures of the FE analysis have good agreement with the experimental temperatures for both the positive and the negative lateral temperature distributions at across web of the girder.
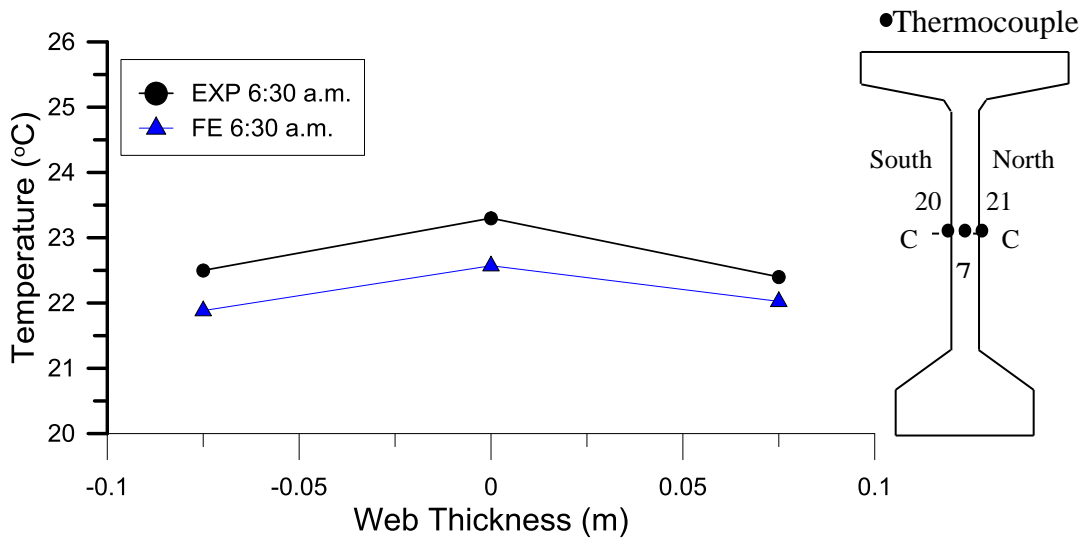
Figure 5.38 Measured and predicted maximum negative lateral temperature distributions at across web of the girder on June1[st]
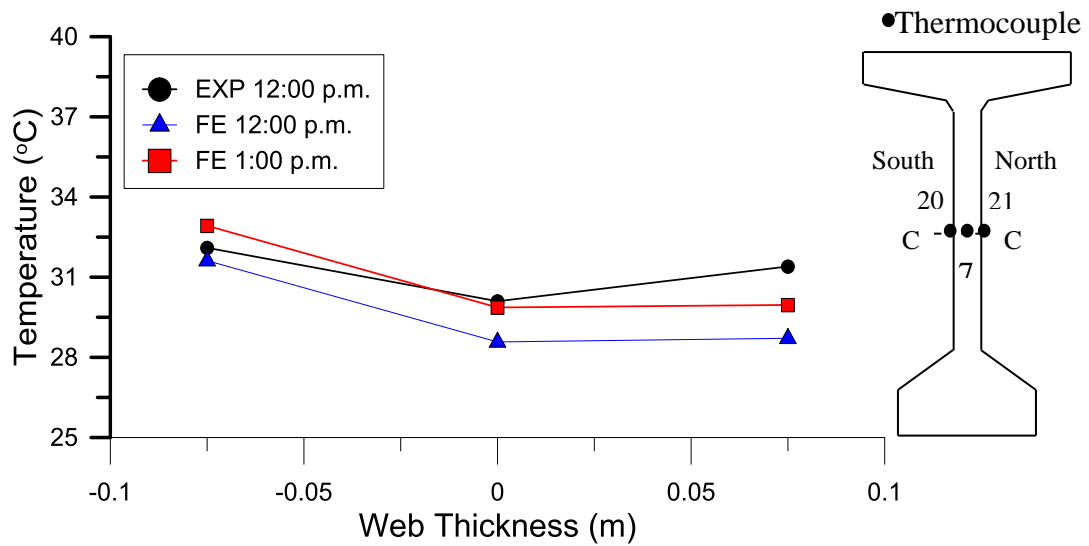
Figure 5.39 Measured and predicted maximum positive lateral temperature distributions at across web of the girder on June1[st]
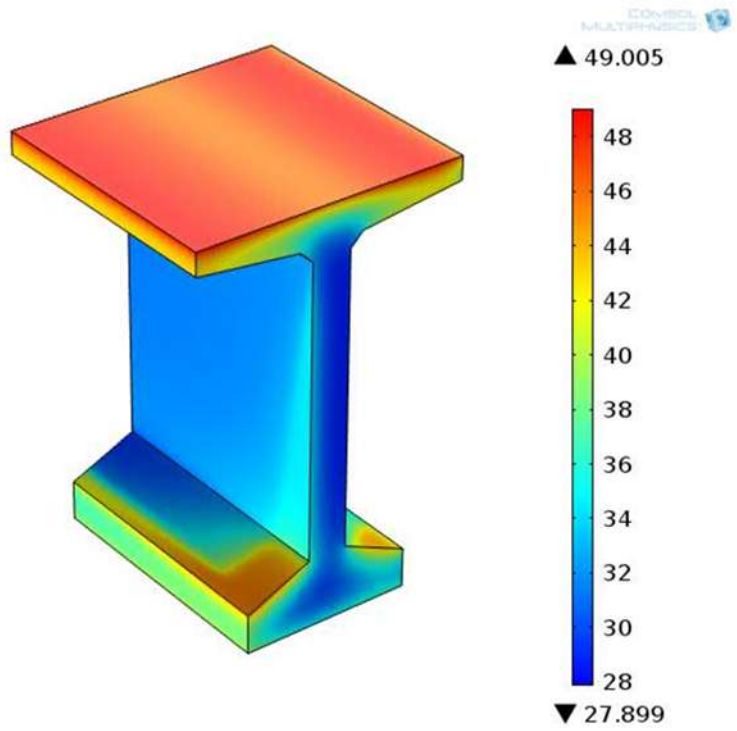
Figure 5.40 Temperature contours at 12:00 pm on June 1st
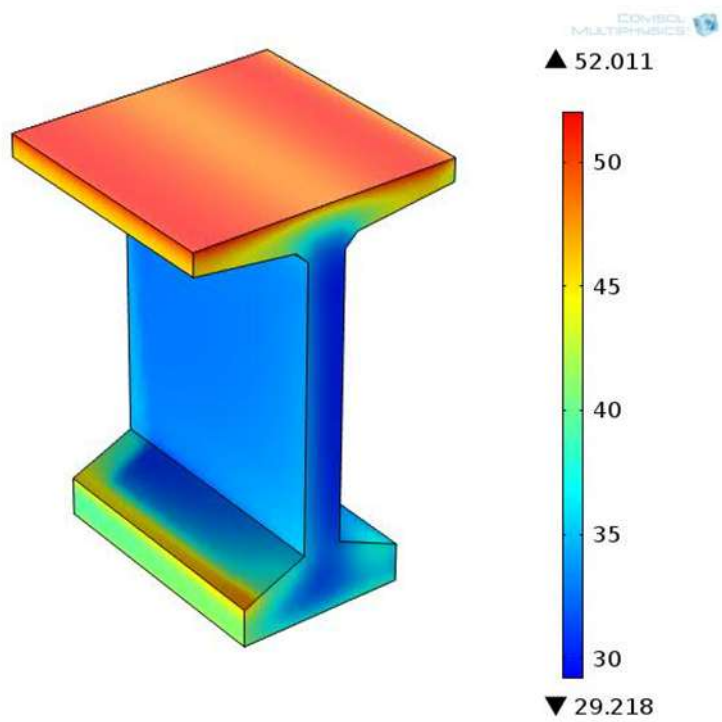
Figure 5.41 Temperature contours at 1:00 pm on June 1st

5.7 Vertical Temperature Distributions on November 15th

Based on the predicted and measured, the vertical temperature differences were calculated from the difference of the lowest and highest temperatures along the web heights of the girder (A-A line). The highest temperature in the girder was predicted and measured on the top surface along of the top flange and the lowest temperature was on along the bottom flange. Figure 5.42 and 5.45 compares the measured and predicted maximum negative and positive vertical temperature distributions. The temperatures in the girder web showed relatively highest increases on the vertical surface because high solar radiation, on the other hand the temperature distribution in the web increased with variations from the summer to the fall.

Furthermore, Figure 5.42 includes temperature distribution; defined by the AAE was 1.14^{o}C and 1.16^{o}C while the MAE was 2.2^{o}C and 1.9^{o}C at (thermocouple 7). This AAE and MAE occurred at 7:40 am and 8:10 am respectively. As shown Figure 5.43 and 5.44 temperature contours at sunrise at 7:40 am and 8:10 am on November 15th.

In Figure 5.45, the AAE was 1.6^{o}C and 1.1^{o}C while the MAE was 2.9^{o}C at (thermocouple 6) and 1.7^{o}C at (thermocouple 7). This AAE and MAE took place at 1:00 pm and 12:10 pm respectively. As shown Figure 5.46 and 5.47 temperature contours at 1:00 pm and 12:10 pm on November 15th. The predicted temperatures of the FE analysis have good agreement with the experimental temperatures for both the positive and the negative vertical temperature distributions.
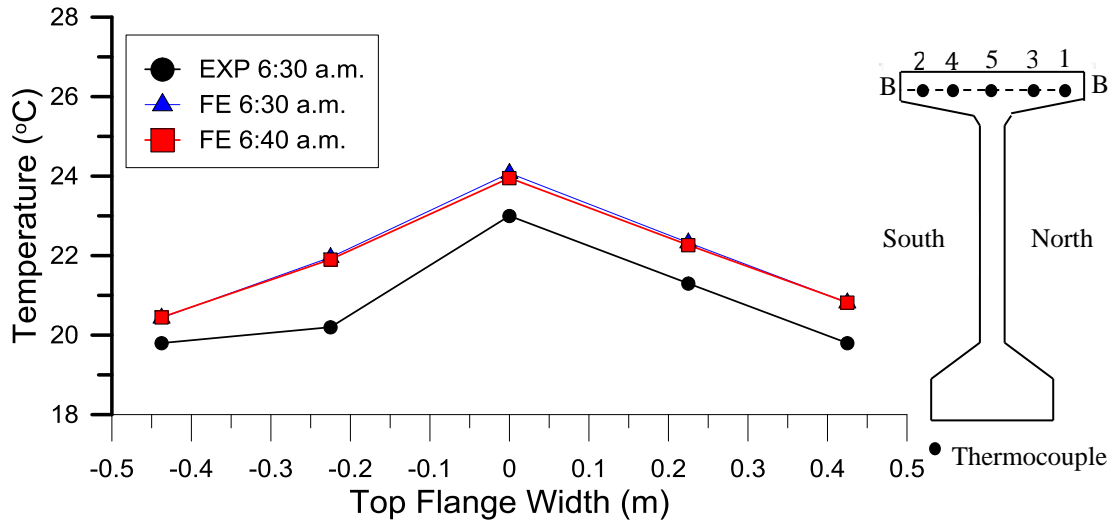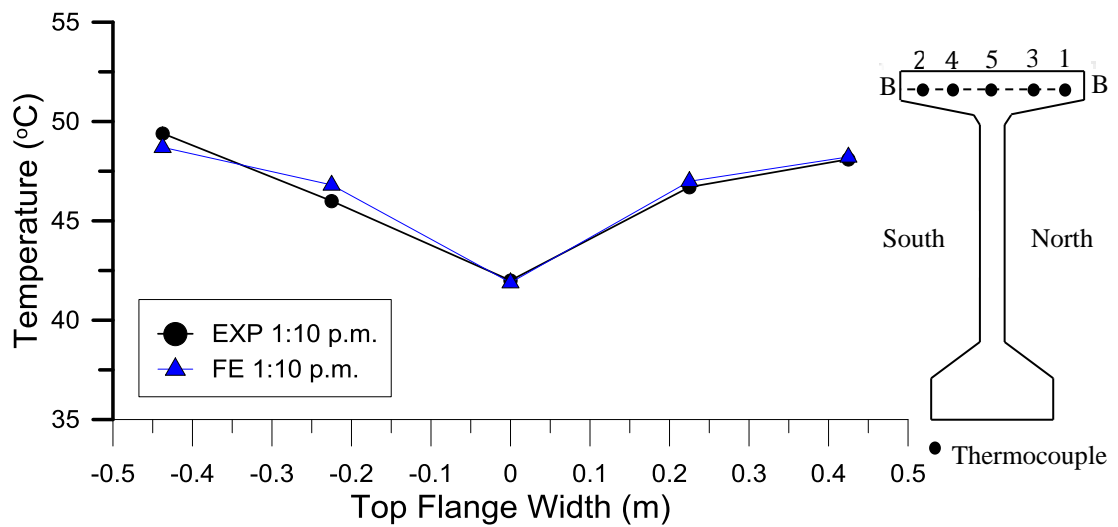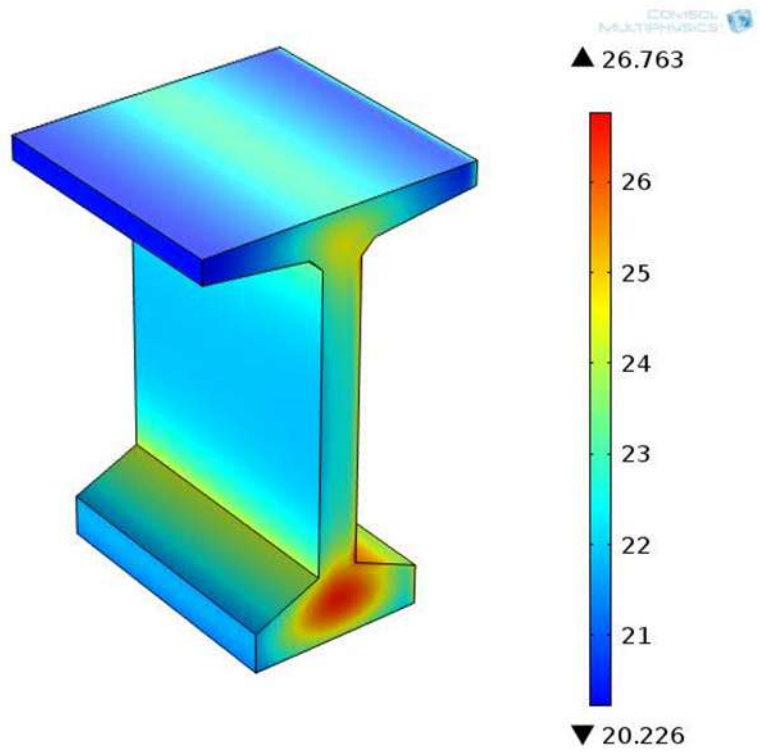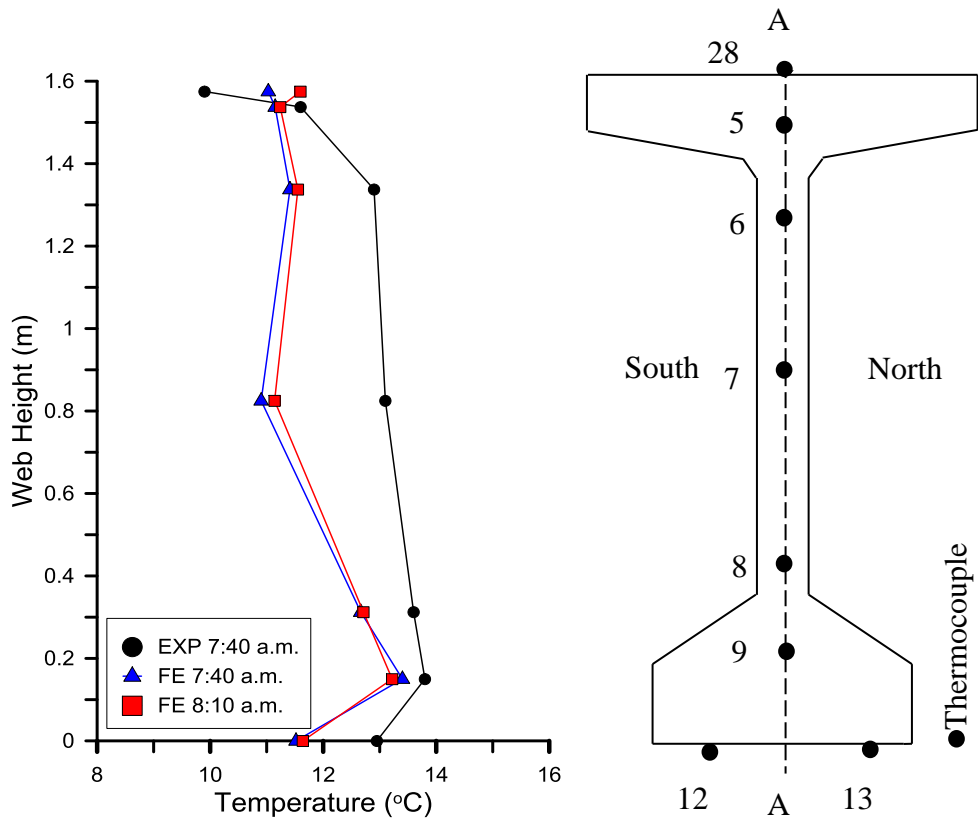
Figure 5.42 Measured and predicted maximum negative vertical temperature distributions along the depth of the girder on November 15th
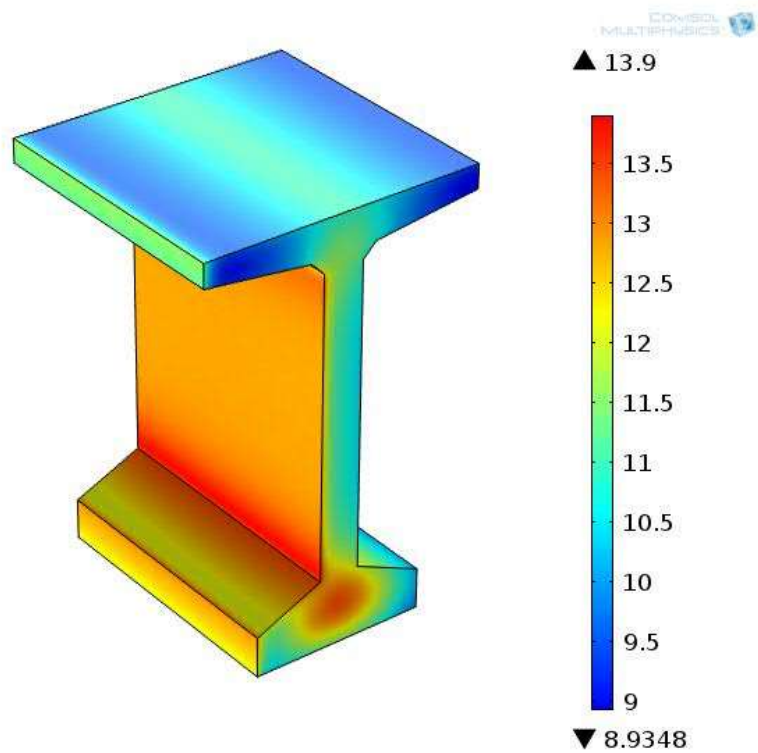
Figure 5.43 Temperature contours at sunrise at 7:40 am on November 15th

Figure 5.44 Temperature contours at sunrise at 8:10 am on November 15th
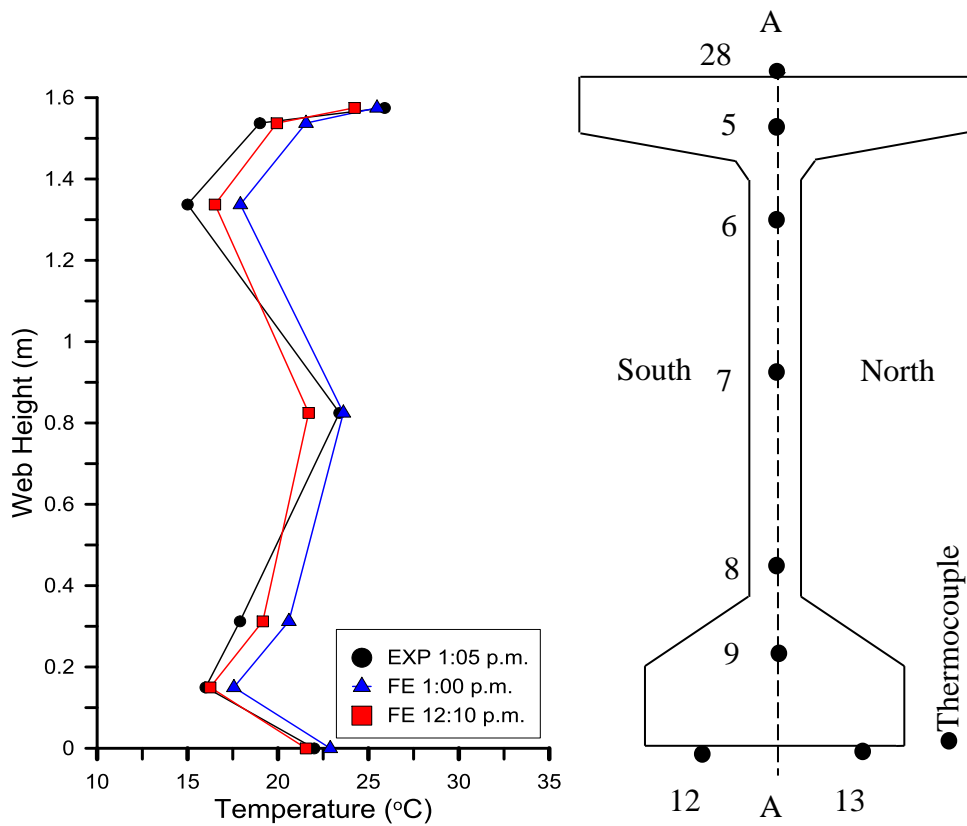
Figure 5.45 Measured and predicted maximum positive vertical temperature distributions along the depth of the girder on November 15th
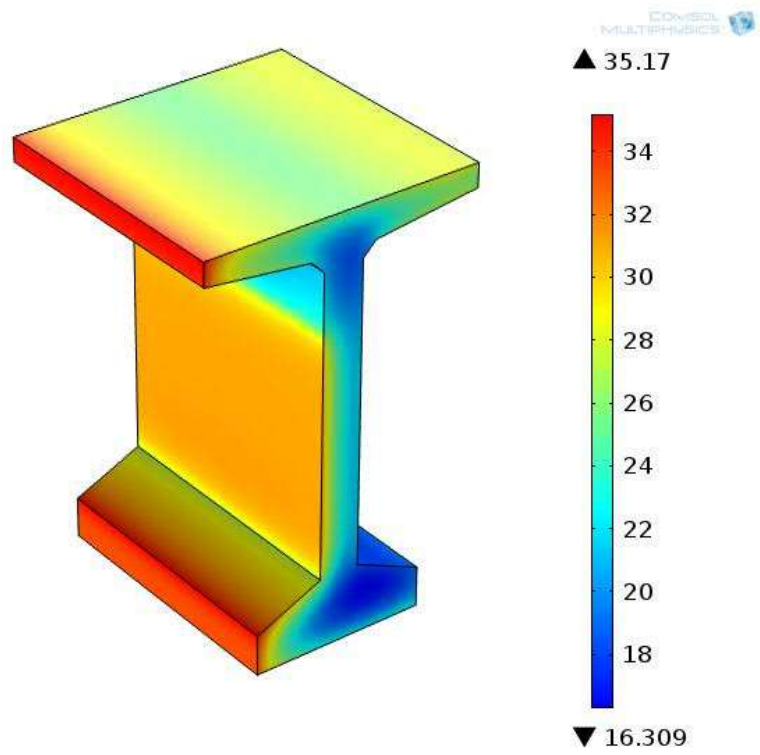
Figure 5.46 Temperature contours at 1:00 pm on November 15th
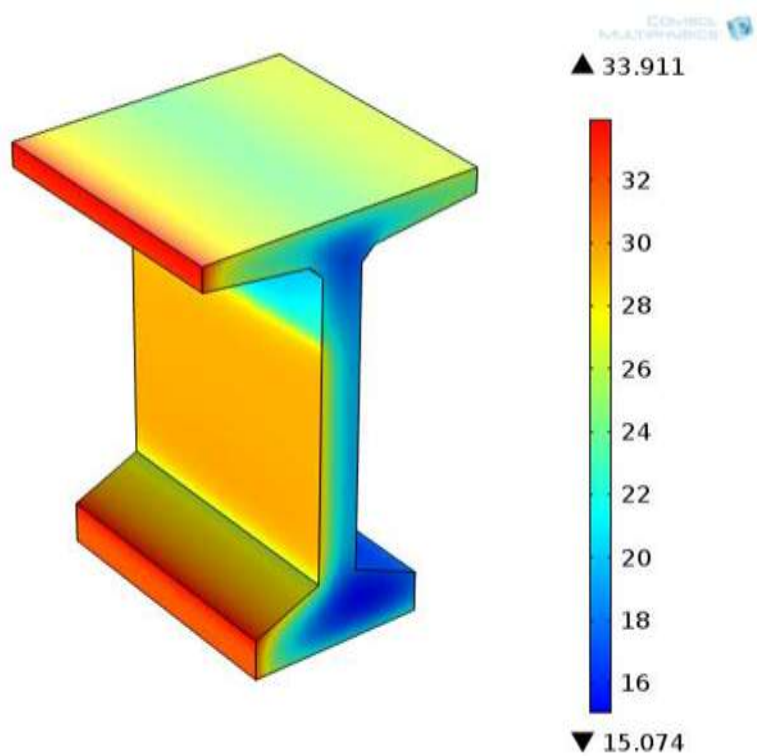
Figure 5.47 Temperature contours at 12:10 pm on November 15th

5.8 Lateral Temperature Distributions on November 15th

Furthermore the vertical temperature differences, the lateral temperature differences were computed from the differences between the lowest and highest temperatures in along width of the top flange, across the web, and along width of the bottom flange of the girder. Figure 5.48 and 5.50 includes compares the measured and predicted maximum negative and positive lateral temperature distributions at along the width of the top flange of the girder. As shown in Figure 5.48, the locations thermocouple at mid-span was installed along width of the top flange of the girder (B-B line).

As shown in Figure 5.48, the AAE was $0.26^{o}C$ while the MAE was $0.44^{o}C$ at (thermocouple 5). This AAE and MAE occurred at 7:40 am. Figure 5.49 shows temperature contours at sunrise at 7:20 am on November 15th. In Figure 5.50, the AAE was $1.8^{o}C$ and $0.9^{o}C$ while the MAE was $2.3^{o}C$ and $1.9^{o}C$ at (thermocouple 1) and (thermocouple 2) respectively. This AAE and MAE took place at 1:40 pm and 12:50 pm respectively. The highest temperature predicted took place on the south-side of the top flange and the lowest temperature took place in the middle of the top flange. As shown Figure 5.50 and 5.51, temperature contours at 1:40 pm and 12:50 pm on November 15th.
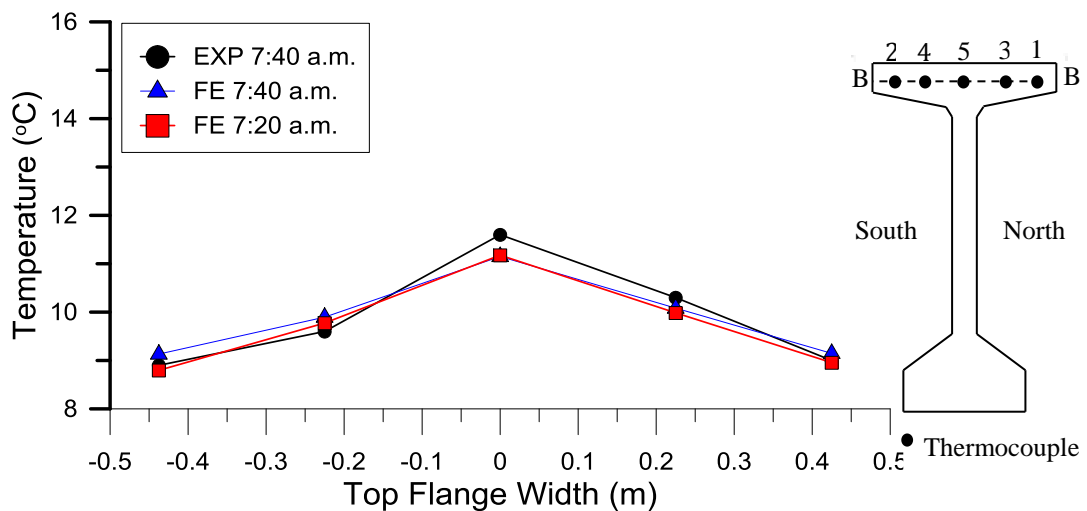
Figure 5.48 Measured and predicted maximum negative lateral temperature distributions along width of the top flange of the girder on November 15th

70

Figure 5.49 Temperature contours at sunrise at 7:20 am on November 15th

Figure 5.50 Measured and predicted maximum positive lateral temperature distributions along width of the top flange of the girder on November 15th

.

71
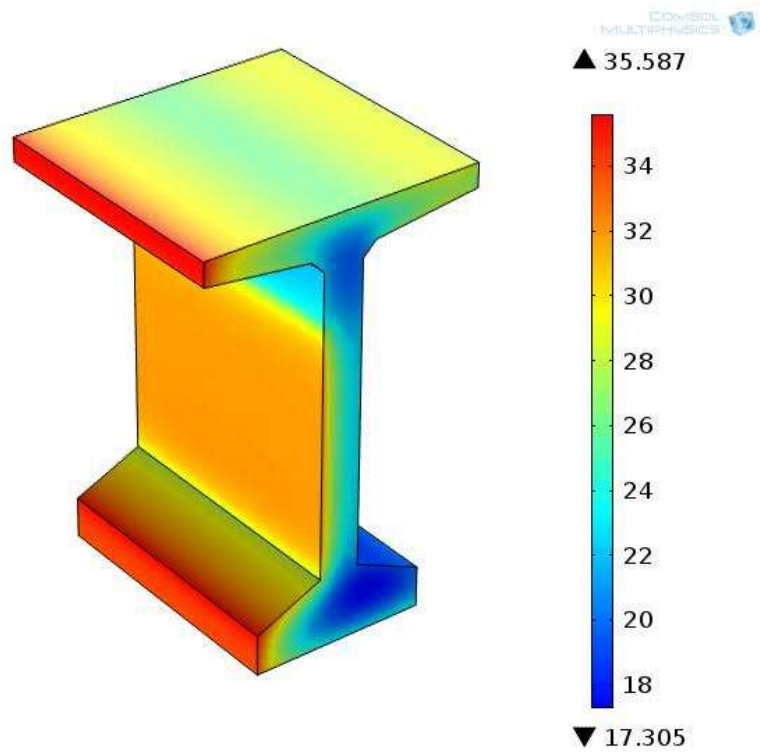
Figure 5.51 Temperature contours at 1:40 pm on November 15th
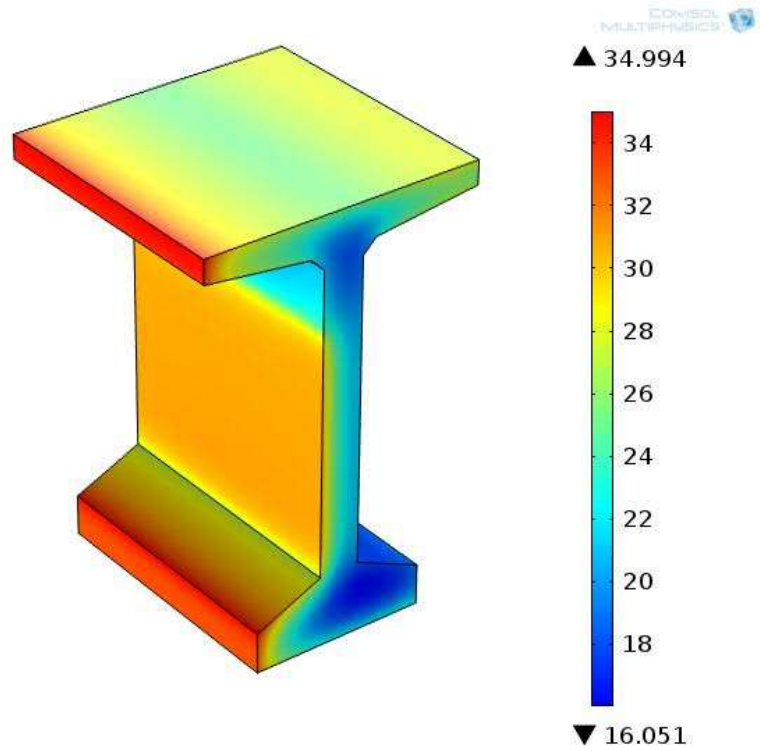
Figure 5.52 Temperature contours at 12:50 pm on November 15th

In addition, as shown in Figure 5.53, compares the measured and predicted maximum negative lateral temperature distributions along the width of the bottom flange of the girder and the locations thermocouple at mid-span was installed along width of the bottom flange of the girder (D-D line). The highest temperature predicted occurred on the middle of the bottom flange and the AAE was $1.3^{o}C$ and $1.0^{o}C$ while the MAE was $2.3^{o}C$ and $2.2^{o}C$ at (thermocouple 11). This AAE and MAE occurred at 7:40 am and 7:30 am respectively. Figure 5.54 shows temperature contours at sunrise at 7:30 am on November 15th.

Also Figure 5.55, includes compares the measured and predicted maximum positive lateral temperature distributions. The highest temperature predicted occurred on the south-side on the vertical surface of the bottom flange. The AAE was $2.0^{o}C$ and $0.8^{o}C$ while the MAE was $3.4^{o}C$ and $2.0^{o}C$ at (thermocouple 15). This AAE and MAE took place at 2:00 pm and 1:00 pm respectively. Figure 5.56 shows temperature contours at 2:00 pm on November 15th.
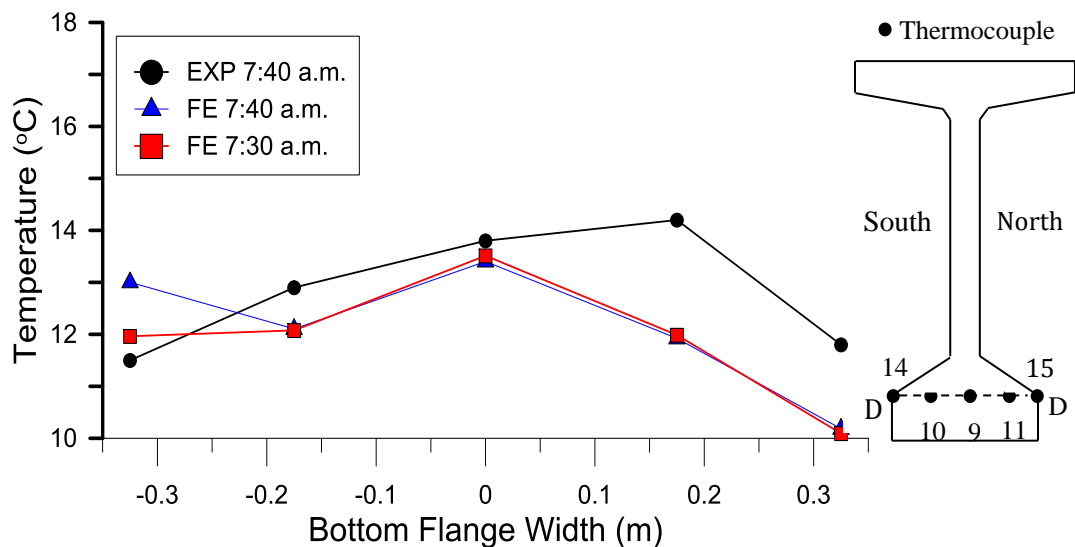
Figure 5.53 Measured and predicted maximum negative lateral temperature distributions along width of the bottom flange of the girder on November 15th
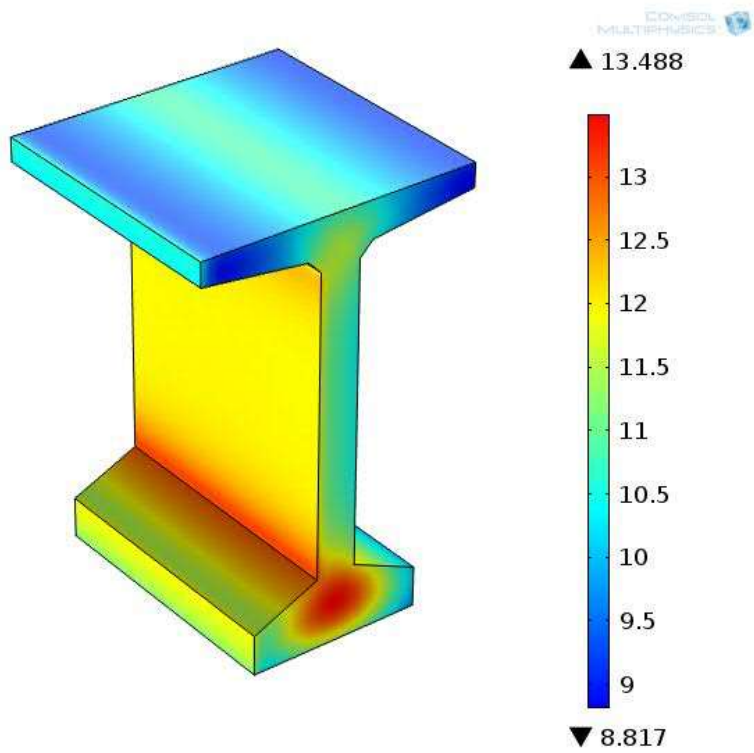
Figure 5.54 Temperature contours at sunrise at 7:30 am on November 15th
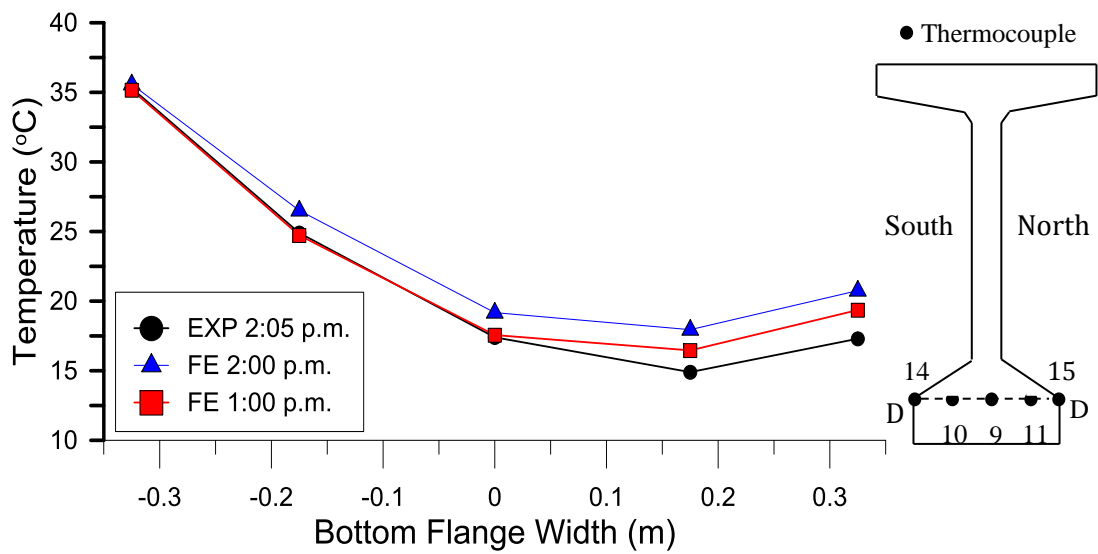
Figure 5.55 Measured and predicted maximum positive lateral temperature distributions along width of the bottom flange of the girder on November 15th
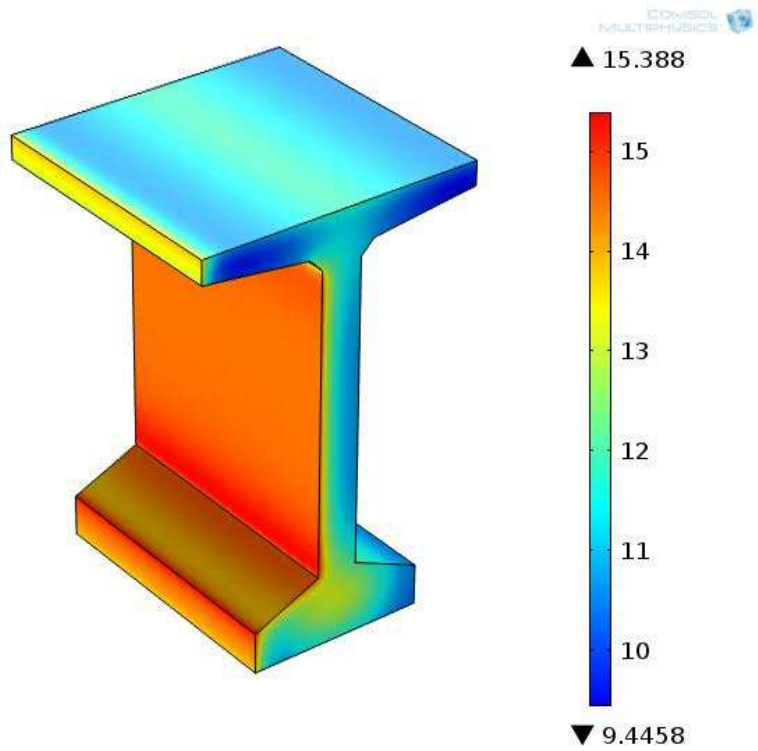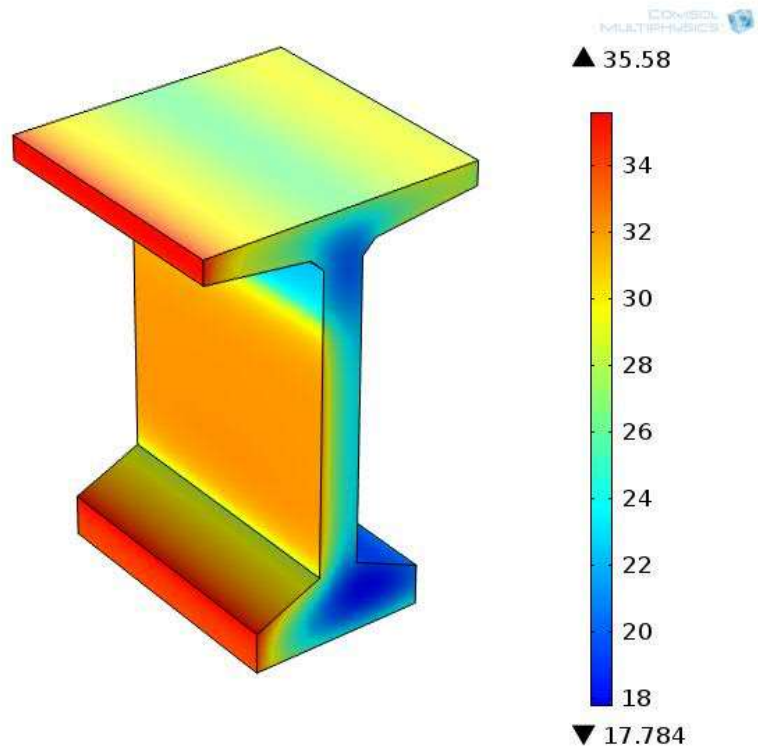
Figure 5.56 Temperature contours at 2:00 pm on November 15th

In Figure 5.57, the locations thermocouple at mid-span was installed across the web of the girder (C-C line), the highest temperature predicted occurred on the south-facing of vertical surface due to high solar radiation on that surface. The AAE was 1.5^{o}C, 1.3^{o}C and 1.8^{o}C while the MAE was 2.19^{o}C, 2.24^{o}C and 2.1^{o}C at (thermocouple 7). This AAE and MAE occurred at 7:40 am, 7:30 am and 6:40 am respectively. Figure 5.58 shows temperature contours at sunrise at 6:40 am on November 15th.

In Figure 5.59, also the highest temperature predicted occurred on the south-facing, the AAE was 0.7^{o}C while the MAE was 1.2^{o}C at (thermocouple 20). This AAE and MAE occurred at 1:00 pm. The predicted temperatures of the FE analysis have good agreement with the experimental temperatures for both the positive and the negative lateral temperature distributions.
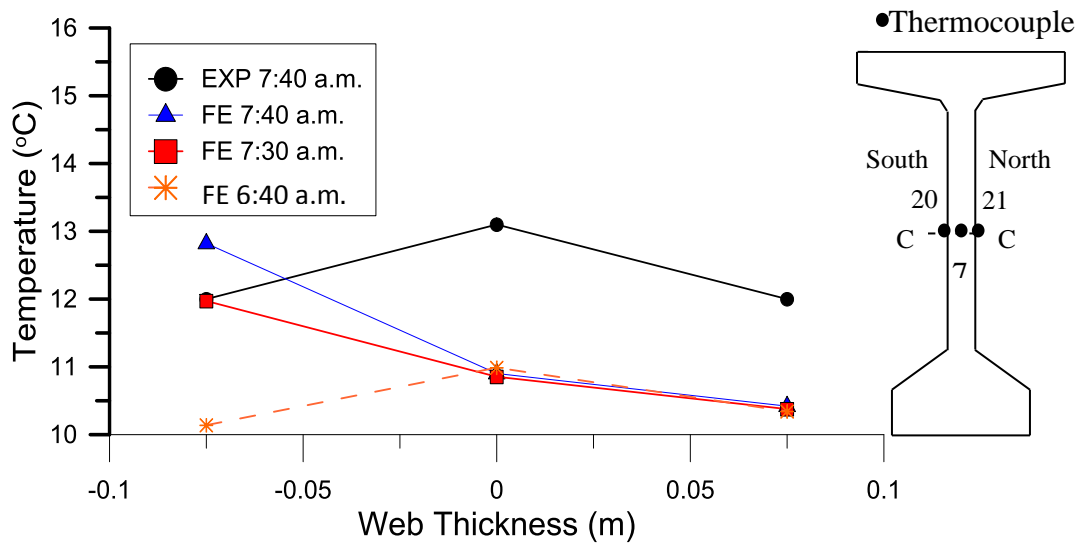
Figure 5.57 Measured and predicted maximum negative lateral temperature distributions at across web of the girder on November 15th
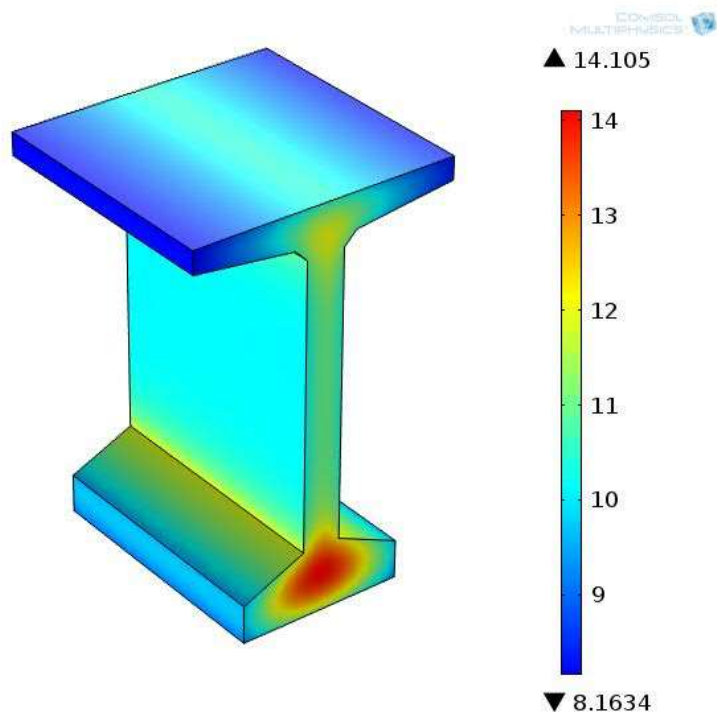
Figure 5.58 Temperature contours at sunrise at 6:40 am on November 15th
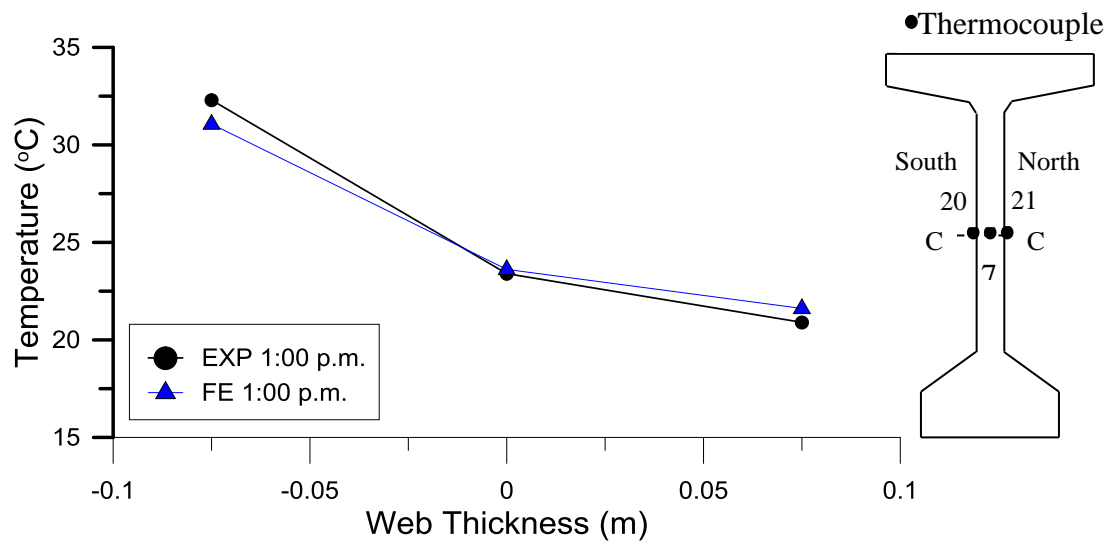
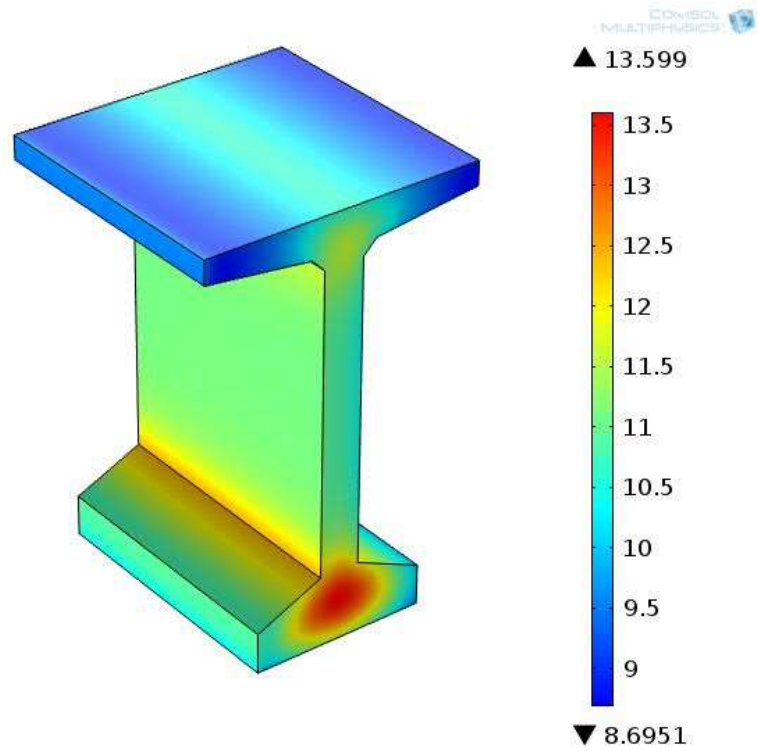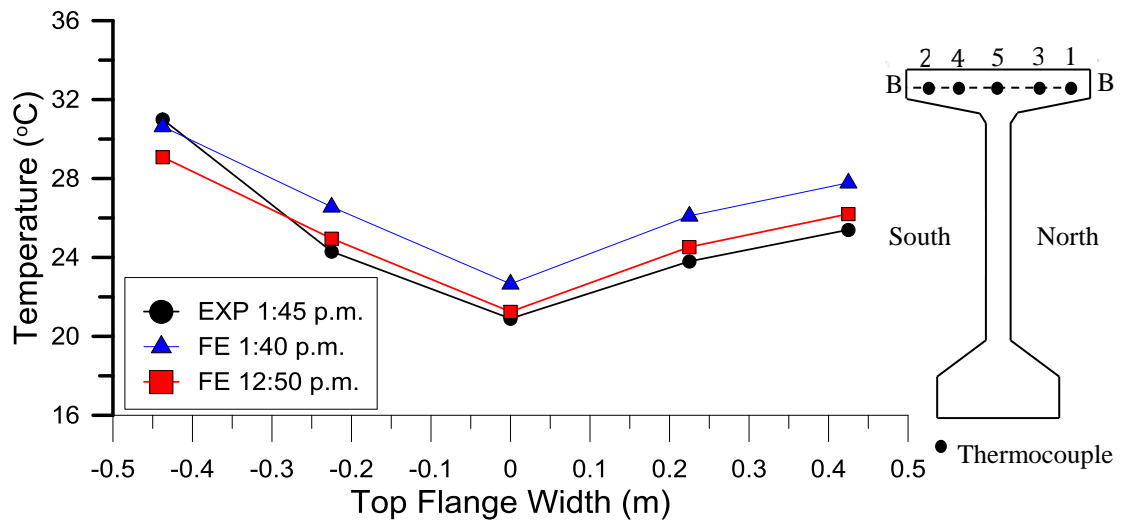**Figure 5.59** Measured and predicted maximum positive lateral temperature distributions at across web of the girder on November 15th

CHAPTER 6

EXTREME TEMPERATURE DISTRIBUTION AND GRADIENTS IN GAZIANTEP

6.1 Environmental Conditions

From the meteorological air temperature records of 30 years were utilized to evaluate the maximum temperature gradient in summer condition in the region of Gaziantep, Turkey. This research evaluates temperatures variations in daily environmental conditions, ambient air, wind speed and solar radiation. Table 6.1 summarizes the hourly solar radiation, daily minimum and maximum air temperatures, and daily average wind speed computed from the measurements for chosen sunny days (30 July), on which largest temperature distributions have been measured.

Table 6.1 The daily and hourly environmental conditions for chosen sunny days through the measurements from 30 July in Gaziantep

Dates	Hourly solar radiation (w/m^2)	Daily air temperature (^oC)		Daily wind speed (m/sec)		Albedo
		Maximum	Minimum	Average	Maximum	
30-July	1013	43.9	21	0.7	1.9	0.2

6.1.1 Solar radiation

Due to variation in the hourly solar radiation during the four seasons of the year, the largest temperature distributions were in 30 July and smallest was in 23 April. Table 6.2 summarizes the hourly solar radiation during 30 July, 2 September, 3 December and 23 April. Maximum hourly solar radiations occurred in summer (30 July), which was 1013 W/m^2 while the minimum hourly solar radiation occurs in 23 April, which was 670 W/m^2.

Table 6.2 Maximum hourly solar radiation for the four seasons of the year

Dates	Maximum hourly solar radiation (w/m^2)
30 July	1013
2 Sptember	914
3 December	795
23 April	670

6.1.2 Air temperature

As expected, the minimum and maximum daily air temperatures increases on the 30 July and decreases after 30 July to the 3 December. As notes for the four months, 30 July, 2 September, 3 December and 23 April variation the surrounding air temperatures as a function of the time of the day, Table 6.3 summarizes maximum and minimum daily air temperatures for the four seasons of the year.

Table 6.3 Maximum and minimum daily air temperature for the four seasons of the year

Dates	Daily Air Temperature (^{o}C)	
	Maximum	Minimum
30 July	43.9	21
2 September	40.9	16
3 December	24.9	1.0
23 April	33.9	11

6.1.3 Wind speed

This study evaluates the differences in daily average wind speed which taken from the meteorological stations records of 30 years in the region of Gaziantep, Turkey. The wind speed which was taken range between 0 to 1.9 m/sec and the average wind speed was 0.7 m/sec.

6.2 Vertical Temperature Distribution and Gradients

Based on the four seasons' largest vertical thermal loads in Gaziantep, the maximum vertical and lateral temperature distributions and gradients in the girder are discussed. This study shows the positive and negative vertical temperature gradients of the four days 23 April, 30 July, 2 September and 3 December. As predicted, the magnitudes of the temperatures were the highest in the 30 July and decreased with decreases in air temperature and solar radiation from the 30 July to the 3 December. Table 6.4, summarizes maximum predicted positive vertical temperature gradients and temperature distributions.

Table 6.4 Maximum predicted positive vertical temperature gradients and temperature distributions for the four seasons of the year

Dates	The maximum predicted positive vertical temperature gradient ^{o}C	The maximum positive vertical temperatures ^{o}C	Times PM
30 July	20	59.1	1:50
2 September	16.7	50.7	1:40
23 April	13.9	41.3	1:50
3 December	10.6	30.4	3:20

Since vertical temperature differences in the bridge girder mainly based on the intensity of solar radiation on the top surface of the girder, Figure 6.1, exhibited, the largest vertical temperature gradient along the web heights of the girder was in summer 30 July. As note seasonal variations from the 30 July to the 3 December, due to the increased solar radiation intensity and the lower altitude of the sun on the vertical surfaces of the girder, the vertical temperature gradients decreased. The predicted vertical temperature gradients in 23 April, 30 July and 2 September, were a rapid decrease from the top surface and smallest gradient in the web while was in 3 December decreased on the top surface and increased in the web because an increase in the solar radiation intensity on the vertical surface.

In addition, the autumn, spring and summer exhibited similar in vertical temperature gradients.

In Figure 6.2, the largest vertical temperature gradient was in autumn because solar radiation intensity on the top surface of the girder. The predicted vertical temperature gradients in 23 April, 30 July and 2 September, were decreased on the top surface and increased in the web because an increase in the solar radiation intensity on the vertical surface while was in 3 December a rapid decrease from the top surface and smallest gradient in the web. The maximum predicted negative vertical temperature gradient along the web heights occurred in 2 September. Table 6.5, summarizes maximum predicted negative vertical temperature gradients and temperature distributions.

Table 6.5 Maximum predicted negative vertical temperature gradients and temperature distributions for the four seasons of the year

Dates	The maximum predicted negative vertical temperature gradient ^{o}C	The maximum negative vertical temperatures ^{o}C	Times AM
30 July	-6.7	37.4	3:40
2 September	-6.8	34.1	2:50
23 April	-5.4	28	1:50
3 December	-6.1	18.4	1:50
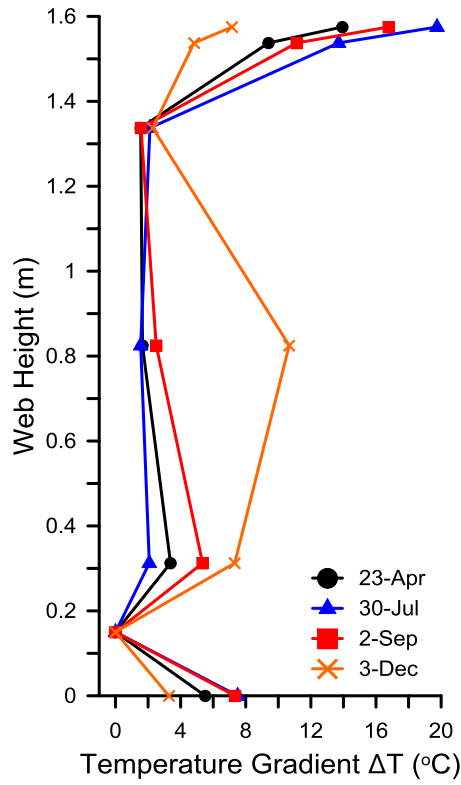
Figure 6.1 Maximum positive vertical temperature gradients for the four seasons of the year
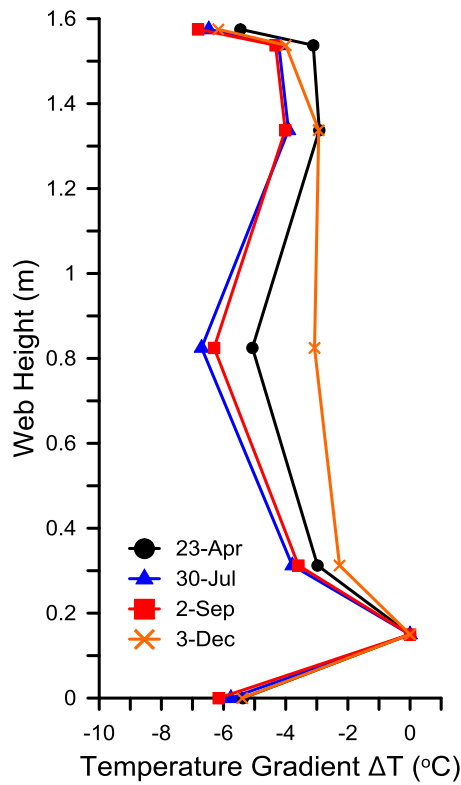
Figure 6.2 Maximum negative vertical temperature gradients for the four seasons of the year

6.3 Transverse Temperature Distribution and Gradients

This research also investigates maximum transverse temperature distributions and gradients along the width of the top flange, along the width of the bottom flange and across the web of the girder, in which the maximum lateral temperature gradients were observed. The positive and negative lateral temperature gradients along the width of the top flange for the four seasons of the year. As predicted, the magnitudes of the temperatures were the highest in 30-July and the smallest in 3-December. The maximum positive lateral temperatures along width of the top flange as shown in Table 6.6.

Table 6.6 Maximum predicted positive lateral temperature gradients and temperature distributions along width of the top flange for the four seasons of the year

Dates	The maximum predicted positive lateral temperature gradient ^{o}C TF	The maximum positive lateral temperatures ^{o}C TF	Times PM
30 July	8.2	61.3	2:10
2 September	9.4	55.6	2:30
23 April	6.9	43.8	2:10
3 December	9.5	32.8	2:40

However, the positive lateral temperature gradient of the top flange as shown in Figure 6.3, the maximum predicted positive lateral temperature gradient along width of the top flange occurred in 3 December which was 9.5°C. This temperature gradient occurred at 2:40 pm, can be observed in Table 6.6.

In Figure 6.4 the maximum negative lateral temperature gradient along width of the top flange obtained from seasonal extreme climate conditions in Gaziantep occurred in summer 30 July which was -6.6°C. This temperature gradient occurred at 2:20 am. As shown in Table 6.7.

Table 6.7 Maximum predicted negative lateral temperature gradients and temperature distributions along width of the top flange for the four seasons of the year

Dates	The maximum predicted negative lateral temperature gradient ^{o}C TF	The maximum negative lateral temperatures ^{o}C TF	Times AM
30 July	-6.6	36.1	2:20
2 September	-6.1	30.0	2:50
23 April	-5.1	25.2	1:50
3 December	-4.8	11.6	4:00

Figure 6.3 Maximum positive lateral temperature gradients along width of the top flange for the four seasons of the year
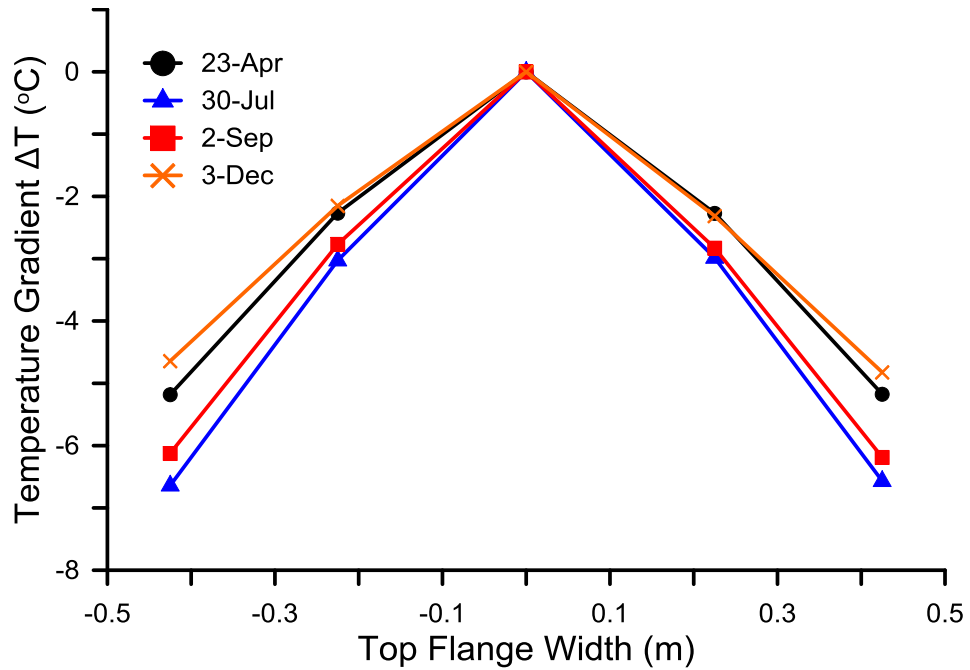
Figure 6.4 Maximum negative lateral temperature gradients along width of the top flange for the four seasons of the year

Figure 6.5 and 6.6 show the positive and negative lateral temperature gradients along the width of the bottom flange for the four seasons of the year. As predicted, the magnitudes of the temperatures were the highest in 30 July and the smallest in 3 December can be observed Table 6.8.

Table 6.8 Maximum predicted positive lateral temperature gradients and temperature distributions along width of the bottom flange for the four seasons of the year

Dates	The maximum predicted positive lateral temperature gradient ^{o}C BF	The maximum positive lateral temperatures ^{o}C BF	Times PM
30 July	22.1	60.9	1:30
2 September	24.6	57.8	1:40
23 April	17.4	44.1	1:30
3 December	25.1	40.5	1:40

As shown in Figure 6.5, the maximum predicted positive lateral temperature gradient along width of the bottom flange occurred in winter 3 December was 25.1°C. This temperature gradient occurred at 1:40 pm, as shown Table 6.8. In Figure 6.6 the maximum negative lateral temperature gradient along width of the bottom flange obtained from seasonal extreme climate conditions in Gaziantep occurred in 2 September which was -10.7°C. This temperature gradient occurred at 12.50 am as shown in Table 6.9.
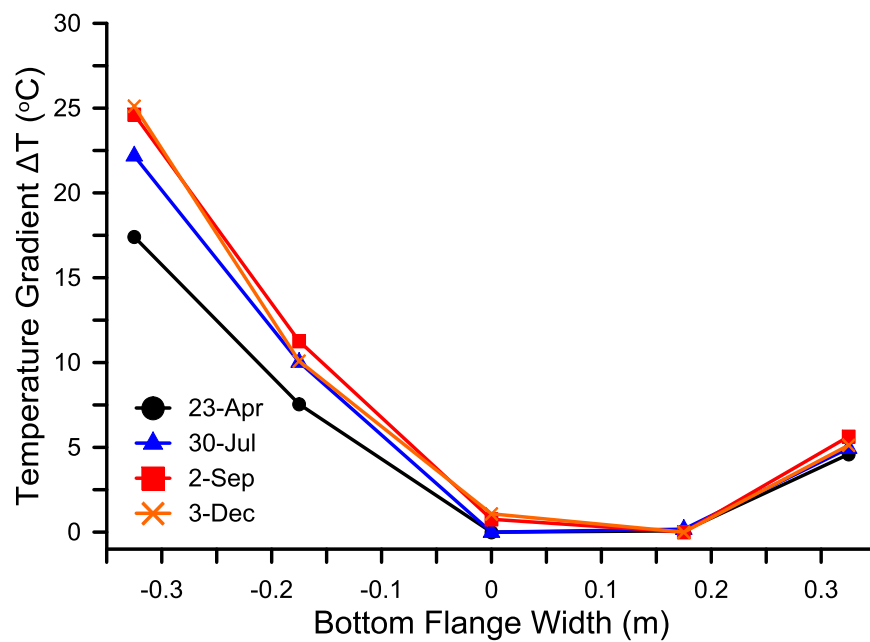
Figure 6.5 Maximum positive lateral temperature gradients along width of the bottom flange for the four seasons of the year
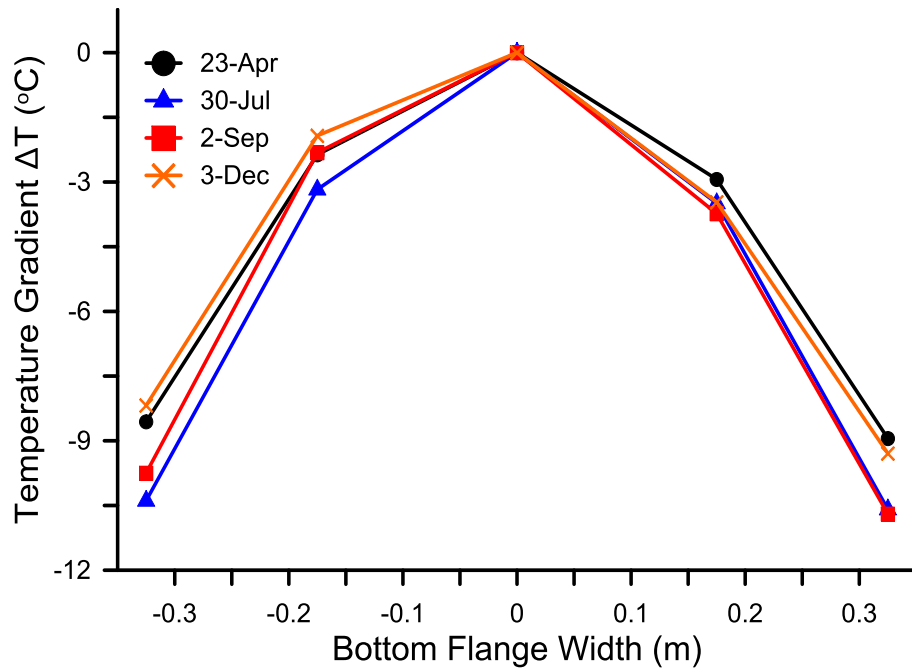
Figure 6.6 Maximum negative lateral temperature gradients along width of the bottom flange for the four seasons of the year

Table 6.9 Maximum predicted negative lateral temperature gradients and distributions along width of the bottom flange for the four seasons of the year

Dates	The maximum predicted negative lateral temperature gradient ^{o}C BF	The maximum negative lateral temperatures ^{o}C BF	Times AM
30 July	-10.5	39.9	2:10
2 September	-10.7	37.3	12:00
23 April	-8.9	28.0	1:50
3 December	-9.2	18.4	1:50

Figure 6.7 and 6.8 show the positive and negative lateral temperature gradients across the web for the four seasons of the year. As predicted, the magnitudes of the temperatures were the highest in the summer and the smallest in the winter. The maximum positive lateral temperatures across the web were 48.7^{o}C at 7:30 pm in 30 July, as shown in Table 6.10.

Furthermore, the positive lateral temperature gradient across the web as shown in Figure 6.7, the maximum predicted positive lateral temperature gradient across the web occurred in winter 3 December was 11.1°C. This temperature gradient occurred at 12:50 pm, as shown in Table 6.10.

In Figure 6.8, the maximum negative lateral temperature gradient across the web obtained from seasonal extreme climate conditions in Gaziantep occurred in autumn 2 September which was -5.5°C. This temperature gradient occurred at 1:40 am, as shown in Table 6.11.
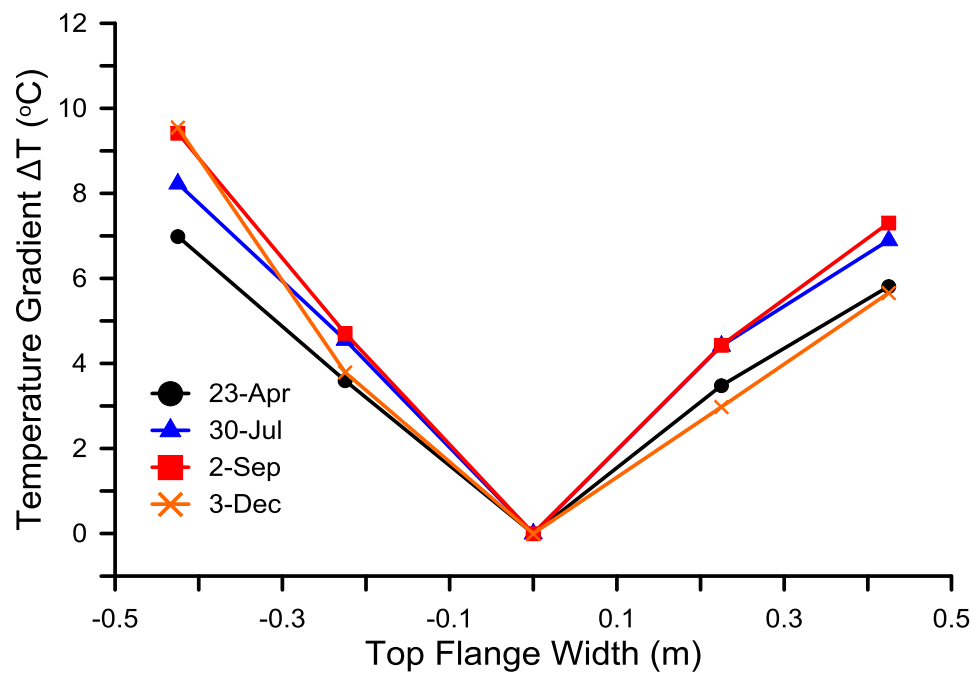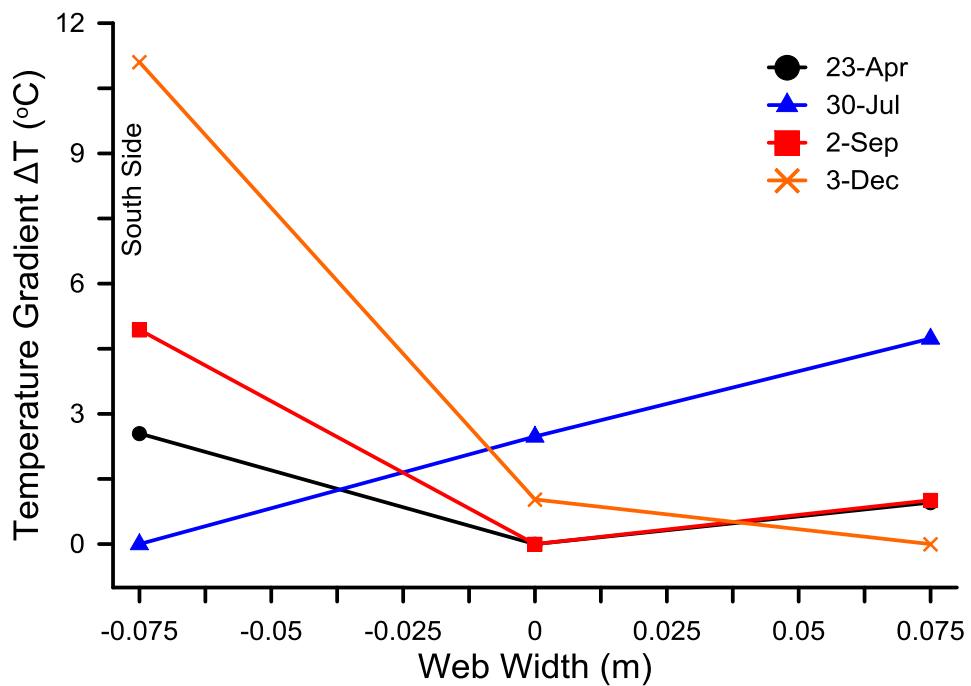

Figure 6.7 Maximum positive lateral temperature gradients across the web for the four seasons of the year
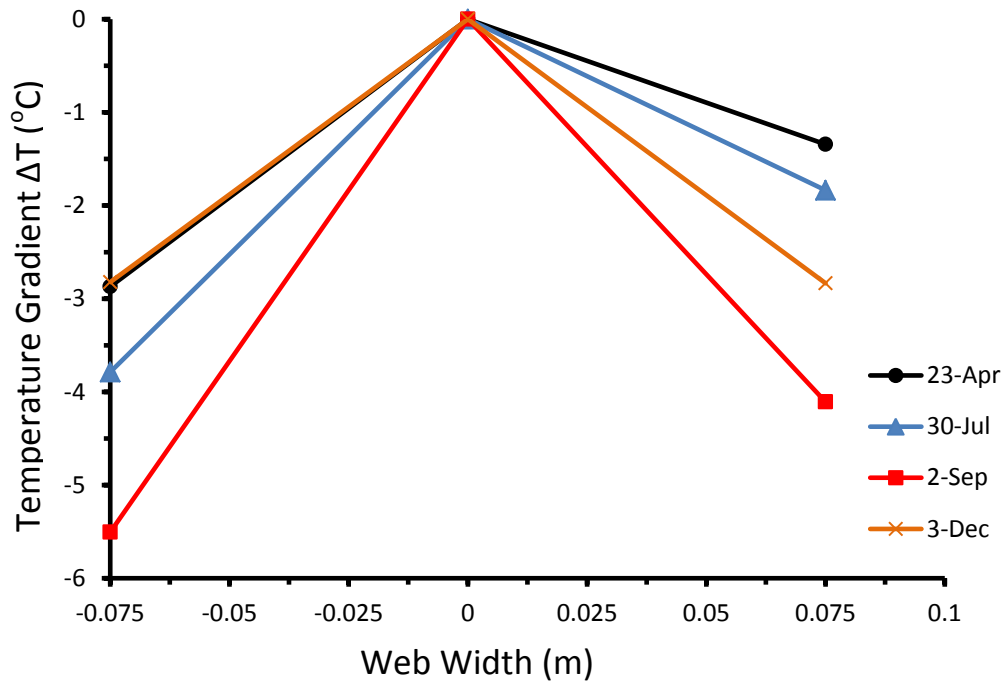
Figure 6.8 Maximum negative lateral temperature gradients across the web for the four seasons of the year

Table 6.10 Maximum predicted positive lateral temperature gradients and temperature distributions across the web for the four seasons of the year

Dates	The maximum predicted positive lateral temperature gradient ^{o}C web	The maximum positive lateral temperatures ^{o}C web	Times PM
30 July	4.7	48.7	7:30
2 September	4.9	45.8	3:50
23 April	2.5	34.4	3:50
3 December	11.1	33.2	12:50

Table 6.11 Maximum predicted negative lateral temperature gradients and temperature distributions across the web for the four seasons of the year

Dates	The maximum predicted negative lateral temperature gradient ^{o}C web	The maximum negative lateral temperatures ^{o}C web	Times AM
30 July	-3.7	35.8	12:10
2 September	-5.5	32.3	1:40
23 April	-2.9	24.2	1:50
3 December	-2.8	19.2	12:00

6.4 Comparison of The Maximum Predicted Positive and Negative Temperature Gradient with The AASHTO 1989 and AASHTO 2007

Based on the vertical temperature gradients, Figures 6.9 and 6.10 compare the maximum predicted temperature gradient from extreme weather conditions of Gaziantep on 30-July with AASHTO 1989 [56] and AASHTO 2007 [57] (Zone 1), (Zone 2), (Zone 3) and (Zone 4). The vertical temperature gradients got during subtracting a minimum temperature from the vertical temperatures at along the depth of the girder A-A line.

The largest predicted vertical temperature differentials, which shows a quick decrease from the top surface and smallest gradient in the web. Since the AASHTO thermal gradients were depended on summer climate conditions, the largest vertical temperature differentials, occurs on June and July was similar to the vertical thermal gradients of the AASHTO specifications.

Due to the bridge temperature gradient variation in concrete temperatures on the height of the structure, the largest recorded variation during time period was defined as the maximum thermal gradient. The data was classified to determine the maximum temperature gradients occurring on the bridge cross section during the monitored months. From the recorded data, it was observed that, in general, the most uniform zone of temperature measurements took place at along the web heights of

the girder which allowed using it as a base line to compute the bottom and top gradients for each measurement time.

This uniform zone helped identify the largest negative and positive temperature gradients matching to the daily temperature variations for each month. Depended on the data, it was determined that the largest positive temperature gradients occurred in bridge during mid-afternoon and largest negative temperature gradients occurred during the early morning hours of each day.

From extreme weather conditions of Gaziantep on 30 July, the largest predicted positive top surface gradient was 20˚C at 1:50 pm on 30 July, while the AASHTO specifications 1989 and 2007 were 30°C in (zone 1), 25.6^{o}C in (zone 2), 22.8^{o}C in (zone 3) and 21.1^{o}C in (zone 4), note both of the AASHTO models (zone 4) agree well with the predicted positive temperature gradient. As compared Figure 6.9 the largest predicted positive design gradient introduced in the current and previous versions of the AASHTO LRFD Code, the shape of predicted temperature gradient shows better agreement with the AASHTO LRFD distribution (zone 4) in that the concrete temperature became uniform closer to the top flange. At the bottom flange, the predicted gradient was 7.5℃, while both the AASHTO suggests a gradient of 2.8℃, therefore, it can be concluded that the AASHTO gradient model is suitable and well for the extreme conditions of Gaziantep with few adjustments.

Similarly, the largest predicted negative gradient -6.8 ˚C at 2:50 am on 2 September while the AASHTO specifications 1989 and 2007 were -9°C in (zone 1), -7.6^{o}C in (zone 2), -6.8^{o}C in (zone 3) and -6.3^{o}C in (zone 4), note both of the AASHTO models (zone 3) agree well and matched with the predicted negative temperature gradient as shown Figure 6.10.

Also the recommended negative design gradient introduced in AASHTO LRFD Specifications (1989 and 2007), and the largest predicted negative gradient. It is interested to note that the top negative temperature gradient is perfectly encompassed by the AASHTO LRFD codes and predicted temperature gradients. At the bottom flange, the predicted gradient was -6.1℃, while both the AASHTO suggests a gradient of -0.8℃, therefore, it can be concluded that the AASHTO gradient model is suitable for the extreme conditions of Gaziantep.
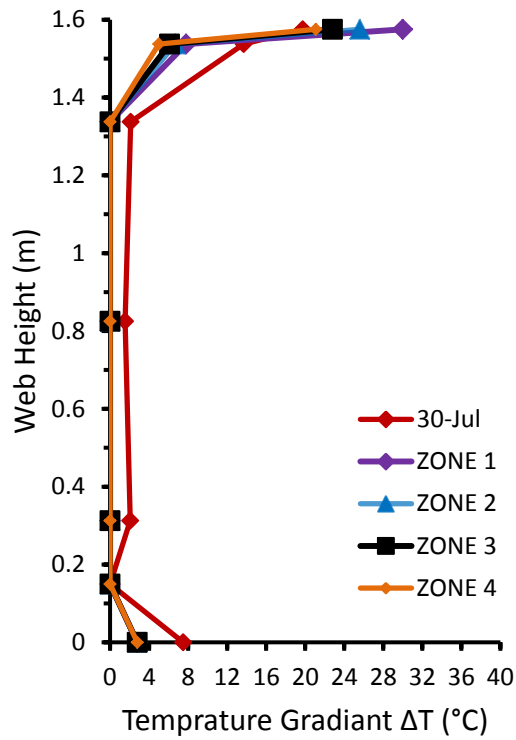
Figure 6.9 Comparison of the maximum predicted positive temperature gradient with AASHTO 1989 [56] and AASHTO 2007 [57] for the four zones
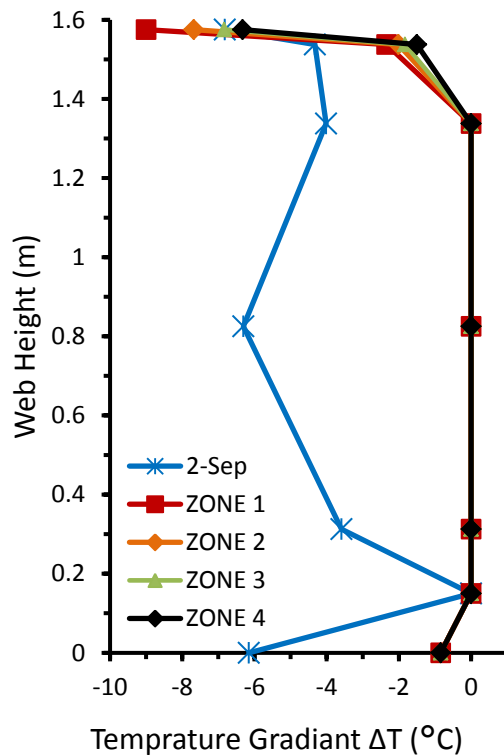
Figure 6.10 Comparison of the maximum predicted negative temperature gradient with AASHTO 1989 [56] and AASHTO 2007 [57] for the four zones

6.5 Comparison of The Maximum Predicted Positive Temperature Gradient with NZ Bridge Manual and BS 5400 Code

Figures 6.11 and 6.12 show a maximum predicted temperature gradient from extreme weather conditions of Gaziantep on 30 July with the gradient distributions of NZ Bridge Manual and BS 5400. The largest predicted positive top surface gradient was 20°C at 1:50 pm on 30 July, while the NZ Bridge Manual and BS 5400 were 32°C and 15.4°C respectively, As shown in Figure 6.11, the fifth order gradient model of the NZ Bridge Manual seems to have conservative largest gradient at the top surface and much higher temperatures along the top surface of the girder. In contrast, the BS 5400 fifth order model shows noticeable variations from the predicted temperatures along the top region of the girder, as shown in Figure 6.12. At the bottom flange, the predicted gradient was 7.5℃, while the NZ Bridge Manual and BS 5400 were 1.5°C and 2°C respectively.
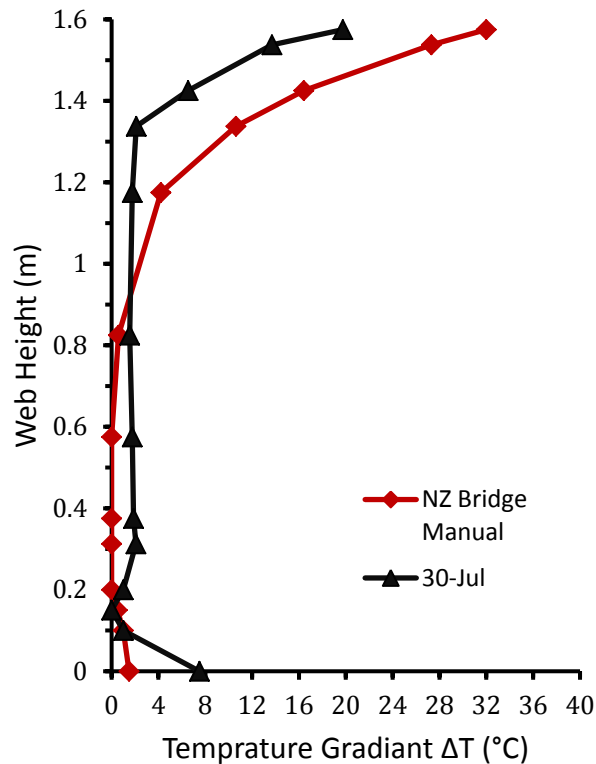
Figure 6.11 Comparison of the maximum predicted positive temperature gradient with NZ Bridge Manual Code
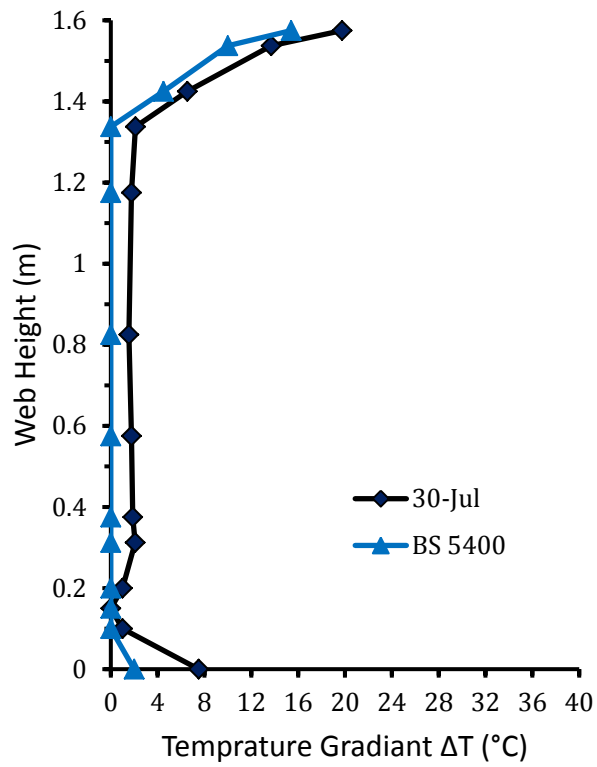
Figure 6.12 Comparison of the maximum predicted positive temperature gradient with BS 5400 Code

CHAPTER 7

CONCLUSIONS

This research investigates vertical and lateral temperature gradients and temperature distributions in PC bridge girders due to climate effects. A 3D FE heat transfer model was developed to represent the heat convection between the girder surface and the climate, heat conduction in the concrete girder, heat radiation to the ambient dings and heat irradiation from the sun. In the region of Gaziantep, Turkey, air temperature records of 30 years were used to evaluate the largest temperature gradients in June and July. To distinguish the most representative temperature gradient model, four gradient models from different bridge design codes were compared with the predicted temperature gradient.

Using daily solar radiation incident on a horizontal surface, the 3D heat transfer analysis are done. The computation of solar radiation with regarding to the time of day on all surface of the girder depended on the position of the sun, the location, geometry of the girder, the shadow on the bottom flange and the web of the girder. Based on the FE analysis of this research several conclusions were obtained.

- This study evaluates vertical and lateral temperature gradients by using seasonal variations in environmental conditions of Gaziantep, the largest vertical temperature gradients were found in the summer with the highest solar intensity on the top surface of the girder, and the largest lateral temperature gradients were found in the winter.

- During the afternoon period in summer, the top surface worms significantly due to the high intensity solar radiation, while the cores of web and bottom

flange keep lower temperatures due to the weak thermal conductivity of concrete, which causes significant temperature gradient along the depth of the girder. The maximum predicted temperature gradient was 20°C on 30 July in Gaziantep, which occurred at 1:50 pm. Thus, the thermal loads involved in this study were taken from the summer and winter environmental extreme conditions of Gaziantep.

- Based on the four seasons the highest temperature distribution along the 24 hours, which was 59.1℃ at thermocouple on the top surface, while the temperature of the bottom flange showed the highest temperatures during the cold hours.

- The maximum predicted positive and negative temperature gradients from extreme weather conditions of Gaziantep on 30 July were compared with ASSHTO LRFD Specifications. The variations and the magnitudes of the predicted temperatures were in good agreement with AASHTO LRFD Specifications for the four zones, it can be concluded that the AASHTO gradient model is suitable and well for the extreme conditions of Gaziantep with few adjustments.

- Many analytical studies on solar radiation and other climatological effects on large-scale structures carried out with ANSYS were found in literature. While, such studies with COMSOL are rare.

- To model the solar radiation in ANSYS 12.1, further programming and subroutines are required. On the other hand, simplifications may be applied to facilitate the problem, which may be accompanied with some acceptable errors.

- The built-in solar model in COMSOL is accurate and can simplify the problems. Also, using the heat transfer with surface-to-surface radiation node in the heat transfer module of COMSOL 4.3a, different thermal loads can be applied at the same time.

REFERENCES

[1]   ANSYS, ANSYS v User's 12.1 (2009). Guide, USA, Canonsburg.

[2]   COMSOL Multiphasic v 4.3a (2012). User's Guide, Stockholm.

[3]   Narouka, M. Hirai, I. and Yamaguti, T. (1955). Measurement of the Temperature of the Interior of the Reinforced Concrete Slab of the Shigita Bridge and Presumtion of Thermal Stress. Symposium of the Stress Measurements for Bridge and Structures, Japanese Society for the Promotion of Science, Proc. Tokyo, Japan.

[4]   Barber, E. S. (1957). Calculations of Maximum Pavement Temperatures from Weather Reports, *Highway Research Board Bulletin* **168**, pp. 1-8.

[5]   Leonhardt, F. Kolbe, G. and Peter, J. (1965, July). Temperaturunterschiede gefahrden spannbetonbrucke (Temperature differences endanger prestressed concrete bridge, translated into to English). Beton-undStahlbetonbau, **60**, (7), pp. 157-163. In German.

[6]   Zuk, W. (1961, September). Thermal and Shrinkage Stresses in Composite Beams. *ACI Journal*, **58**, (3), pp. 327-340.

[7]   Zuk, W. (1965). Thermal Behavior of Composite Bridges-Insulated and Uninsulated, Highway Research Record 76, National Research Council, pp. 231-253.

[8]   Priestly, M. J. N. (1972). Thermal Gradients in Bridges-Some Design Consideration, *New Zealand Engineering*, **27**, Part 7, pp. 228-233.

[9]   Maher, D. R. H. (1970). The Effects of Differential Temperature on Continuous Prestressed Concrete Bridges, *Civil Engineering Transactions*, CE **12**, pp. 29-32.

[10]   New Zealand Ministry of Works and Developments. (1970). Bridge Design Temperature Gradient. New Zealand, Wellington.

[11]   Priestly, M. J. N. (1976). Design Thermal Gradients for Concrete Bridges, *New Zealand Engineering*, **31**, Part 9, pp. 213-219.

[12]   Emerson, M. (1973). The calculation of the distribution of temperature in bridge (TRRL Report LR 561). Berkshire, UK: Transport and Road Research Laboratory.

[13]   Lagigan, A. G. (1973). The Temperature Response of Concrete Box-girder Bridge. Ph.D Thesis, Reporte No. 94, School of Engineering, University of Auckland, New Zealand.

[14] Reynolds, J. and Emanuel, J. H. (1974). Thermal Stresses and Movements in Bridge. *Journal of the Structural Engineering*, Proceedings of the ASCE, **100**, (1), pp. 63-78.

[15] Will, K. M. (1975). Analytical and experimental investigation of the thermal response of highway bridges. Doctoral dissertation, University of Texas at Austin.

[16] Will, K. M. Johnson, C. P. and Matlock, H. (1977). Analytical and experimental investigation of the thermal response of highway bridges (Research Project 23-2). Interim report to Texas state department of highways and public transportation, University of Texas at Austin.

[17] Radolli, M. and Green, R. (1975). Thermal Stresses in Concrete Bridge Superstryctures under Summer Conditions. Transportation Research Record 547, Transportation Research Board.

[18] Emanuel, J. H. and Hulsey, J. L. (1978). Temperature Distributions in Composite Bridges, *Journal of the Structural Division*. ASCE, **104**, pp. 65-78.

[19] Dilger, W. H. Ghali, A. and Cheung, M. S. (1981, November). Field Measurements of Muskwa River Bridge. *Journal of Structural Division*, **107**, (11), pp. 2147-2161.

[20] Dilger, W. H. Ghali, A. Cheung, M. S. and Maes, M. A. (1983). Temperature stresses in composite box girder bridges. *Journal of Structural Engineering*, **109,** (6), pp. 1460-1478.

[21] Kenney, J. B. and Soliman, M. H. (1987). Temperature distribution in composite bridges. *Journal of Structural Engineering*, **113**, (3), pp. 475-482.

[22] Clark, H. (1989). Evaluation of Thermal Stress in a Concrete Bridge, Ph.D.University of Washington, 261.

[23] Emerson, M. (1968). Bridge temperature movements in the British Isles, (TRRL Report No LR 228), England, Berkshire, UK: Transport and Road Research Laboratory.

[24] Emerson, M. (1982). Thermal movements of concrete bridges, field measurements and method of prediction, (TRRL Supplementary Report No SR 747), (TRRL Report No LR 765), England, Transport and Road Research Laboratory.

[25] Emerson, M. (1977). Temperature differences in bridge: basis of design requirements, (TRRL Report No LR 765), England, Transport and Road Research Laboratory.

[26] Emerson, M. (1980). Temperature in bridges during cold winter of 1978/1979, (TRRL Report No LR 765), England, Transport and Road Research Laboratory.

[27] Moorty, S. and Roeder, C. W. (1992, April). Temperature-dependent bridge movements. *Journal of Structural Engineering*, 118 (4), pp. 1090-1105.

[28] Imbsen, R. A. (1985). Vandershaf. D. E. Schamber, R. A. and Nutt, R. V. Thermal Effects in Concrete Bridge Superstructure. Nationnal Cooperative Highway Research Program, Report 276, National Research Council,

Washington.

[29] Elbadry, M. M. and Ghali, A. (1983). Temperature Variations in Concrete Bridges, *Journal of Structural Engineering*, ASCE, **109**, pp. 2355-2374.

[30] Elbadry, M. and Ghali, A. (1986). Thermal Stresses and Cracking of Concrete Bridges, *ACI Journal*, **83**, pp. 1001-1009.

[31] Elbadry, M. M. and Ghali, A. (1989). Serviceability Design of Continuous Prestressed Concrete Structures. *Journal of the Prestressed Concrete Institute*, **34**, (1), pp. 54-91.

[32] Mirambell, E. and Aguado, A. (1990, September). Temperature and stress distributions in concrete box girder bridges. *Journal of Structural Engineering*, **116**, (9), pp. 2388- 2409.

[33] Dilger, W. H. Ghali, A. and Cheung, M. S. (1981, November). Field Measurements of Muskwa River Bridge. *Journal of Structural Division*, **107**, (11), pp. 2147-2161.

[34] Churchward, A. and Sokai, Y. J. (1981). Prediction of temperatures in concrete bridges. *Journal of Structural Engineering*, **107**, (11), pp. 2163-2176.

[35] Roberts-Wollman, C.L. Breen, J.E. and Cawrse, J. (2002, May). Measurements of thermal gradients and their effects on segmental concrete bridge. *Journal of Bridge Engineering*, **7**, (3), pp. 166-174.

[36] AASHTO. (1999). Guide Specifications for Design and Construction of Segmental Concrete Bridges, 2nd ed. American Association of State Highway and Transportation Officials, USA, Washington, DC.

[37] AASHTO. (1994). AASHTO LRFD Bridge Design Specifications. 1st Ed. American Association of State Highway and Transportation Officials (AASHTO), USA, Washington, D.C.

[38] AASHTO (2000). AASHTO LRFD Bridge Design Specifications. American Association of State Highway and Transportation Officials. USA, Washington, D.C.

[39] Saetta, A. Scotta, R. and Vitaliani, R. (1995). Stress analysis of concrete structures subjected to variable thermal loads. *Journal of Structural Engineering*, **121**, (3), pp. 446-457.

[40] Suchinda, C. and Will, K. M. (1999, June). A temperature response measurement in fiber reinforced polymeric bridge decks. Proceedings of Sixth Annual International Conference on Composite Engineering. Orlando, FL.

[41] Suchinda, C. (2000). Experimental and analytical investigation of the thermal behavior of a fiber reinforced polymeric bridge deck. Doctoral dissertation, Georgia Institute of Technology.

[42] Gilland, J. A. and Dilger, W. H. (1997). Monitoring concrete temperature during construction of the confederation bridge. *Canadian Journal of Civil Engineering*, **24**, pp. 941-950.

[43] Roeder, C. W. (2003). Proposed Design Method for Thermal Bridge Movements. *ASCE - Journal of Bridge Engineering*, pp. 12-19.

[44] AASHTO. (2010). AASHTO LRFD Bridge Design Specifications, 4th Ed. American Association of State Highway and Transportation Officials (AASHTO). USA, Washington, D.C.

[45] AASHTO. (1996). AASHTO Standard Specification for Highway Bridges, 15th Ed. American Association of State Highway and Transportation Officials (AASHTO). USA, Washington, D.C.

[46] Li, D. Maes, M. A. and Dilger, W. H. (2004). Thermal Design Criteria for Deep Prestressed Concrete Girders Based on Data from Confederation Bridge, *Canadian Journal of Civil Engineering*, **31**, pp. 813-825.

[47] CSA. Canadian Standard Association. (2000). Design of Highway Bridges. Standard (CAN/CSA-S6-00), Canada, Ontario. Design Brief.

[48] Jong-Hang Lee, (2010). Experimental and Analytical Investigations of The Thermal Behavior of Prestresses Concrete Bridge Including Implementation. Ph.D. Thesis, USA, GA, Atlanta, Georgia.

[49] ABAQUS. (2008). Abaqus version 6.8. Providence, RI: Dassault Systems Simulia Corp.

[50] Wang, J. and Fang, Z. (2009). Temperature Variation of Concrete Box Girder Bridge, *Frontiers of Structural and Civil Engineering,* **3**, (4), pp. 407-413.

[51] Zhang, L. Wu, L. and Yang, L. (2012). Analysis of Temperature Field of Concrete Box Girder and Secondary Development of Program, *Journal of Convergence Information Technology*, **7**.

[52] Carboni, B. and Lacarbonara, W. (2012). A Three-Dimensional Continuum Approach to The Thermoelastodynamics of Large Scale Structures, *Engineering Structures*, **40**, pp. 155-167.

[53] New Zealand Ministry of Works and Developments, (1973). Highway Bridge Design Brief.

[54] New Zealand Ministry of Works and Developments, (1977). Highway Bridge Design Brief.

[55] Quan C. (2008). Effects of Thermal loads on Texas Steel Bridges. Ph.D thesis, USA, Texas, The University of Texas at Austin.

[56] AASHTO. (1989). AASHTO Guide Specifications Thermal effects in concrete bridge superstructures. American Association of State Highway and Transportation Officials. USA, Washington, DC.

[57] AASHTO. (2007). AASHTO LRFD Bridge Design Specifications. 4th Ed. American Association of State Highway and Transportation Officials. USA, Washington, D.C.